Inaugural dissertation

for

obtaining the doctoral degree

of the

Combined Faculty of Mathematics, Engineering and Natural Sciences

of the

Ruprecht - Karls - University

Heidelberg

Presented by

M.Sc. Ruben Bulkescher

born in: Mühlbach, Romania

Oral examination: 17.10.2022

Effects of dicarbonyl stress in the absence of

HSPA1A/HSPA1B in endothelial cells

and STZ-induced diabetic mice on the

development of diabetic nephropathy

Referees:

Prof. Dr. Marc Freichel

Prof. Dr. Matthias Mayer

CONTENTS

ABSTRACT

The number of individuals diagnosed with diabetes continues to increase year over year, with roughly half a billion people affected worldwide. Diabetes-related comorbidities are an extra burden on patients and account for many deaths through cardiovascular events (heart attack and stroke) or microvascular organ damage (nephropathy, neuropathy, and retinopathy). In Germany, diabetic nephropathy is the leading cause for kidney failure which leaves patients no other choice than renal dialysis or waiting for an organ transplant. This puts a tremendous financial strain on the public health sector. Therefore, therapies are needed to prevent or slow down the progression of diabetes-related alterations of the vasculature or organs.

Proteotoxic properties of glycated proteins (so called advanced glycation end products or AGEs), have been marked as one pathway leading to diabetic nephropathy, especially adducts from the reactive dicarbonyl methylglyoxal (MG). In this regard, the heat-shock proteins *Hspa1a* and *Hspa1b* were chosen as a target, as they have the greatest importance in addressing protein misfolding and aggregation. In this work, the loss of *Hspa1a/Hspa1b* on methylglyoxal-induced endothelial dysfunction was studied *in vitro,* whilst the effect on diabetic nephropathy was studied *in vivo* using an experimental model of type 1 diabetes.

A loss of *Hspa1a/Hspa1b* did lead to an increase of MG-derived advanced glycation end products in vitro. However, clearance of MG-modified proteins was unaffected. In addition, oxidative stress and expression of inflammation markers were increased. Furthermore, MG triggered changes of the mitochondrial network after acute and chronic stress in *Hspa1a/Hspa1b* knockout cells, whereas mitochondrial respiration remained unchanged. *In vivo*, the kidneys from *Hspa1a/Hspa1b* knockout mice showed no differences in renal parameters, either in control or STZ-diabetic mice. Mesangial matrix was found to be increased in the STZ-diabetic mice, which was enhanced in the *Hspa1a/Hspa1b* knockout mice. Interestingly, the lack of *Hspa1a/Hspa1b* seemed to attenuate albuminuria.

In conclusion, the *in vitro* results indicate that a deficiency of *Hspa1a/Hspa1b* shortly increases a MG-H1 accumulation under acute MG-stress and induces changes in the mitochondrial network. The *in vivo* data suggest that a loss of *Hspa1a/Hspa1b* might be protective in respect of albuminuria and might be an interesting therapeutic target.

VI

ZUSAMMENFASSUNG

Die Zahl der Patienten mit Diabetes nimmt von Jahr zu Jahr zu. Mittlerweile gibt es weltweit über eine halbe Milliarde Menschen mit dieser Diagnose. Dazu kommen häufig noch durch den Diabetes-bedingte Komorbiditäten wie kardiovaskuläre Erkrankungen (Herzinfarkt und Schlaganfall), und mikrovaskuläre Organschädigungen (Nephropathie, Neuropathie und Retinopathie), welche eine zusätzliche Belastung für die Patienten darstellen. Die diabetische Nephropathie ist die Hauptursache für ein terminales Nierenversagen, wodurch Patienten viele Jahre auf Dialyse angewiesen sind, während sie auf ein Spenderorgan warten. Diese Behandlungen stellen eine große finanzielle Last für das Gesundheitssystem dar. Daher ist es notwendig Therapien zu erforschen, welche das Auftreten von diabetischen Spätfolgen verhindern oder deren Fortschreiten verlangsamen können. Die proteintoxischen Eigenschaften einer Proteinglykierung werden als eine potenzielle Ursache für das Auftreten der diabetischen Nephropathie gesehen. Besonders hervorzuheben ist dabei das reaktive Ketoaldehyd Methylglyoxal (MG). In diesem Kontext wurden die Hitzeschockproteine *Hspa1a* und *Hspa1b* ausgewählt, da sie eine Schlüsselfunktion bei der Prozessierung von fehlgefalteten und aggregierten Proteinen haben. Ziel dieser Arbeit war es herauszufinden, wie sich der Verlust von *Hspa1a/Hspa1b* auf die MG-induzierte endotheliale Dysfunktion im Zellmodell auswirkt und ob die diabetische Nephropathie in einem Diabetes Mausmodell verschlimmert wird.

Der Verlust von *Hspa1a/Hspa1b* führte tatsächlich zu einer vermehrten Akkumulation der Proteinglykierung durch MG, in Form von MG-H1. Allerdings wurde dadurch der Abbau von MG-H1 nicht beeinträchtigt. Zusätzlich traten in den Knockout Zellen vermehrt oxidativer Stress und die Expression von Entzündungsmediatoren auf. Des Weiteren versursachte akuter und chronischer MG-Stress eine Umstrukturierung des mitochondrialen Netzwerkes in *Hspa1a/Hspa1b* Knockout Zellen, die jedoch nicht mit einer Veränderung der mitochondrialen Atmungskette einherging.

Im Mausmodell wurden in den Nieren keine Veränderungen der Morphologie beobachtet, mit Ausnahme einer vergrößerten mesangialen Matrix in diabetischen Mäusen. Dies war in den *Hspa1a/Hspa1b* Knockout Mäusen stärker ausgeprägt. Besonders hervorzuheben ist die Erkenntnis, dass ein Verlust von *Hspa1a/Hspa1b*

zu einer schwächeren Ausprägung der Albuminurie in den diabetischen Mäusen geführt hat.

Abschließend kann man sagen, dass der Verlust von *Hspa1a/Hspa1b* in Endothelzellen zu einer Erhöhung von Diabetes-assoziiertem Stress, in Form von kurzfristig erhöhten MG-H1 Konzentrationen, und Änderungen im mitochondrialen Netzwerk führt. Die in vivo Daten zeigten, dass sich der Verlust von *Hspa1a/Hspa1b* positiv auf die Entwicklung einer Albuminurie auswirkt. Dies könnte ein interessanter Ansatzpunkt für eine medikamentöse Therapie sein.

ABBREVIATIONS

3DG-H1	3-Deoxyglucosone-hydroimidazolone 1
AFOG	Acid fuchsin orange G
AGE	Advanced glycation end product
ANOVA	Analysis of variance
ARE	Antioxidant response element
ATP	Adenosine triphosphate
BIH	Bioenergetic health index
BMI	Body mass index
BNIP3	BCL2/adenovirus E1B 19 kda protein-interacting protein 3
BSA	Bovine serum albumin
C57BL/6	C57 black 6 mouse strain
Cas9	CRISPR associated endonuclease 9
CEL	Nε-(carboxyethyl)-lysine
CMCP	Center for Model System and Comparative Pathology
CML	Nε-(carboxymethyl)-lysine
COX1	Complex 1
CRISPR	Clustered regularly interspaced short palindromic repeats
Ctrl	Control
DNA	Deoxyribonucleic acid
DNAJB1	Dnaj homolog subfamily B member 1
DRP1	Dynamin-related protein 1
e.g.	Example given
ECM	Extracellular matrix
ED50	Median effective dose
FCCP	Carbonyl cyanide-4-(trifluoromethoxy) phenylhydrazone
FIS1	Mitochondrial fission protein 1
FMA	Fractional mesangial area
G-H1	Glyoxal-derived hydroimidazolone 1
GADA	Glutamic acid decarboxylase antibodies
GBM	Glomerular basement membrane

GDF15	Growth differentiation factor 15
GLO1	Glyoxalase 1
GLP-1-RA	Glucagon-like peptide 1 receptor agonists
GRP78	Glucose-related protein 78
GTP	Guanosine triphosphate
HbA$_{1C}$	Glycated hemoglobin
HO1	Heme oxygenase 1
HOMA2-B	Homeostasis model assessment 2 estimate of beta cell function
HOMA2-IR	Homeostasis model assessment 2 estimate of insulin resistance
HSF1	Heat-shock factor 1
HSP	Heat-shock protein
ICAM1	Intercellular adhesion molecule 1
IHC	Immunohistochemistry
IL-6	Interleukin 6
IMM	Inner mitochondrial membrane
KO	Knockout
LC-MS/MS	Liquid chromatography - tandem mass spectrometry
LC3	Microtubule-associated protein 1 light chain 3 alpha
MARD	Mild age-related diabetes
MCEC	Mouse cardiac endothelial cells
MFN1	Mitofusin 1
MFN2	Mitofusin 2
MG	Methylglyoxal
MG-H1	Methylglyoxal-derived hydroimidazolone 1
MOD	Mild obesity-related diabetes
mtDNA	Mitochondrial deoxyribonucleic acid
N	Number
NBD	Nucleotide binding domain
NF-KB	Nuclear factor kappa-light-chain-enhancer of activated B cells
NQO1	NAD(P)H dehydrogenase [quinone] 1
NRF1	Nuclear respiratory factor 1
NRF2	Nuclear respiratory factor 2
ns	Not statistically significant
OCR	Oxygen consumption rate

X

oGTT	Oral glucose tolerance test
OMM	Outer mitochondrial membrane
OPA1	Optic atrophy protein 1
p	Probability value
PARKIN	Parkinson juvenile disease protein
PCR	Polymerase chain reaction
PGC1A	Peroxisome proliferator-activated receptor gamma coactivator 1
PGC1B	Peroxisome proliferator-activated receptor gamma coactivator 2
PINK1	PTEN-induced putative kinase protein 1
PTEN	Phosphatase and tensin homolog
qRT-PCR	Quantitative real-time polymerase chain reaction
RAGE	Receptor for advanced glycation end products
RNA	Ribonucleic acid
ROS	Reactive oxygen species
SAID	Severe autoimmune diabetes
SBD	Substrate binding domain
SD	Standard deviation
SGLT2	Sodium-glucose linked transporter 2
SIDD	Severe insulin-deficient diabetes
SIRD	Severe insulin-resistant diabetes
STZ	Streptozotocin
TFAM	Mitochondrial transcription factor 1
TFB2M	Transcription factor B2 mitochondrial
TIMM	Translocase of inner mitochondrial membrane
TLR4	Toll-like receptor 4
TNF-alpha	Tumor necrosis factor alpha
TOMM	Translocase of outer mitochondrial membrane
UACR	Urinary albumin-to-creatinine ratio
VCAM1	Vascular adhesion molecule 1
WT	Wild-type

UNITS

°C	Degree Celsius
bp	Base pairs
cm	Centimeter
Da	Dalton
dL	Deciliter
eV	Electronvolt
g	Gram
h	Hour
kb	Kilobase
kDa	Kilodalton
kV	Kilovolt
mg	Milligram
min	Minute
mL	Milliliter
mm	Millimeter
mmol	Millimole
ms	Milliseconds
ng	Nanogram
nm	Nanometer
pmol	Picomole
rpm	Revolutions per minute
U/mL	Units/milliliter
V	Volt
µm	Micrometer
µM	Micromolar

LIST OF FIGURES

LIST OF TABLES

1 INTRODUCTION

1.1 Diabetes mellitus

Diabetes mellitus is a chronic metabolic disease. Patients present with high blood glucose levels, referred to as hyperglycemia. To date, around 537 million adults (20-79 years) are diagnosed with diabetes, which is roughly 7% of the world population (Figure 1).[1] In Germany, over 6.2 million adult patients are diagnosed with diabetes, accounting for 7.5% of the German population. Globally, 6.7 million deaths in the age group of 20-79 were attributed to diabetes or diabetes-related complications in 2021.[1]
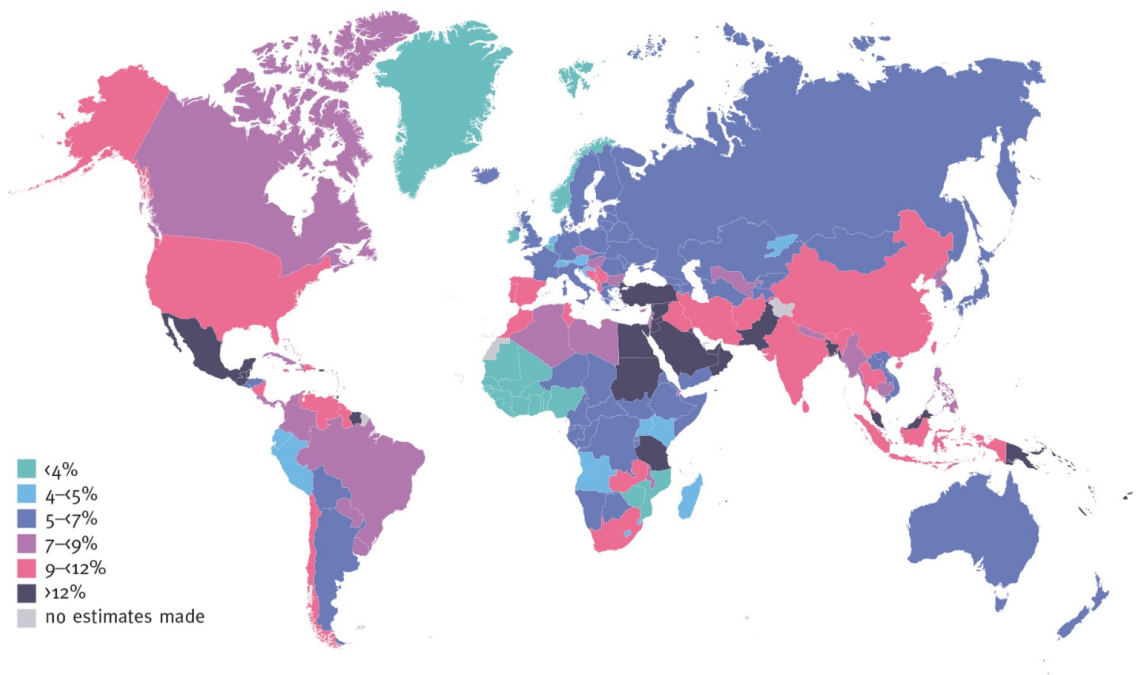
Figure 1 Diabetes around the world.
The map shows the percental incidence of diabetics in all countries around the world. Figure adapted from ref. [1].

1.1.1 Diagnosis

Diabetes mellitus is diagnosed through the abundance of elevated levels of blood glucose. During the fasting state, values of 100 mg/dL and below are measured in healthy individuals. Values equal or above 126 mg/dL are sufficient for the diagnose of diabetes. Fasted blood glucose levels between 100-125 mg/dL indicate an impaired fasting glucose, which can be seen as a prediabetic state. Next to the fasted blood glucose level, the oral glucose tolerance test (oGTT) can be used for the diagnosis of an impaired glucose tolerance.[2] During this test, 75 g of glucose in a glass of water are ingested and the plasma glucose is measured. In a healthy person, two hours after ingestion of 75 g of glucose, the level stays below 140 mg/dL, whereas in diabetes the level exceeds 200 mg/dL (Figure 2). Intermediate values between 140-200 mg/dL are present in patients with impaired glucose tolerance, which again can be present in prediabetes. Another measure for the diagnosis of diabetes is the ratio of glycated hemoglobin (HbA_{1C}). In healthy individuals it is below 5.7%, in diabetics it is constantly above 6.5%. Values in between can hint to a prediabetes.[3]
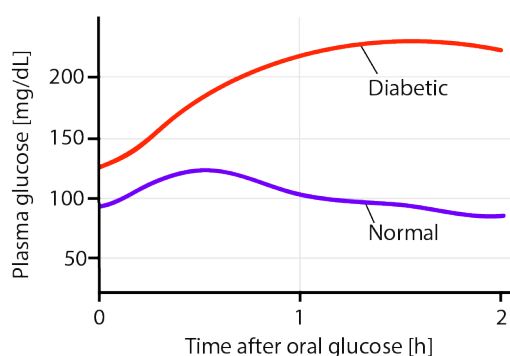
Figure 2 Oral glucose tolerance test.
Plasma glucose concentrations after an oral glucose tolerance test in a healthy and a diabetic patient. For an oral glucose tolerance test, 75 g of glucose are ingested, and the plasma glucose is measured over a time span of 120 minutes.

1.1.2 Traditional classification system of diabetes subtypes

Patients with diabetes can be categorized in four classes. In type 1 diabetes, which is also termed juvenile diabetes, the insulin-producing beta cells in the pancreas are lost by autoimmune reactions, which lead to an insulin deficiency.[4] However it has to be noticed that autoimmune diabetes can have its onset as well in adult age (so-called "late onset diabetes in adults", or LADA). If it occurs in obese adult patients, this often

leads to wrong categorization as type 2 diabetes. Therefore, measurement of autoimmune antibodies, like glutamic acid decarboxylase and islet cell autoantibodies, is essential for making the right diagnose.[5,6] Around 5-10% of diabetic patients fall into the group of type 1 diabetes (high interregional difference, e.g. Finland).[2] Type 2 diabetes, or adult-onset diabetes, is a multifactorial disease that typically develops in patients that are obese, or have a higher percentage of abdominal fat together with a positive family history of type 2 diabetes.[2] An unhealthy lifestyle with a high caloric intake in combination with low physical activity leads to chronic elevated levels of blood glucose. As this lifestyle is nowadays also present in children and adolescents, these age groups can also develop type 2 diabetes. Over time, elevated levels of blood glucose, cause an insulin resistance, which results in a diminished insulin-regulated uptake of glucose by GLUT4 (glucose transporter type 4) in muscle, liver, and fat tissue. The third type of diabetes is called gestational diabetes.[7] It occurs during pregnancy and is characterized by glucose intolerance.[2] There are several risk factors, that facilitate the development of gestational diabetes, including obesity or a family history of type 2 diabetes.[8] The fourth group includes types of diabetes that arise from different causes. Diabetes can be induced from drugs, genetic defects in the beta cells of the pancreas (so-called "Maturity onset of diabetes of the young", or MODY), hormonal imbalances and infections as well as after pancreatectomy.[7] Gestational diabetes and the specific types of diabetes from type 4 are much less common than type 1 and type 2 diabetes.[2]

1.1.3 New classification system of diabetes subtypes

With the classification of patients in the four subgroups alone, no prediction can be made, whether a patient is more prone to develop certain diabetic complications. For this, patients must be closely monitored for elevated blood lipids, albumin excretion, and routine visits with an endocrinologist, an ophthalmologist, and a neurologist. Therefore, in 2018, the classification has been revised into 5 new subgroups.[9] This new classification includes more patient characteristics and evaluates the respective risks of developing diabetic complications. For the differentiation of patients into these new subgroups the measurements of six variables are combined (Figure 3). Those variables are age at diagnosis, glycated hemoglobin (HbA$_{1c}$), body mass index (BMI)[10], glutamic acid decarboxylase antibodies (GADA)[2] and estimates of the beta cell function (HOMA2-B; homeostasis model assessment 2)[11] and insulin resistance

(HOMA2-IR).[12] Furthermore, the existence and severity of diabetic complications and prescription of medication were included. The 5 clusters are:

1) SAID: severe autoimmune diabetes. The first cluster includes patients with an early-onset disease, who have poor metabolic control, a low BMI, the presence of GADA and an insulin deficiency.

2) SIDD: severe insulin-deficient diabetes. Patients who are assigned to cluster 2 have similar characteristics to patients in cluster 1 but are GADA negative.

3) SIRD: severe insulin-resistant diabetes. Cluster 3 includes patients who have a high body mass index and a high insulin resistance (HOMA2-IR).

4) MOD: mild obesity-related diabetes. Patients in cluster 4 are considered obese with a high BMI, however they are not showing an insulin resistance.

5) MARD: mild age-related diabetes. The last cluster includes patients with a higher age and a lower BMI, but otherwise with the same characteristics as patients in cluster 4.
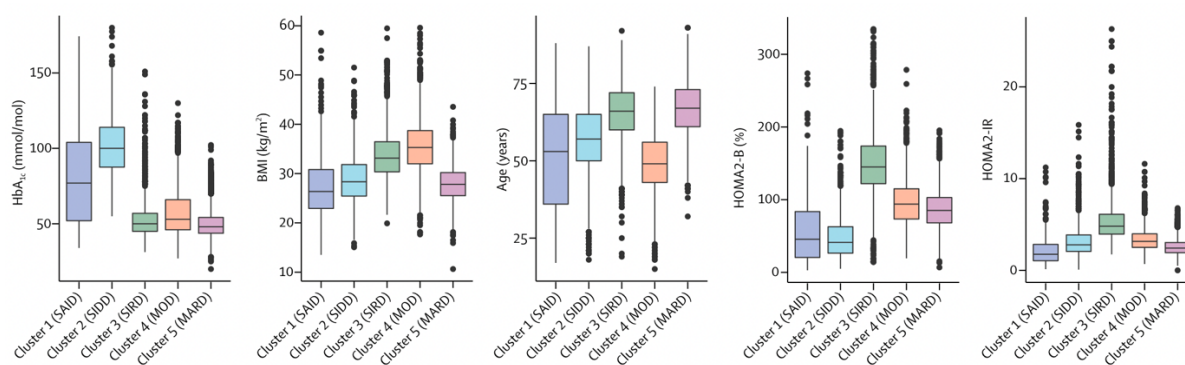
Figure 3 Novel subgroups of adult-onset diabetes.
Diabetic patients are clustered in 5 subgroups for each of the respective characteristic, which are HbA_{1C}, body mass index, age of onset of diabetes, HOMA2-B (estimate for the beta cell function) and HOMA2-IR (estimate for insulin resistance). SAID: severe autoimmune diabetes; SIDD: severe insulin-deficient diabetes; SIRD: severe insulin-resistant diabetes; MOD: mild obesity-related diabetes; MARD: mild age-related diabetes. Figure adapted from ref. [9].

Patients that were assigned to cluster 3 showed a higher risk for diabetic and chronic kidney disease. Furthermore, they were more likely to suffer from end-stage renal disease than patients assigned to cluster 5. Patients in cluster 2 were more commonly diagnosed with diabetic retinopathy, than patients in the other clusters.[9]

A study from the DZD (Deutsches Zentrum für Diabetesforschung, German center of diabetes research) has also investigated how this new clustering of patients can be

beneficial in terms of diagnosis and forecast of diabetic-related complications.[13] A third study focused on predicting diabetic complications in patients with prediabetes.[14] With these new subgroups, the risk evaluation of patients developing specific diabetic complications can be more easily predicted and treatment options can be tailored to the individual patient.

1.2 Diabetic complications

Diabetic patients often develop comorbidities throughout their life. These diabetes-associated diseases can be divided in macrovascular and microvascular complications. Among the macrovascular complications are coronary artery disease, cardiomyopathy and stroke.[15] The most occurring microvascular complications include diabetic retinopathy[16], diabetic neuropathy[17], and diabetic nephropathy[18]. More recently acknowledged diabetic complications that arise from the development of fibrosis are for example non-alcoholic fatty acid liver disease (NAFLD) and non-alcoholic steatohepatitis (NASH), as well as lung fibrosis or diabetic pneumopathy.[19,20]

The pathogenesis of these complications is not fully understood. Only one aspect that is constant are elevated levels of blood glucose besides an increase of reactive metabolites. Patients with hyperglycemia also tend to have higher levels of triglycerides[21], which promote atherosclerosis (macroangiopathy) in large blood vessels (Figure 4A). In atherosclerosis, fat and blood clots build up in the arteries and stick to the vessel walls. Over time, the arteries narrow and the blood flow is reduced, up to the point where it is completely clogged and increases the risk of an ischemic heart attack or stroke.[22]
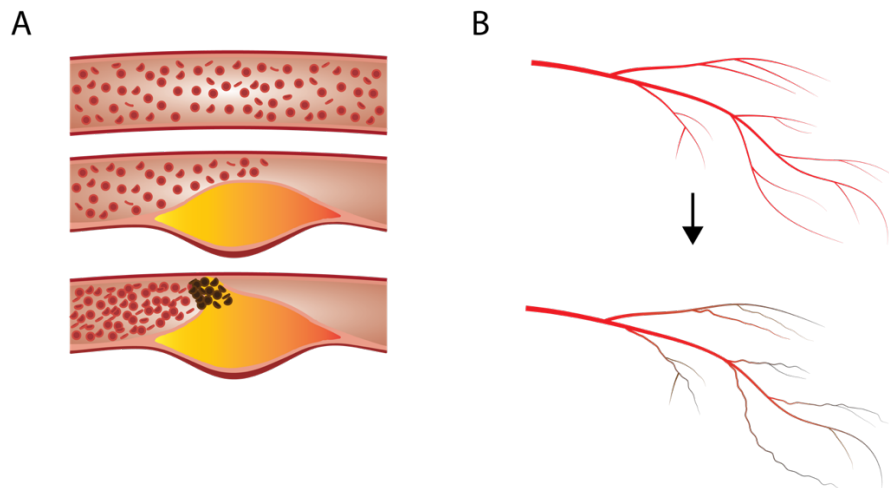
Figure 4 Illustration of the development of macro- and microangiopathy.
(A) In macroangiopathy or atherosclerosis, so-called plaques, which are made of fat, blood cells, calcium and cholesterol clog and narrow the arteries which reduces blood flow and eventually leads to coronary artery disease or stroke. (B) In microangiopathy or microvascular disease the constant high levels of blood glucose lead to a weakening of the vessel walls, which can result in leaks that affect the blood flow to the organs.

Microangiopathy affects the small blood vessels (Figure 4B). It develops, when the endothelial cells lining the blood vessels are constantly exposed to high levels of blood glucose, resulting in increased protein glycation. This in turn leads to a vascular permeability and changes of the blood flow to the organs, that can damage the organs after a constant undersupply of oxygen and nutrients, especially the kidney and the retina.[23,24]

There are several hypotheses, how diabetic complications form on the molecular level, e.g. through an increased polyol pathway flux, the activation of protein kinase C, or through an increased flux through the hexosamine pathway.[25]

A fourth hypothesis, which is further investigated in this study, focusses on the increased formation of advanced glycation end products as an important mechanism for the development of diabetic complications.[25]

Diabetic nephropathy is the leading cause for end-stage renal disease worldwide and affects diabetic patients severely in their daily life.[26] Moreover, the kidney health deterioration is progressing with diabetes duration. Therefore, I decided to focus on diabetic nephropathy induced kidney changes in this thesis.

1.2.1 Physiology and functions of the kidneys

The kidney is an important organ that is essential for survival. Foremost it filters the blood that passes through it. Thereby it reabsorbs water, molecules like glucose and proteins, and excretes toxins, salts, hormones, and metabolites in the form of urine. Other functions include the blood-pressure regulation, acid-base homeostasis, and the regulation of osmolality. Anatomically, the kidneys are engulfed by the renal capsule, and consist of the outer cortex, and the inner renal medulla. The functional unit of the kidney is the nephron. A human kidney has around 1.2 million nephrons. It consists of the renal corpuscle and the renal tubule. The renal corpuscle can be further divided into the glomerulus and the Bowman's capsule.[27] During the glomerular filtration, blood is entering the glomerulus *via* the afferent arteriole and leaving it *via* the efferent arteriole (Figure 5). In between it is filtered by passing through the glomerular capillary endothelial cells, the glomerular membrane, and podocytes until it reaches the Bowman's space. Under healthy conditions, the glomerular filtrate is free of proteins, as their size is too big to pass through the pores in the glomerular capillary walls. The glomerular filtration rate is about 180 liters per day and around 1-2 liters of urine are produced. In the second part of the blood filtration, electrolytes, glucose, amino acids, creatinine and water, that are in the glomerular filtrate, are reabsorbed in the proximal tubules.[28] In the case that proteins like albumin or low-molecular weight proteins are glomerulary filtered, they will be retrieved *via* receptor-mediated endocytosis.[28] The proximal tubule reabsorbs nearly 100% of the passing glucose (up to 180 g per day). This is done by the sodium-glucose linked transporters (SGLT) 1 and 2. The proximal tubule also secretes molecules, which include hydrogen, uric acid, phosphate and waste products, or toxins.[29]
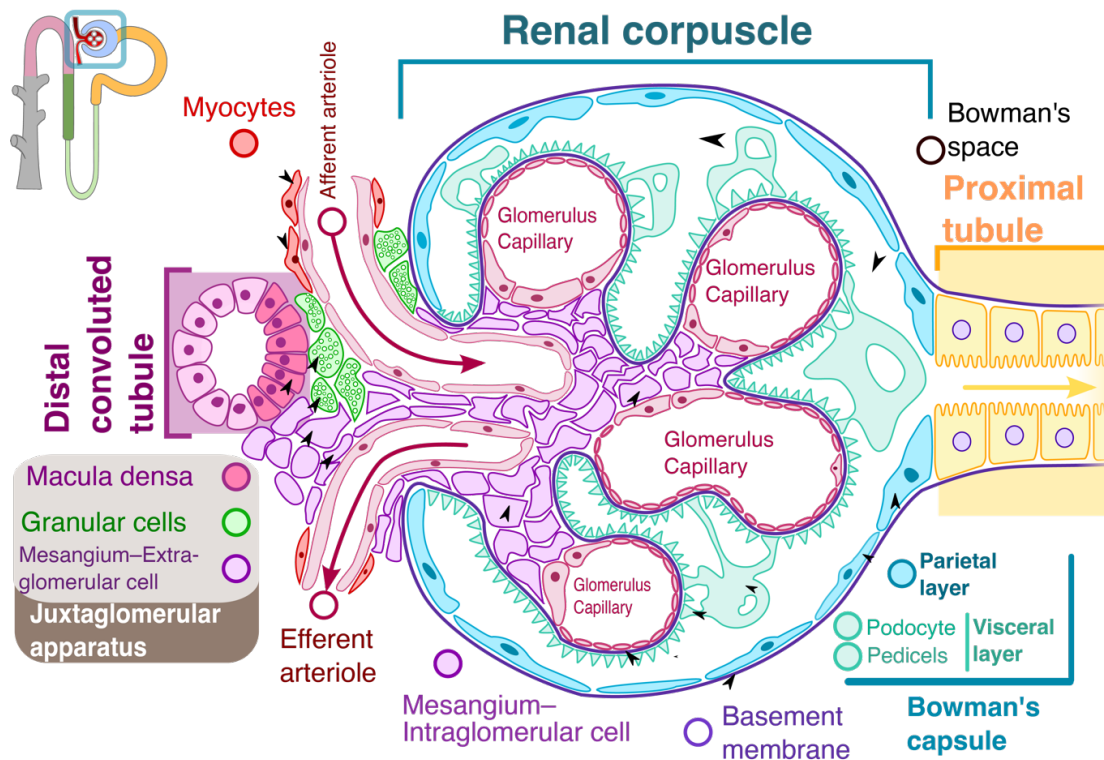
Figure 5 Schematic illustration of a renal corpuscle.
Blood enters the glomerulus through the afferent arteriole. It is then filtered by passing through the glomerular capillary endothelial cells, the glomerular basement membrane and podocytes and collected in the Bowman's space. Then the filtrate reaches the proximal tubule, where electrolytes, glucose, amino acids, creatinine, and water are reabsorbed. Figure adapted from ref. [30].

1.2.2   Diabetic nephropathy

All parts of the kidney tissue can be affected in diabetic kidney disease: the glomerulus, the vasculature, the interstitium and the renal tubules. Pathological changes of the glomerulus include glomerular lesions, a mesangial expansion, podocyte loss and a thickening of the glomerular basement membrane.[31] These pathological changes lead to a hardening and scarring of the glomerular tissue, also known as glomerulosclerosis, resulting in glomerular hyperfiltration and protein leakage.[32,33] Albumin is the most abundant protein in the blood plasma and the leakage of this protein, also called albuminuria, is one consequence of glomerulosclerosis. The albumin excretion rate (AER) is measured as mg albumin excreted in urine in 24 hours.[18] The albumin-to-creatinine ratio can be used, when a urine collection for 24 hours is not possible, since the creatinine excretion is very stable and can be used to normalize for the excretion of other molecules in the urine. The severity of albuminuria depends on the amount of excreted albumin found in the

urine and is categorized in normal (<30 mg albumin per 24 hours), mild (30-300 mg albumin per 24 hours) or severe (>300 mg albumin per 24 hours) albuminuria (see Table 1).[18]

Table 1 Categories of albuminuria

Measure	Normal albuminuria	Mild albuminuria	Severe albuminuria
Albumin excretion rate (mg per 24 hours)	<30	30-300	>300
Albumin-to-creatinine ratio (mg/g)	<30	30-300	>300
Albumin-to-creatinine ratio (mg/mmol)	<3	3-30	>30

Further symptoms that manifest in diabetic nephropathy include an increase in blood pressure[34], reduction of the estimated glomerular filtration rate[35], interstitial fibrosis[36,37], tubular atrophy[38], as well as atherosclerosis[39,40].

1.2.2.1 Therapy options

Insulin is the most known diabetes medication. It is not only administered to type 1 diabetics but also type 2 diabetics, usually in combination with other anti-diabetic medication. These include for example metformin, SGLT2 (Sodium-glucose linked transporter 2) inhibitors and GLP-1 receptor agonists (Glucagon-like peptide 1), that provide additional benefits that reduce symptoms occurring in diabetes-related complications. The exact mode of action of metformin is still unknown, however, it is assumed to act on three levels: inhibition of gluconeogenesis[41], inhibition of glucose resorption in the gut, and lowering insulin resistance.[42] SGLT1 and 2 reabsorb glucose molecules in the proximal tubules into the blood stream.[43] A pharmacological inhibition of this process is used to reduce the plasma glucose and thereby lower the HbA_{1C} levels in diabetic patients. Furthermore, SGLT2 inhibitors cause a reduction of body weight[44], lower the systolic and diastolic blood pressure[45], and show a reduction in albuminuria and podocyte autophagy[46], which are all nephroprotective.[47,48]

GLP-1-RA (receptor agonists) act like GLP-1 and bind to G-protein coupled receptors on the beta cells, and thereby cause an increase in insulin excretion.[49] Aside from the lowering of plasma blood glucose, they provide nephroprotective effects.[50,51] GLP-1-RA reduce the progression of albuminuria[52] and fibrosis, through a

suppression of the tubular expression of the pro-inflammatory genes TNF-alpha (tumor necrosis factor alpha) and MCP-1 (monocyte chemoattractant protein 1).[53,54]

1.3 Advanced glycation end products

In vivo, advanced glycation end products (AGEs) are mainly formed by the glycation of proteins, lipids and DNA, a process that happens non-enzymatically.[55–57] AGEs are formed from glucose, ascorbic acid, polyunsaturated fatty acids and the reactive metabolites methylglyoxal (MG), glyoxal and 3-deoxyglucosone (Figure 6).[58–61] The resulting advanced glycation end products are called glucosepane, pentosidine, N^ε-(carboxymethyl)-lysine (CML), methylglyoxal-derived hydroimidazolone 1 (MG-H1) and N^ε-(carboxyethyl)-lysine (CEL), glyoxal-derived hydroimidazolone 1 (G-H1) and 3-deoxyglucosone-hydroimidazolone 1 (3DG-H1).[62–64]
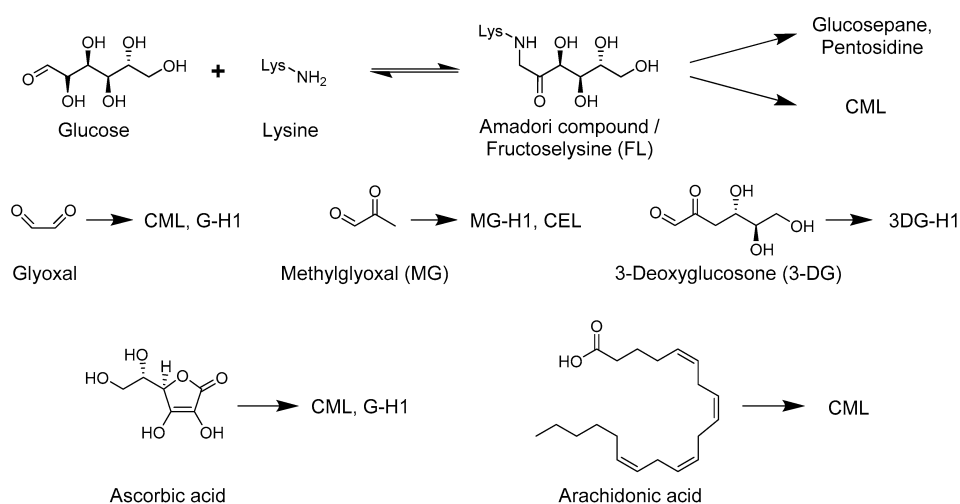
Figure 6 Precursor molecules for the formation of advanced glycation end products.
Glucose, glyoxal, methylglyoxal, 3-deoxyyglucosone, ascorbic acid and arachidonic acid undergo a Maillard reaction to form a post-translational protein modification on lysine and arginine side chains. The resulting advanced glycation end products are glucosepane, pentosidine, glyoxal-derived hydroimidazolone 1 (GH-1), methylglyoxal-derived hydroimidazolone 1 (MG-H1), $N\varepsilon$-(carboxymethyl)-lysine (CML), $N\varepsilon$-(carboxyethyl)-lysine (CEL) and 3-deoxyglucosone-derived hydroimidazolone 1 (3DG-H1). Figure adapted from ref. [65].

1.3.1 Formation of methylglyoxal and methylglyoxal-derived advanced glycation end products

Glyceraldehyde-3-phosphate and dihydroxyacetone phosphate are the two intermediate products that are formed in glycolysis from fructose 1,6-bisphosphate,

and are the main source for methylglyoxal (Figure 7), which is the most reactive precursor of AGEs.[66] Around 0.05-0.10% of these triosephosphates form non-enzymatically to MG.[67] The main MG-derived AGEs are the hydroimidazolones MG-H1, MG-H2 and MG-H3, that are formed in a Maillard reaction of methylglyoxal with arginine side chains of proteins.[63,68,69] Minor MG-derived AGEs that form on arginine residues are argpyrimidine[70] and tetrahydropyrimidine[71]. MG can also bind to lysine residues, leading to the formation of carboxyethyl-lysine (CEL).[63] There is a naturally occurring endogenous detoxification system, that disposes of MG: GLO1 and GLO2 are two glyoxalases that catalyze the conversion of MG to S-lactoylgluthathione to render it harmless.[72] However, when abnormally high levels of MG are formed, GLO1 activity can be saturated, thereby leading to increased MG-derived AGE formation.[73] Besides the GLO1 system, aldo-keto reductases (AKRs) and aldehyde dehydrogenases (ALDHs) were described to detoxify methylglyoxal.[74]
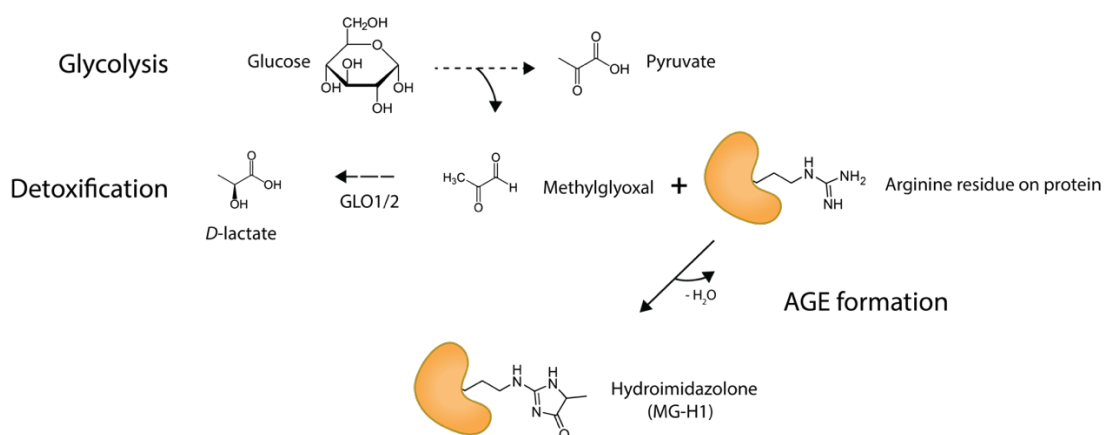
Figure 7 Formation of methylglyoxal (MG) and the advanced glycation end product hydroimidazolone (MG-H1).
Methylglyoxal forms non-enzymatically as a by-product from the two intermediate products glyceraldehyde-3-phosphate and dihydroxyacetone phosphate. MG is a very reactive molecule and will bind to lysine and arginine side chains of proteins to form the advanced glycation end product MG-H1. The glyoxalases GLO1 and GLO2 are two detoxification enzymes, that convert MG to harmless D-lactate.

1.3.2 Effects of AGEs

The harmful effects of advanced glycation end products can be categorized as receptor-dependent and -independent (Figure 8).

Receptor-dependent effects occur after activation of intracellular signaling pathways by binding to the receptor for advanced glycation end products (RAGE).[75] After binding to RAGE, the NF-KB (nuclear factor kappa-light-chain-enhancer of activated B cells) signaling cascade is activated, inducing the transcription of *RAGE* itself, vascular endothelial growth factor (*VEGF*), interleukin 6 (*IL-6*), vascular adhesion molecule 1 (*VCAM1*) and tumor necrosis factor alpha (*TNF-alpha*), which generates inflammatory reactions.[76–80]

AGE-modified extra- and intracellular proteins can have an altered structure and function. Cross-linking of ECM (extracellular matrix) proteins like collagens and elastin results in arterial stiffness and decreased endothelial cell adhesion.[81–84] Due to their low turn-over rate, modifications on long-lived proteins are even more deleterious to the cells and tissues if they are not immediately addressed by the cell's repair machinery. Furthermore, the stability or half-life of the precursor itself can also play an important role. The half-life of MG-H1 is 2-3 weeks.[85,86] The stability of glucosepane is at least three weeks.[87]
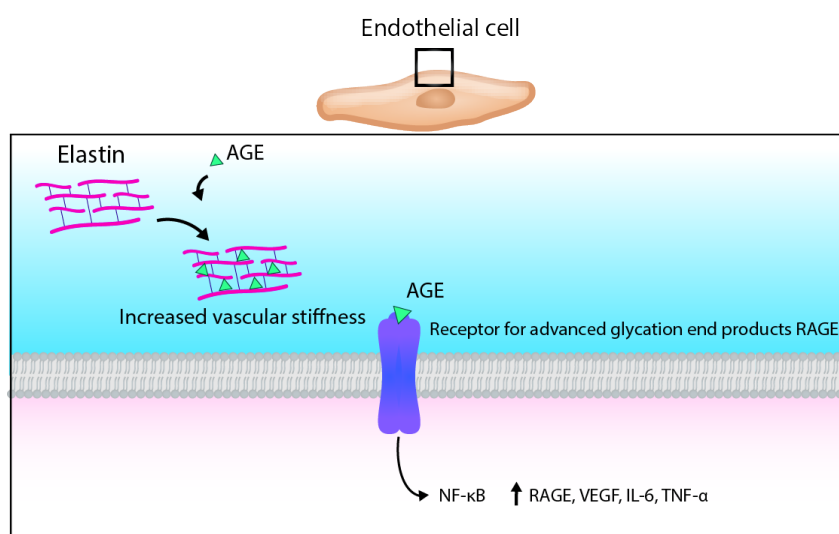
Figure 8 Extracellular and intracellular effects of advanced glycation end products (AGEs).
In the extracellular matrix, advanced glycation end products can cross-link collagen or elastin fibers, which increases the vascular stiffness, that makes it more prone to leaks or damages. AGEs also bind to their respective receptor RAGE (receptor for advanced glycation end products) that initiates the NF-KB (nuclear factor kappa-light-chain-enhancer of activated B cells) signaling cascade intracellularly, inducing the expression of *RAGE*, vascular endothelial growth factor (*VEGF*), vascular adhesion molecule 1 (*VCAM1*), interleukin 6 (*IL-6*) and tumor necrosis factor alpha (*TNF-alpha*).

1.3.3 Methylglyoxal in diabetes and disease

Many studies have linked MG or MG-derived AGEs to be part of the development of various diseases, such as Alzheimer's disease[88], Parkinson's disease[89], rheumatoid arthritis[90] and especially of diabetes, since the formation of MG increases proportionally with increasing glucose availability.[91]

MG and the other AGE precursors 3-deoxyglucosone and glyoxal, were all found to be elevated in serum of diabetic patients.[92–94] MG-H1 and MG-H2 were detected in human lens proteins, potentially contributing to aggravated protein aggregation, ROS (reactive oxygen species) production and worsening of the symptoms present in patients with cataract.[95] Another study found increased MG-H1 serum levels of patients with diabetic retinopathy.[96] Furthermore, in serum of non-diabetic patients with uremia, MG-derived AGEs were elevated.[97]

The implication of AGEs in the formation or exacerbation of diabetic nephropathy and diabetic kidney disease has been investigated in many studies. AGE formation, especially hyperglycemia-related AGEs have been shown to be a hallmark for the development of diabetic kidney disease. The AGE-mediated mechanisms that are involved in the pathology of diabetic kidney disease (glomerulosclerosis, glomerular basement membrane thickening, mesangial expansion, podocyte permeability) include increase of oxidative stress, induction of cytokines and inflammatory processes and altered proteasome-mediated degradation.[98–103]

The exact underlying mode-of-action how MG or its derivates contribute to the emergence or progression of these diseases remains to be identified. One frequently discussed mechanism is the potential of MG to change the stability and structure of the protein conformation by changing the physicochemical properties after binding to arginine and lysine residues.[69,104,105] That could result in misfolding of the protein and thereby lead to a decrease or complete inactivation of the protein function.[106–108]

1.4 Heat-shock proteins

Heat-shock proteins (HSP) are molecular chaperones belonging to the cellular protein quality control system, which also includes the proteasome and autophagy.[109] The main functions of HSPs can be categorized as housekeeping and stress-related activities (Figure 9 and Table 2). Housekeeping activities include the folding of newly translated polypeptides into their tertiary structure[110], assembly of protein complexes[111] and transport of proteins across organelle membranes[112]. The

stress-related activities include stabilization of proteins to prevent misfolding or aggregation[113], disaggregation of proteins[114] and guidance of proteins to their degradation *via* the ubiquitin proteasome pathway.[115,116]
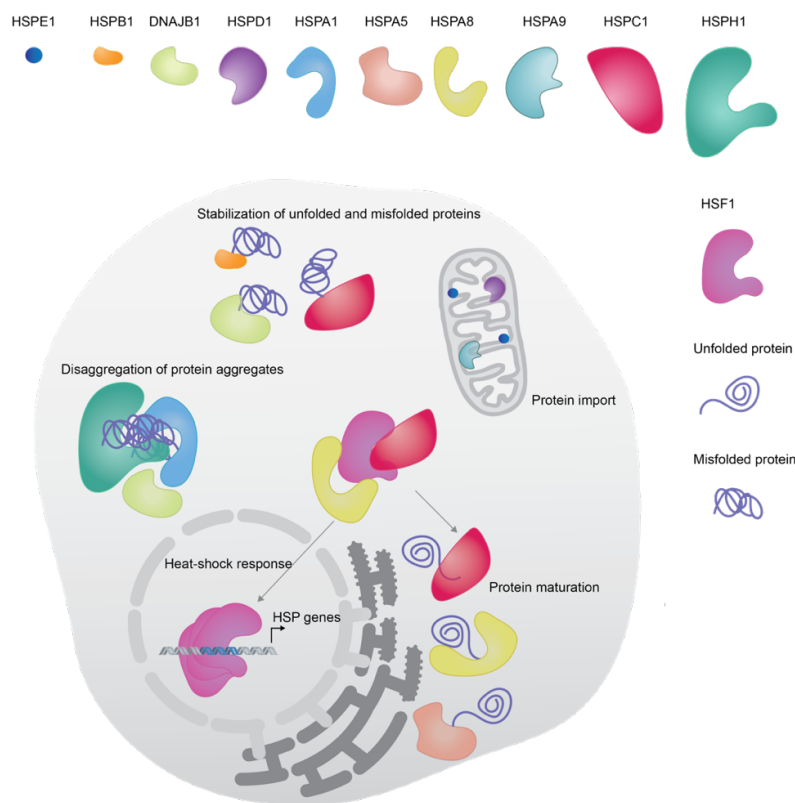
Figure 9 Overview of the mammalian heat-shock proteins and their subcellular location.
HSP= heat-shock protein; DNAJB1= DnaJ homolog subfamily B member 1, HSF1= heat-shock factor 1.

The expression of HSPs is increased when cells are exposed to certain stress conditions, including heat[117], cold[118], ultraviolet radiation[119], ROS, proteotoxic stress[120] or viral infection[121]. Under these stress conditions their main function is to prevent proteins from misfolding, or to refold misfolded proteins.[113,114] Their expression is modulated by the heat-shock response[122]. In unstressed conditions heat-shock factor 1 (HSF1) is bound to HSPA1A/HSPA1B and HSPC1 (Figure 9). Upon, for example, a heat stress, HSF1[123] dissociates from these proteins, homotrimerizes and translocates into the nucleus. There it binds to genomic promotor regions, the so-called heat-shock elements,[124,125] to induce the expression of HSPs.

The *HSP70* family consists of 11 proteins.[126] The best-characterized ones are *HSPA1A* and *HSPA1B*[127], *HSPA5*[128], *HSPA8*[129] and *HSPA9*[130]. *HSP70* family members have a nucleotide binding domain (NBD) at the N-terminus and a substrate

14

binding domain (SBD) at the C-terminus and the domains are connected by a linker.[131,132] The folding mechanism of newly synthesized polypeptides or misfolded proteins (substrates) is dependent on adenosine triphosphate (ATP). The cycle of ATP binding and hydrolysis at the NBD triggers substrate binding and release through conformational changes of HSP70.[133] This process is accompanied by J-domain proteins, that mediate binding of substrates to HSP70, and nucleotide exchange factors that replace adenosine diphosphate (ADP) with ATP.[134,135]

Table 2 List of heat-shock proteins, their function and subcellular location.

Heat-shock protein or co-chaperone	Aliases	Function	Location
HSPE1	HSP10	Folding and stabilization of imported proteins[136]	Mitochondria
HSPB1	HSP27	Stabilization of proteins[137], protection from oxidative stress[138]	Cytoplasm, nucleus
DNAJB1	HSP40	Assists HSPA1A and HSPA1B in protein folding[139]	Cytoplasm, nucleus
HSPD1	HSP60	Folding and stabilization of imported proteins[136,140]	Mitochondria
HSPA1A	HSP70-1	Folding and stabilization of proteins[141]	Cytoplasm, nucleus
HSPA1B	HSP70-2	Folding and stabilization of proteins[141]	Cytoplasm, nucleus
HSPA5	GRP78	Protein folding[142]	Endoplasmic reticulum, cytoplasm
HSPA8	HSC70	Protein folding, formation of protein complexes[141]	Cytoplasm, nucleus
HSPA9	mtHSP70, mortalin	Protein import[143]	Mitochondria

HSPC1	HSP90AA1	Folding and stabilization of proteins[144]	Cytoplasm, nucleus
HSPH1	HSP105 HSP110	Nucleotide exchange factor for HSPA1A and HSPA1B[139]	Cytoplasm

The HSPs, HSPE1, HSPD1 and HSPA9 are all expressed in mitochondria and are involved in folding, stabilization and import of proteins into the mitochondrial membranes.[136,140,143] The expression of the latter can also be used as an indicator of mitochondrial health and homeostasis, including mitochondrial biogenesis.

1.4.1 Heat-shock proteins in diabetes and diabetic nephropathy

The involvement of HSPs in diseases that are characterized by increased oxidative stress, protein misfolding, protein aggregation or inflammation, has been studied extensively, for example in Alzheimer's disease[145] and cancer[146].

In diabetes, as well as diabetic animal models, HSPs were also observed to be either lower or higher expressed in various tissues and cell types, as compared to healthy controls. The expression and phosphorylation of HSPB1, which acts protective under oxidative stress and can inhibit apoptosis[147] was increased in podocytes, as well as in the retina in experimental diabetes mellitus.[148,149] In the kidneys of STZ-induced (streptozotocin) diabetic rats, the three HSPs HSPD1, HSPB1 and HSPA1A were all overexpressed, but mainly in the outer medulla.[150] However, it is worth to mention, that not all studies attain the same results. For instance, another study found *Hspd1* to be downregulated in renal tissue of diabetic rats.[151] In a series of experiments HSPs were shown to be higher expressed in renal tubular cells upon treatment with high-glucose and different AGEs.[152–154] With the advances made in the last decade in next generation sequencing approaches, more and more links of diseases and gene polymorphisms in genes were detected and associated with certain diseases. Various studies have linked genetic polymorphisms of *HSPA1A* and *HSPA1B* to the development of diabetes or diabetes-related complications.[155–158]

1.5 Mitochondria

Mitochondria are organelles with a mean size of approximately 1.4 µm^2.[159] Their shape can be round or rod-like, and they are mostly interconnected. They form a

three-dimensional tubular network inside the cell and are evenly spread throughout the cytoplasmic space. Their composition varies from most other organelles, in that they are built with a double membrane structure (Figure 10). The outer mitochondrial membrane (OMM) encapsulates the mitochondria from the cytosol. Inside is a second membrane, the inner mitochondrial membrane (IMM), that encapsulates another compartment, called the mitochondrial matrix. The space in between the two membranes is called intermembrane space. Aside from the nucleus, mitochondria are the only organelles, that also contain DNA in the form of mitochondrial DNA (mtDNA) and a protein translation machinery.[160] However only 13 proteins are encoded in the mtDNA, alongside two ribosomal RNAs (rRNAs) and 22 transporter RNAs (tRNAs).[161] Therefore, most of the mitochondrial proteins are encoded in nuclear DNA and have to be transported to the mitochondria. This is facilitated, amongst others, by the HSPs, HSPD1 and HSPA9.[140,143] The IMM is folded, which increases the surface area of the mitochondrial matrix, where important metabolic processes, like the citric acid cycle and oxidative phosphorylation are carried out to produce adenosine triphosphate (ATP).
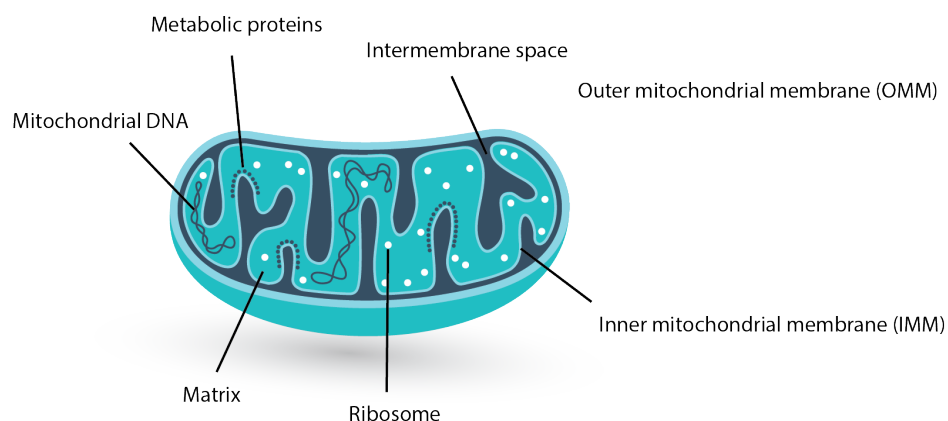
Figure 10 Structure of a mitochondrion.
Mitochondria are organelles, that are organized by two membranes, the outer mitochondrial membrane and the inner mitochondrial membrane. The space in between the two membranes is called intermembrane space. The space inside the inner mitochondrial membrane is called matrix. It contains the proteins, that are relevant for the energy conversion processes of the citric acid cycle and oxidative phosphorylation. The matrix also contains mtDNA and ribosomes, for transcription and translation of mitochondrial proteins.

Mitochondria provide the cells with energy. In the mitochondrial matrix, they convert pyruvate and acetyl-CoA (Coenzyme A), that are produced during glycolysis and the fatty acid metabolism, to guanosine triphosphate, nicotinamide adenine dinucleotide

(NAD) and flavin adenine dinucleotide (FAD). This series of enzymatic reactions is called the citric acid cycle.[162] NADH and FADH2 are then further metabolized during oxidative phosphorylation in the IMM, which results in the production of ATP.[163] The energy-converting process of oxidative phosphorylation is a major source for ROS generation in the form of free radicals.[164] These were shown to be elevated in diabetic patients and can impair mitochondrial function.[165,166]

1.5.1 Mitochondrial homeostasis

The mitochondrial network is highly dynamic and constantly reshaping. It can react to changes in metabolic demand, as well as, to proteotoxic and cellular stresses.[167,168] It reshapes *via* four main processes, mitochondrial fusion and fission, mitochondrial biogenesis, and mitophagy.

1.5.1.1 Mitochondrial fusion and fission

Mitochondrial fusion and fission are the two ways for a cell to quickly react to dysfunctional parts of the mitochondria. Mitochondrial fusion is important to ensure mtDNA stability. In a process called genetic complementation, the cell can fuse two mitochondria, that have different genetic defects, in a way that they can complement each other and thus bypass their deficiency.[169] If the damage of a mitochondrion is beyond repair, cells can selectively isolate this part through mitochondrial fission and then target it to autophagosomal degradation.

Mitochondrial fusion is carried out in a two-step process (Figure 11A). First, the outer mitochondrial membranes of two single mitochondria are tethered by outer mitochondrial membrane proteins, the two mitofusins MFN1 and MFN2.[170] In the second step, the inner mitochondrial membrane protein optic atrophy 1 (OPA1) fuses the IMM.[171]

The key protein in mitochondrial fission (Figure 11B) is dynamin-related protein 1 (DRP1) or dynamin-1-like protein (DNM1L). First, DRP1 is recruited by adaptor proteins in the OMM to the mitochondrial surface.[172] Then, DRP1 oligomerizes in a ring-like structure around the mitochondrion and mediates membrane scission *via* constriction.[173,174]

18
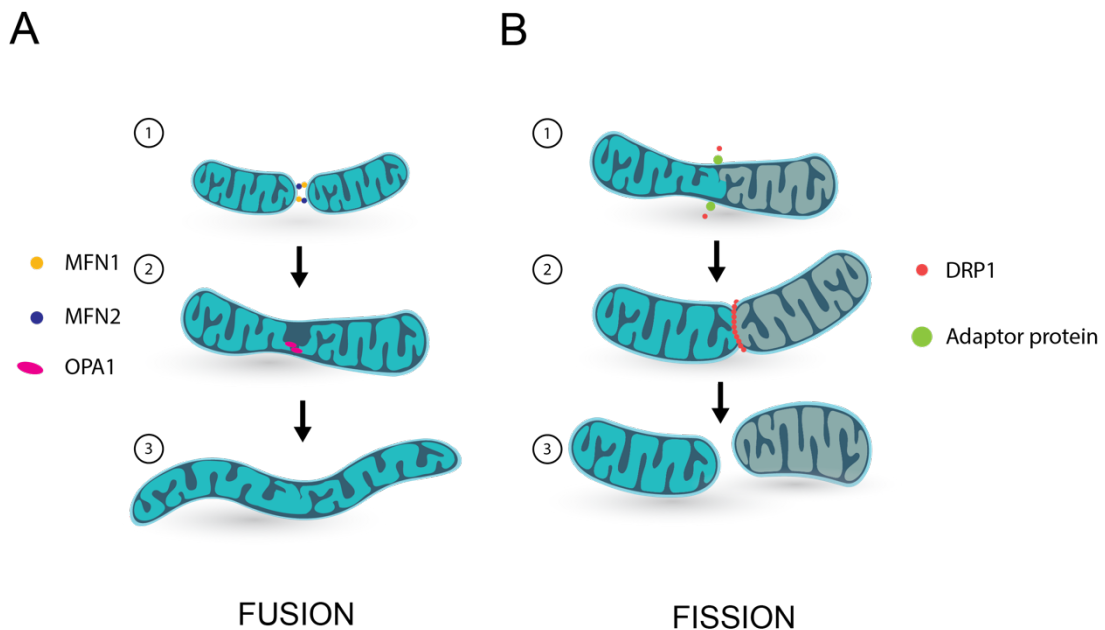
Figure 11 Mitochondrial fusion and fission.
(A) In the first step of mitochondrial fusion the mitofusins 1 and 2 (MFN1 and MFN2) tether two single mitochondria together and fuse the outer mitochondrial membranes. In the second step, optic atrophy protein 1 (OPA1) fuses the inner mitochondrial membrane. (B) In the first step of mitochondrial fission, DRP1 is recruited to mitochondria by adaptor proteins. In the second step, DRP1 oligomerizes and forms a ring-like structure around the location where the mitochondrion is split, *via* constriction. The result are two single mitochondria, of which one potentially is going to be degraded *via* mitophagy.

1.5.1.2 Mitochondrial biogenesis

Through mitochondrial biogenesis, cells can react to an increase in energy demand by producing new mitochondria. Peroxisome proliferator activated receptor gamma coactivator 1 alpha (*PGC1A)* is considered the master regulator of mitochondrial biogenesis.[175] It is a transcription factor, that induces the transcription of many genes related to mitochondrial DNA transcription and synthesis, like nuclear respiratory factor 1 and 2 (*NRF1*, *NRF2*), mitochondrial transcription factor 1 (*TFAM)* and transcription factor B2 mitochondrial, (*TFB2M)*.[176,177] Furthermore, the expression of the protein translocation machinery, that facilitates protein transport into mitochondria and transport in between mitochondrial compartments is induced. To this class belong the TOMM (translocase on the outer mitochondrial membrane) and the TIMM (translocase of inner mitochondrial membrane) proteins in cooperation with HSPA9.[178,179]

1.5.1.3 Mitophagy

Mitophagy is the degradation process for defective mitochondria. There are several ubiquitin-dependent and ubiquitin-independent pathways that regulate mitophagy (Figure 12). Under non-stress conditions, PTEN-induced putative kinase protein 1 (PINK1), a serine/threonine kinase, is cleaved in the mitochondria, followed by export and degradation.[180–182] Damaged mitochondria, however, become depolarized. After this reduction of the membrane potential of the OMM, PINK1 remains on the OMM, where it auto-phosphorylates and homodimerizes.[183,184] PINK1 then phosphorylates ubiquitin on several proteins on the OMM, that leads to the recruitment of Parkinson juvenile disease protein (PARKIN), that is subsequently activated by phosphorylation of PINK1.[185] Activated PARKIN then continues ubiquitination on OMM proteins, that lead to the recruitment of mitophagy receptor prohibitin-2 (PHB2) and microtubule-associated protein 1 light chain 3 alpha (LC3) and the degradation of the mitochondrion.[186,187] Another pathway, that is ubiquitin-independent, is mediated through BCL2/adenovirus E1B 19 kDa protein-interacting protein 3 (BNIP3), whose overexpression alone results in triggering mitophagy through loss of membrane potential.[188,189]
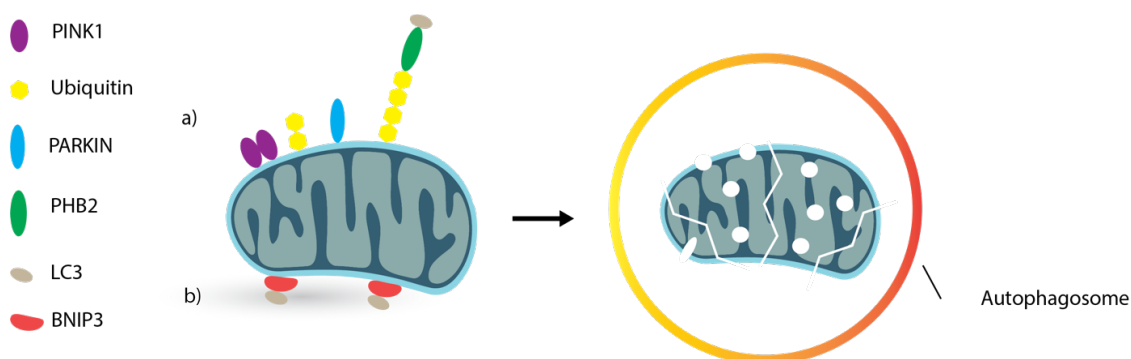
Figure 12 Illustration of two mitophagy pathways.
Degradation of mitochondria is initiated through a series of events. There are (a) ubiquitin-dependent and (b) ubiquitin-independent pathways. a) In the PINK1-PARKIN mediated ubiquitin-dependent mitophagy, PTEN induced putative kinase protein 1 (PINK1) stabilizes and dimerizes on the outer mitochondrial membrane after a depolarization of the membrane occurred. PINK1 then ubiquitinates OMM proteins, which leads to the recruitment of Parkinson juvenile disease protein (PARKIN), which is subsequently phosphorylated by PINK1. PARKIN then ubiquitinates further OMM proteins, that recruit mitophagy receptor prohibitin 2 (PHB2) and microtubule associated protein 1 light chain 3 alpha (LC3), which induces autophagosome formation. b) A ubiquitin-independent pathway is mediated through the interaction of BCL2/adenovirus E1B 19 kDa protein interacting protein 3 (BNIP3) and LC3 on the OMM.

1.5.2 Mitochondria in diabetes

Disturbances of the highly regulated mitochondrial homeostasis or energy metabolism can lead to defects and diseases. Hyperglycemia was reported to induce mitochondrial fragmentation through the fission machinery, essentially reacting to the increase in mitochondrial respiration and overproduction of reactive oxygen species from increased glucose metabolism.[190,191] A single point mutation in the overlapping genes encoding for the subunit of mitochondrial ATP synthase *MT-ATP6* and MT-*ATP8* (from C to G, at m.8561) of complex V has been shown to cause a diabetes-like phenotype due to a decreased ATP production.[192] Mitochondrial dysfunction has been linked to cause insulin resistance and impaired insulin secretion in diabetes patients.[193]

In an obesity study, the mitochondrial metabolic parameters were assessed from twin pairs, where one was lean, and one was obese.[194] In subcutaneous adipose tissue of the obese participants, they found a downregulation of oxidative phosphorylation proteins and lower mtDNA amounts compared to their lean twins. Additionally, they showed that mitochondrial biogenesis was reduced, through downregulation of *PGC1A* expression. That could eventually lead to mitochondrial dysfunction and insulin resistance as explained above. Two other studies made the same observation of a downregulation of *PGC1A* and *NRF1* induced genes.[195,196]

Disturbances of the crucial mitochondrial metabolism pathways, like the citric acid cycle, fatty acid oxidation and ATP production through oxidative phosphorylation have been linked to diabetic kidney disease.[197–200]

1.6 Aim of the project

Advanced glycation end products and heat-shock proteins have been associated with various diseases. However, the exact mode how they contribute to the development or progression of these diseases, especially diabetic nephropathy remains unknown. The aims of this study were:

1. Investigate the effects of dicarbonyl stress, in the form of methylglyoxal and the resulting advanced glycation end product MG-H1 in endothelial cells. This was accompanied by a loss-of-function study for the HSPA1A and HSPA1B proteins to elucidate the importance of HSPA1A/HSPA1B in the occurrence of diabetes-related endothelial stress.

2. Investigate if the loss of HSPA1A/HSPA1B protein expression aggravates the diabetic nephropathy symptoms in a streptozotocin-induced diabetic mouse model and evaluate HSPA1A/HSPA1B as a potential target for the treatment of diabetic nephropathy.

2 RESULTS

2.1 Generation of a *Hspa1a/Hspa1b* gene knockout cell line

Initially, it was planned to perform a double gene knockout (KO) of the two stress-inducible *Hsp70* variants *Hspa1a* and *Hspa1b*. Therefore, two plasmids were used, for the CRISPR/Cas9-mediated genetic modification for the two respective genes. The analysis of the genetically modified mouse cardiac endothelial cell line (MCEC) showed a knockout of both genes on the mRNA level (Figure 13A), and a significant reduction on the protein level to 0.1-fold (Figure 13B). Even after a heat-shock experiment, HSPA1A and HSPA1B expression only showed an increase in the wild-type (WT) cell line. The faint protein band for the KO cell lines, that remained on the western blot, was determined to be unspecific binding of the polyclonal anti-HSPA1A antibody to HSPA1L (Figure 13C). For this, recombinant HSPA1L protein, kindly provided by Prof. Dr. Matthias Mayer, was loaded on the SDS-PAGE and detected with the anti-HSPA1A antibody. To verify the knockout on the genome level, the DNA loci around the CRISPR/Cas9 modification site was sequenced via next generation sequencing. For the three independent knockout cell clones AD4, BE12 and BH9 the results showed a deletion of 2, 10 and 23 bases, which resulted in a shift of the open reading frame, leading to a functional gene knockout (Figure 13D). However, in all three cell lines no reads were produced for the *Hspa1b* gene. Therefore, the genomic sequences around the *Hspa1a* and *Hspa1b* genes were amplified. The result showed that the wild-type MCEC line does not contain the *Hspa1b* gene, as here only the flanking sites of the gene were amplified (Figure 13E). Based on this result, all following experiments only mention the differences of wild-type and *Hspa1a* knockout in the endothelial MCEC line.
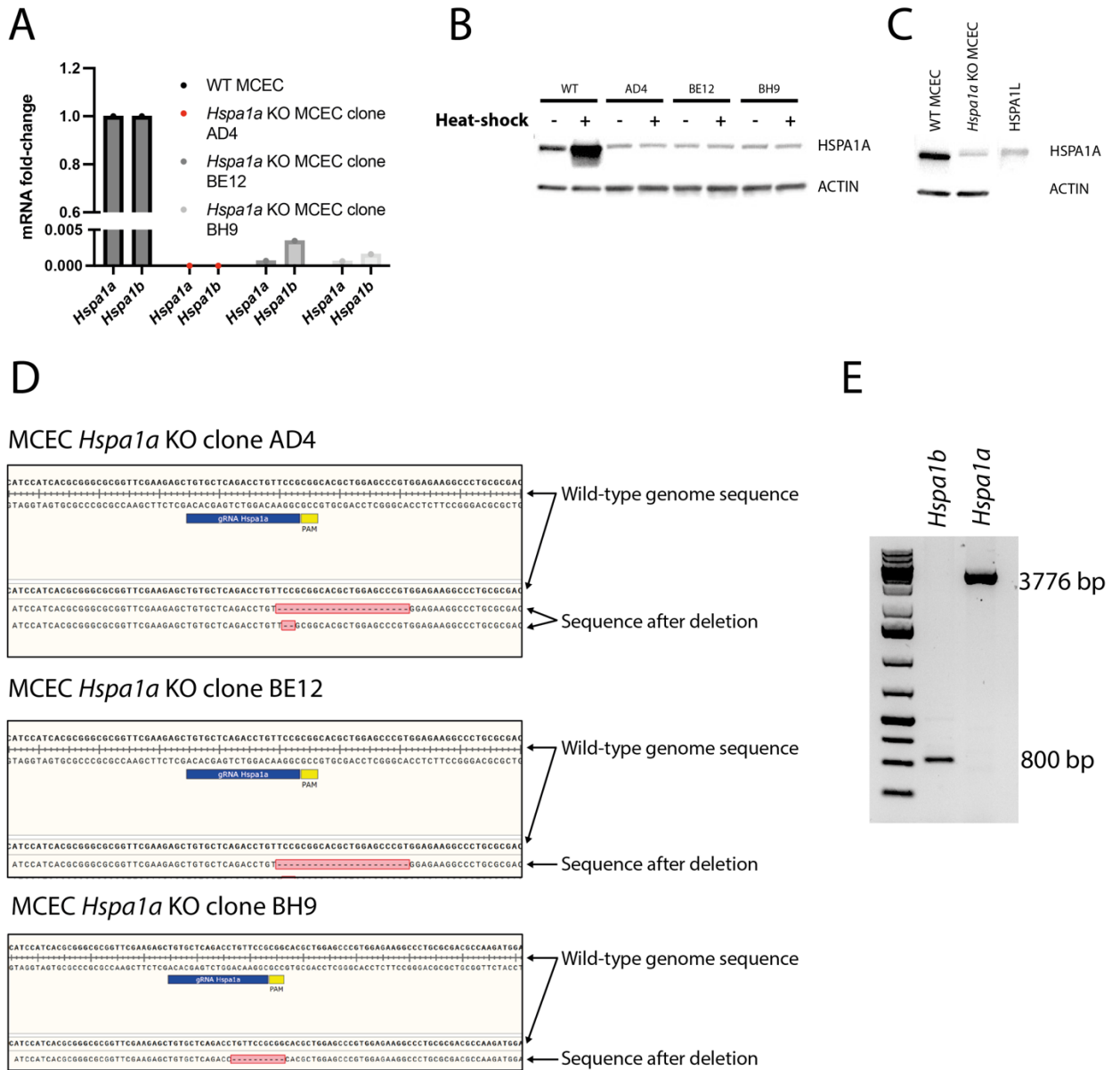
Figure 13 Validation of the *Hspa1a/Hspa1b* gene knockout in mouse cardiac endothelial cells.
(A) *Hspa1a* and *Hspa1b* expression was measured in wild-type and *Hspa1a/Hspa1b* knockout MCEC lines (B) HSPA1A expression in the respective cell lines with and without heat-shock treatment. (C) The remaining faint protein band in the western blot is caused by unspecific binding of the anti-HSPA1A antibody to HSPA1L. Recombinant HSPA1L was provided by Prof. Dr. Matthias Mayer. (D) Genome sequencing on the three *Hspa1a* knockout MCEC cell lines AD4, BE12 and BH9 showed a deletion of the *Hspa1a* sequence of 2, 23, and 10 nucleotides, resulting in the functional gene knockout. Next generation sequencing was performed by Dr. Rebekka Medert. (E) DNA amplification of the respective genome sequences show that wild-type mouse cardiac endothelial cells do not contain the *Hspa1b* gene.

2.2 Effects of acute and chronic methylglyoxal stress in endothelial cells

2.2.1 Effect of methylglyoxal on cell viability

At high concentrations, MG is a cytotoxic compound that, if not removed or metabolized by the cell, can increase proteotoxic and oxidative stress. Therefore, it was investigated at what concentrations acute MG stress had an influence on cell viability. For this, WT and *Hspa1a* KO MCEC were treated with different concentrations of MG for 24 hours. Then, a CellTiter-Glo® cell viability assay was performed to measure the median effective dose (ED50) for all cell lines. The CellTiter-Glo® assay measures the cell viability through a conversion of the reporter molecule luciferin into oxyluciferin *via* cellular ATP.[201] The ED50 for the wild-type MCEC was 980 µM of MG (Figure14). The ED50 for the *Hspa1a* knockout cell lines was 862.6 µM of MG. The difference of the ED50 between the WT and KO cells was not statistically significant. At a concentration of 500 µM MG, the cell's viability started to deteriorate. Thus, for all following experiments a concentration of 500 µM MG was used.
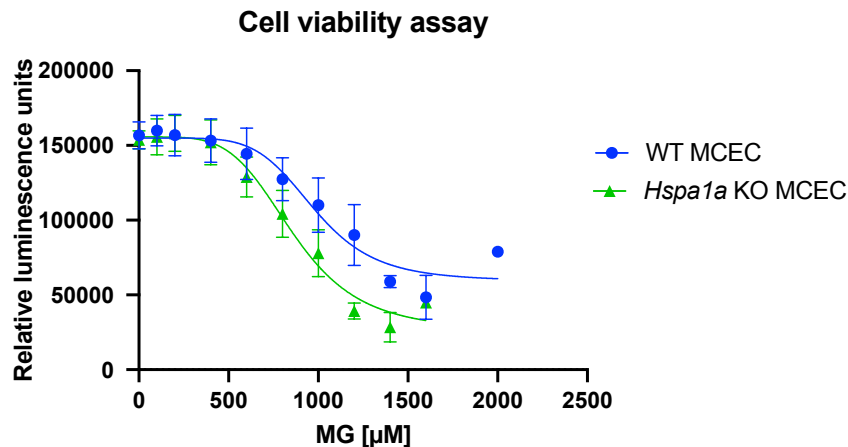
Figure 14 CellTiter-Glo® luminescent cell viability assay.
Wild-type and three different *Hspa1a* knockout mouse cardiac endothelial cell lines (MCEC) were treated with various concentrations of methylglyoxal for 24 hours, followed by a CellTiter-Glo® luminescent cell viability assay. ED50 for the wild-type MCEC was 980 µM methylglyoxal. ED50 for the *Hspa1a* knockout MCEC was 862.6 µM methylglyoxal. Data represent mean ± SD of three independent biological replicates.

2.2.2 Cellular MG-H1 accumulation and clearance

MG-derived post-translational modifications have been shown to induce protein misfolding or loss of protein function. Heat-shock proteins are chaperone proteins, that inhibit a misfolding or aggregation upon binding, or guide misfolded or aggregated proteins to the proteasomal degradation pathway. In the next experiment, it was determined, whether *Hspa1a* deficient cells accumulate increased concentrations of MG-H1 modified proteins upon MG treatment. For this, WT and *Hspa1a* KO cells were stressed for 24 hours with 500 µM MG. Then, MG-H1 modified proteins were detected with an anti-MG-H1 antibody *via* fluorescence widefield microscopy (Figure 15A). Compared to control conditions, WT MCEC had a 3-fold increase (p=0.0019) of MG-H1 signal, whereas *Hspa1a* KO cells had a 5.5-fold increase (p<0.0001) of MG-H1 signal. The amount of MG-H1 modified proteins was indeed increased in *Hspa1a* KO cells, compared to WT MCEC (p=0.0030). To check, whether the degradation of MG-H1 modified proteins was also impaired in *Hspa1a* KO MCEC, a MG-H1 clearance assay was performed. Again, WT and *Hspa1a* KO MCEC were stressed with 500 µM MG for 24 hours. Then, the MG-containing assay medium was removed and replaced with normal assay medium. Cells were fixed directly after medium change, or after a further incubation of another 24 and 48 hours. MG-H1 modified proteins were detected with an anti-MG-H1 antibody *via* an in-cell western blot (Figure 15B). As in the previous experiment, the *Hspa1a* KO MCEC accumulated higher concentrations of MG-H1 modified proteins compared to the WT MCEC (3.3-fold vs. 9.6-fold; p=0.0002). The amount of MG-H1, 24 hours and 48 hours after medium change was reduced to 0.4-fold (p=ns) and to 0.55-fold (p=ns) for the WT cells, respectively. The reduction of MG-H1 modified proteins in the *Hspa1a* KO cells, 24 and 48 hours after medium change, was 3.3-fold (p<0.0001). Therefore, it was concluded, that the clearance of MG-H1 modified proteins is at least as efficient in WT as in *Hspa1a* KO MCEC and is not dependent on the presence of HSPA1A.
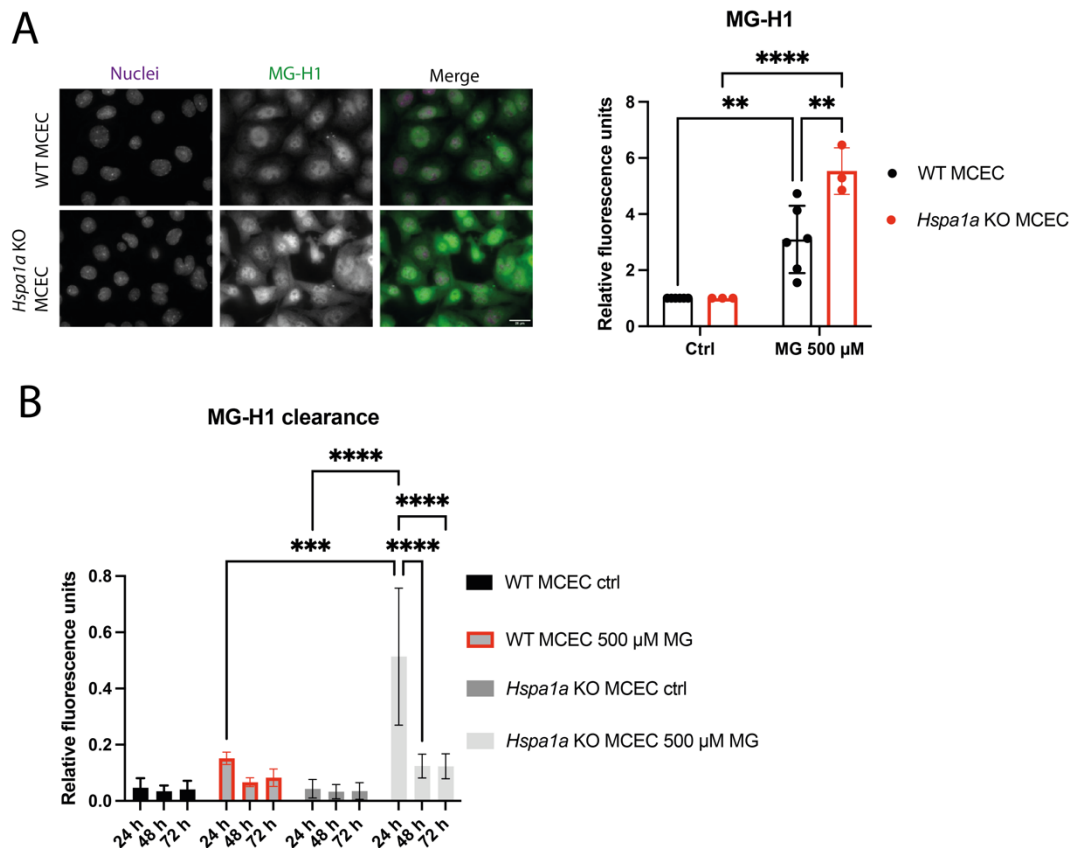
Figure 15 MG-H1 fluorescence microscopy and MG-H1 clearance assay.
(A) WT and *Hspa1a* KO MCEC were treated with 500 µM MG for 24 hours. MG-H1-modified proteins were labeled with an anti-MG-H1 antibody and detected *via* fluorescence microscopy. Scale bar = 20 µm. (B) Wild-type and three different *Hspa1a* knockout mouse cardiac endothelial cell lines (MCEC) were treated with 500 µM of methylglyoxal for 24 hours. 24 hours, 48 hours, and 72 hours after replacing the MG-medium with normal assay medium cells were fixed and stained with anti-MG-H1 antibody for an in-cell western blot using the Odyssey® DLx Imaging system. Data represent mean ± SD, analyzed by a two-way ANOVA statistical test followed by comparing all groups using Sidak`s multiple comparison test. **$p \leq 0.01$, ***$p \leq 0.001$, ****$p \leq 0.0001$.

2.2.3 Changes in mRNA expression upon acute methylglyoxal stress

Based on the hypothesis that the loss of HSPA1A expression leads to an increased proteotoxic stress, changes in mRNA expression of other members of the heat-shock protein family were investigated. Furthermore, genes that are related to oxidative stress, general inflammation and atherosclerosis were analyzed.

WT and *Hspa1a* KO MCEC were stressed once (acute stress) with 500 µM MG. After 12 hours, total RNA was isolated, and the mRNA expression changes were analyzed (Figure 16). *Hspa1a* mRNA expression in the wild-type cells was 2.24-fold increased

(p=0.0298) upon acute MG stress, as compared to controls. *Hspc1* expression was increased in both cell lines, however not statistically significant. *Hspb1* expression was reduced upon MG treatment to 0.73-fold (p=0.0095) in the WT MCEC and to 0.48-fold (p=0.0185) in the *Hspa1a* KO MCEC compared to their respective controls. HSPH1 and the co-chaperone DNAJB1 are important for protein disaggregation together with HSPA1A, and the mRNA expression was unchanged in the WT and *Hspa1a* KO MCEC. The expression of the two mitochondrial heat-shock proteins *Hspd1* and *Hspa9*, which are involved in mitochondrial protein transport, were increased; in the WT MCEC, *Hspa9* expression after MG stress was increased 1.8-fold (p=0.0193), whereas in the *Hspa1a* KO MCEC it was increased by 2.2-fold (p=0.0239) as compared to the respective controls. *Hspd1* mRNA expression was increased 3.19-fold (p=0.0016) in the WT MCEC after MG treatment. The increase in the *Hspa1a* KO MCEC was not statistically significant for *Hspd1*. The other small mitochondrial heat-shock protein that is expressed in mitochondria, *Hspe1*, was only slightly induced in the WT MCEC (1.21-fold, p=0.0479). Heat-shock factor 1 (*Hsf1*), *Hspa8* and *Hspa5* mRNA expression remained unchanged in all cell lines upon MG treatment as compared to their respective controls. Interestingly, in the control *Hspa1a* KO MCEC, there was a reduced baseline mRNA expression of *Hsf1* (0.32-fold, p=0.0056), *Hspa8* (0.40-fold, p=0.0235), and *Hspb1* (0.46-fold, p=0.0004) as compared to control WT MCEC.
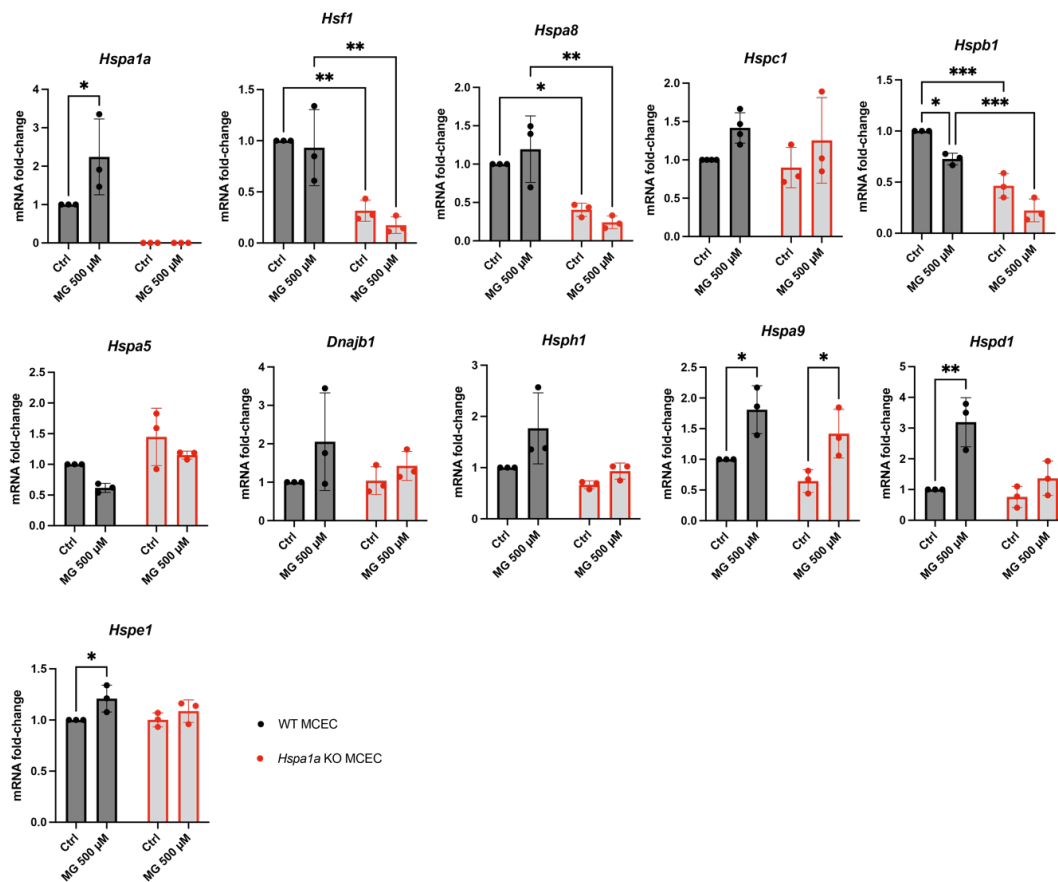
Figure 16 mRNA expression changes of heat-shock proteins after acute MG stress.
Wild-type and three different *Hspa1a* knockout mouse cardiac endothelial cell lines (MCEC) were treated with 500 µM of methylglyoxal for 12 hours. The graphs show the fold-change of mRNA expression of heat-shock proteins after acute MG stress; HSP= Heat-shock protein, *Hsf1*= Heat-shock factor 1, *Dnajb1*= DnaJ homolog subfamily B member 1. Data represents mean ± SD, analyzed by a two-way ANOVA statistical test followed by comparing all groups using Sidak`s multiple comparison test. *$p \leq 0.05$, **$p \leq 0.01$, ***$p \leq 0.001$.

The antioxidant response after oxidative stress is mediated by the transcription factor NRF2[202] and will induce the expression of *NQO1*[203] and *HO1*[204] after binding to antioxidant response elements (ARE) near their gene transcription promotors. Oxidative stress is known to be increased after MG stress.[205] *Nrf2* and *Nqo1* mRNA expression remained unchanged after acute MG stress in the WT and *Hspa1a* KO MCEC (Figure 17A). However, for *Ho1*, there was a decreased expression in the WT MCEC (0.57-fold, p=0.0398) and a 2.62-fold increase in the *Hspa1a* KO MCEC (p=0.0012).

Growth differentiation factor 15 (*GDF15*), vascular cell adhesion molecule 1 (*VCAM1*) and intercellular adhesion molecule 1 (*ICAM1*) are genes that are related to inflammation and atherosclerosis. *Gdf15* was 8.1-fold (p<0.0001) increased after acute MG stress, however only in the *Hspa1a* KO MCEC (Figure 17B). *Vcam1* expression was reduced in both, WT (0.17-fold, p=<0.0001) and *Hspa1a* KO MCEC (0.11-fold, p=0.0012) upon MG stress, whereas *Icam1* mRNA expression was only downregulated in WT MCEC (0.38-fold, p=0.0179).
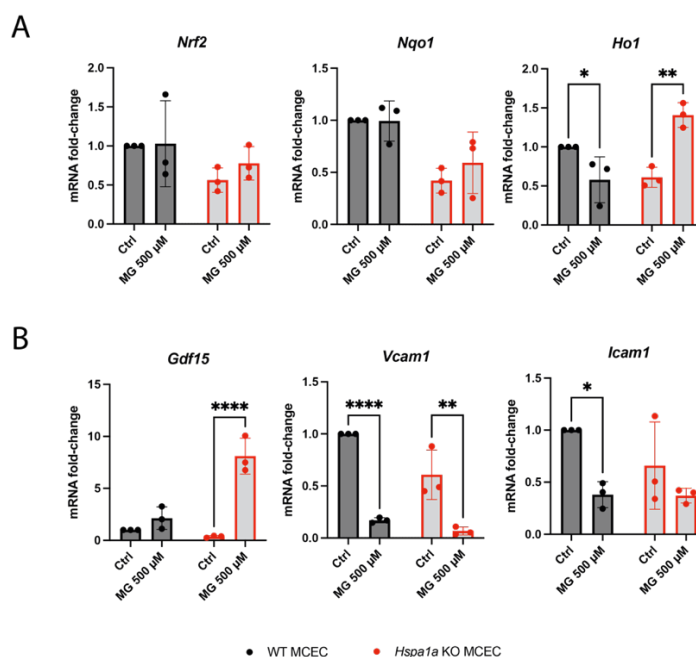
Figure 17 mRNA expression changes of anti-oxidative genes and inflammation markers after acute MG stress.

Wild-type and three different *Hspa1a* knockout mouse cardiac endothelial cell lines (MCEC) were treated with 500 µM of methylglyoxal for 12 hours. (A) The graphs show the fold-change of mRNA expression of anti-oxidative genes after acute MG stress; *Nrf2*= Nuclear factor erythroid 2-related factor 2, *Nqo1*= NAD(P)H dehydrogenase [quinone] 1, *Ho1*= Heme oxygenase 1. (B) The graphs show the fold-change of mRNA expression of genes related to inflammation and atherosclerosis after acute MG stress; *Gdf15*= Growth differentiation factor 15, *Vcam1*= Vascular cell adhesion molecule 1, *Icam1*= Intercellular adhesion molecule 1. Data represents mean ± SD, analyzed by a two-way ANOVA statistical test followed by comparing all groups using Sidak`s multiple comparison test. *p ≤ 0.05, **p ≤ 0.01, ****p ≤ 0.0001.

Since the expression of the two mitochondrial heat-shock proteins *Hspa9* and *Hspd1* was increased upon MG stress, which could potentially point to increased stress or damage in the mitochondria, the induction of other mitochondrial stress-coping mechanisms was analyzed, namely fission and fusion, mitophagy or mitochondrial biogenesis.

On the mRNA level, the key regulator of mitochondrial fission *Drp1* was up to 1.49-fold increased in WT (p=0.0436) but only slightly in *Hspa1a* KO MCEC (p=ns) (Figure 18A). *Fis1*, which is one of the adaptor proteins on the OMM to recruit DRP1, was downregulated in WT (0.51-fold, p=0.0001) and *Hspa1a* KO MCEC (0.37-fold, p<0.0001) after MG stress. The mitochondrial fusion protein *Mfn1* was downregulated to 0.74-fold, but only in the WT MCEC (p=0.0259), whereas *Mfn2* mRNA expression did not change. *Opa1* was downregulated after MG stress in both cell lines, but only statistically significant in the *Hspa1a* KO MCEC (0.79-fold, p=0.0472).

The mRNA expression changes of the mitophagy-related proteins *Pink1*, *Parkin* and *Bnip3* were also analyzed after MG stress (Figure 18B). *Pink1* showed a reduced expression upon MG stress in both cell lines, however this was not statistically significant. Only in the WT MCEC *Parkin* expression was reduced by 0.39-fold (p=0.0139). *Bnip3*, on the other hand, was reduced in both, WT (0.37-fold, p<0.0001) and *Hspa1a* KO MCEC (0.18-fold, p<0.0001). For *Pink1* (0.26-fold, p=0.0052) and *Parkin* (0.42-fold, p=0.0203), the baseline expression in the *Hspa1a* KO MCEC was already reduced, as compared to untreated WT MCEC.

Mitochondrial biogenesis is induced when the cell's energy demand is increased. The transcription factors *Pgc1a* and *Pgc1b*, that regulate mitochondrial biogenesis, were both decreased in the WT MCEC (*Pgc1a*: 0.38-fold, p=0.0017; *Pgc1b*: 0.43-fold, p=0.0002) after MG stress (Figure 18C). Furthermore, the baseline expression of the *Hspa1a* KO MCEC was lower as compared to untreated WT MCEC (*Pgc1a*: 0.39-fold, p=0.0034; *Pgc1b*: 0.31-fold, p<0.0001). *Nrf1* mRNA expression was only induced in the *Hspa1a* KO MCEC upon MG stress (1.62-fold, p=0.0076). *Tfam* expression was decreased in the WT MCEC (0.87-fold, p=0.045), but increased in the *Hspa1a* KO MCEC (1.31-fold, p=0.0006). The transcription factor *Tfb2m* was only induced in the *Hspa1a* KO MCEC (1.94-fold, p<0.0001). The expression of the mitochondrial transport protein on the outer mitochondrial membrane *Tomm7* was not changed upon MG stress. The expression of the mitochondrial transport proteins on the inner mitochondrial membrane *Timm23* and *Timm17a*, were both induced for the *Hspa1a* KO MCEC (*Timm23*: 1.82-fold, p=0.0003; *Timm17a*: 1.56-fold, p=0.0003) and *Timm17a* for the WT MCEC (1.39-fold, p=0.005).
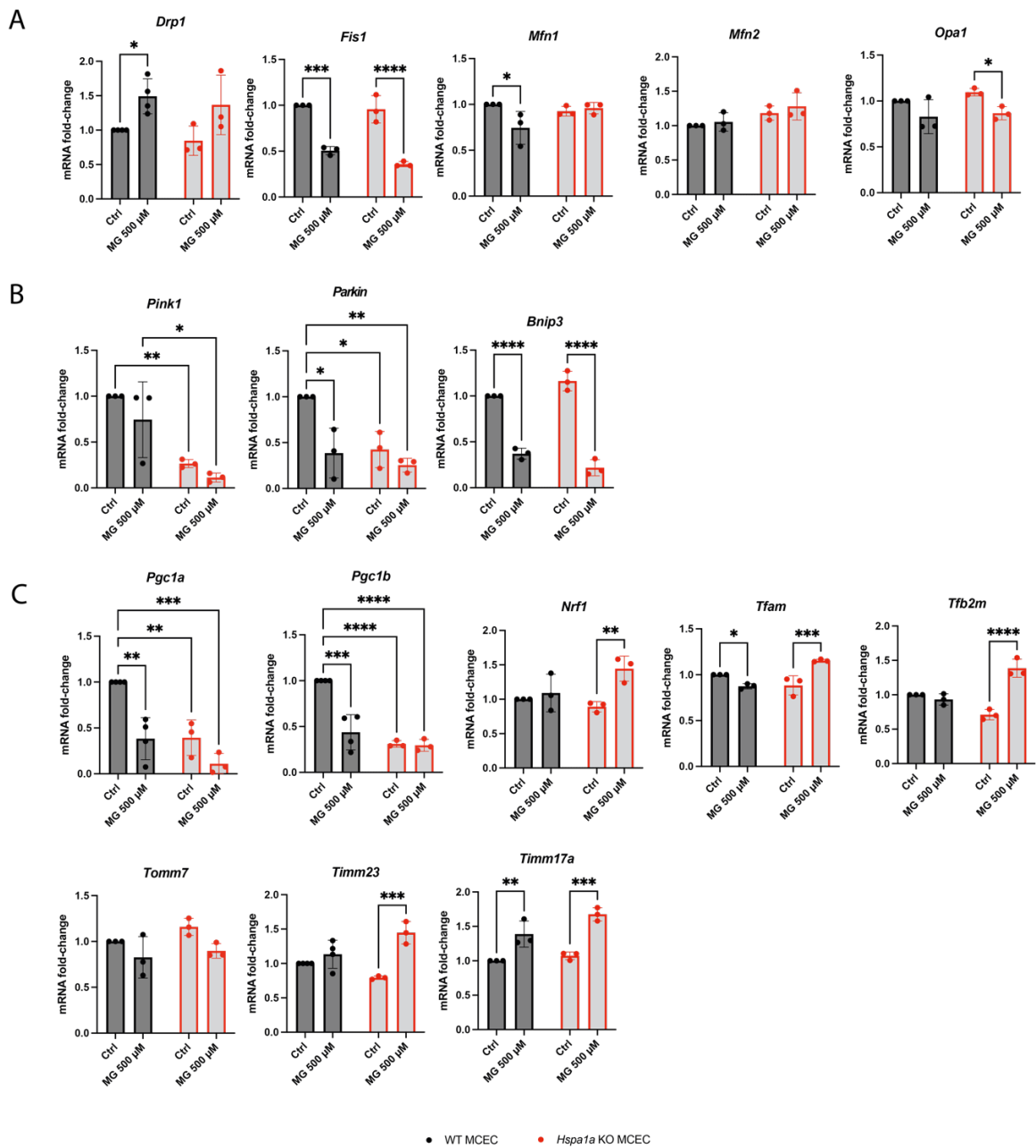
Figure 18 mRNA expression changes of genes related to mitochondrial fusion and fission, mitophagy and mitochondrial biogenesis after acute MG stress.

WT and three different *Hspa1a* KO MCEC were treated with 500 µM of methylglyoxal for 12 hours. (A) The graphs show the fold-change of mRNA expression of the mitochondrial fusion and fission machinery after acute MG stress; *Drp1*= dynamin-related protein 1, *Fis1*= mitochondrial fission protein 1, *Mfn*= mitofusin, *Opa1*= optic atrophy protein 1. (B) The graphs show the fold-change of mRNA expression of mitophagy-related genes after acute MG stress; *Pink1*= PTEN-induced putative kinase protein 1, *Parkin*= Parkinson juvenile disease protein, *Bnip3*= BCL2/adenovirus E1B 19 kDa protein-interacting protein 3. (C) The graphs show the fold-change of mRNA expression of genes that regulate mitochondrial biogenesis after acute MG stress; *Pgc*= peroxisome proliferator-activated receptor gamma coactivator 1,

Figure legend continued from previous page: *Nrf1*= nuclear respiratory factor 1, *Tfam*= mitochondrial transcription factor 1, *Tfb2m*= transcription factor B2, mitochondrial, *Tomm7*= translocase of the outer mitochondrial membrane 7, *Timm*= translocase of the inner mitochondrial membrane. Data represents mean $\pm$ SD, analyzed by a two-way ANOVA statistical test followed by comparing all groups using Sidak`s multiple comparison test. *$p \leq 0.05$, **$p \leq 0.01$, ***$p \leq 0.001$, ****$p \leq 0.0001$.

2.2.4 Methylglyoxal-induced changes in protein expression

As the change in activity of heat-shock proteins cannot be directly inferred from the changes in mRNA expression, the changes in protein expression and subcellular location were analyzed using fluorescence microscopy (Figure 19). Upon acute MG stress, HSPA1A protein expression showed a minor upregulation of 1.56-fold (p=ns). The expression of HSF1 was increased in all cell lines (WT: 1.26-fold, p<0.0001; *Hspa1a* KO: 1.25-fold, p<0.0001). The expression of HSPA8 minimally decreased in *Hspa1a* KO MCEC after acute MG stress (0.81-fold, p=0.033). The protein expression of HSPC1 was 1.61-fold (p<0.0001) increased in WT MCEC and 1.46-fold (p<0.0001) increased in *Hspa1a* KO MCEC after MG stress. The expression of the co-chaperone DNAJB1 was 1.62-fold (p=0.0057) increased in WT MCEC and 1.48-fold (p=0.022) increased in *Hspa1a* KO MCEC. Furthermore, both mitochondrial heat-shock proteins were also upregulated on the protein level. The expression of HSPA9 was 1.80-fold (p=0.0001) increased in WT MCEC and 1.45-fold (p=0.006) increased in *Hspa1a* KO MCEC upon acute MG stress. The expression of HSPD1 was 2.85-fold (p=0.006) increased in WT MCEC and 3.02-fold (p=0.0036) increased in *Hspa1a* KO MCEC. Example fluorescence microscopy images for the protein analysis and subcellular location of the WT and *Hspa1a* KO cell lines can be observed in Figure 45 in the appendix section.
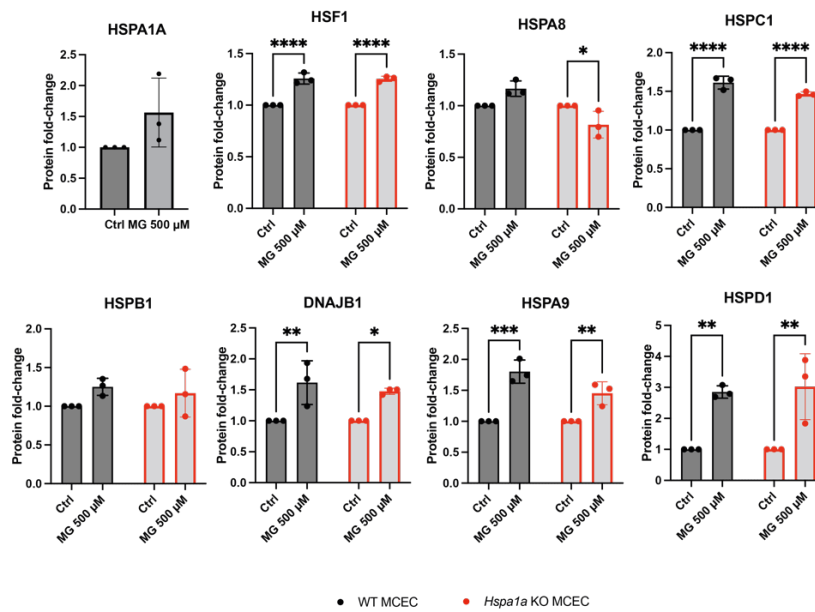
Figure 19 Protein expression changes of heat-shock proteins after acute MG stress.
WT and three different *Hspa1a* KO MCEC were treated with 500 µM of methylglyoxal for 24 hours. Protein expression was measured *via* fluorescence microscopy and normalized to the total number of cells. Data represents mean ± SD. HSPA1A data was analyzed by unpaired t-test with Welch's correction, all other were analyzed by a two-way ANOVA statistical test followed by comparing all groups using Sidak`s multiple comparison test. *p ≤ 0.05, **p ≤ 0.01, ***p ≤ 0.001, ****p ≤ 0.0001.

2.2.5   MG-H1 levels in whole cell lysates and isolated mitochondria

After observing the changes in mitochondrial protein expression, the question arose whether MG-H1 formation on mitochondrial proteins occurs, and if this is increased in the *Hspa1a* KO MCEC. MG-H1 modified proteins were detected in the cytoplasm, especially in the nucleus (Figure 15A). However, the signal intensity was too high to detect a distinct signal in mitochondria. Therefore, mitochondria of MG-stressed WT and *Hspa1a* KO MCEC were isolated and analyzed by western blotting (Figure 20A). An increase in the MG-H1 signal could be observed in the mitochondrial preparations from the MG stressed cells. Next, the protein lysates of control and MG-stressed WT and *Hspa1a* KO MCEC were analyzed for their MG-H1 content with a combined liquid chromatography and mass spectrometry approach (LC-MS/MS). The MG-H1 concentration of MG-stressed *Hspa1a* KO MCEC was 1.46-fold increased (p=0.031) in whole cell protein lysates, and 1.48-fold increased (p=0.035) in mitochondrial protein lysates (Figure 20B).
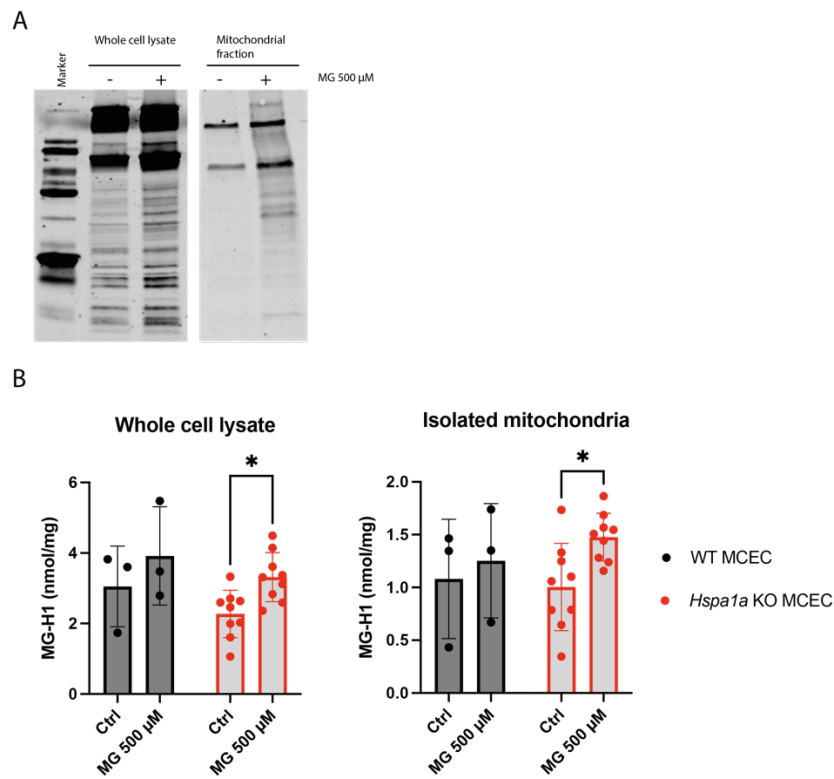
Figure 20 Comparison of MG-H1 levels in whole cell lysate and in isolated mitochondria after acute MG stress.
(A) The blot shows the staining of MG-H1 modified proteins for whole cell protein lysates and isolated mitochondria lysates for the WT MCEC, with and without treatment with 500 µM MG for 24 hours. (B) Whole cell protein lysates and lysates of isolated mitochondria were analyzed via LC-MS/MS by Dr. Thomas Fleming. Data represents mean ± SD, analyzed by a two-way ANOVA statistical test followed by comparing all groups using Sidak`s multiple comparison test. *$p \leq 0.05$.

2.2.6 Changes of the mitochondrial network upon acute MG stress

To analyze changes of the mitochondrial network, we created a fully automated image analysis workflow, together with partners from the ZMBH imaging facility from Heidelberg University, that works as a plugin on the imageJ software platform (A detailed description of the workflow is provided in the methods section, 4.2.18). For this, WT and *Hspa1a* KO MCEC were stressed with MG and immunostaining was performed with an anti-COX1 (Complex 1) antibody. After acute MG stress, the number of mitochondria increased 1.43-fold for WT (p=0.0049) and 1.85-fold for *Hspa1a* KO MCEC (p<0.0001; Figure 21). Accordingly, the total area increased in the WT (1.46-fold, p=0.0302) and in the *Hspa1a* KO MCEC (1.98-fold, p<0.0001). The average size of the mitochondria did not change in all cell lines. The mitochondrial network became more complex in the *Hspa1a* KO MCEC, which is shown by an

increase of the degree of branching, which was 1.85-fold higher (p=0.0060) compared to the respective controls. However, branching was not changed in the WT MCEC (Figure 21).
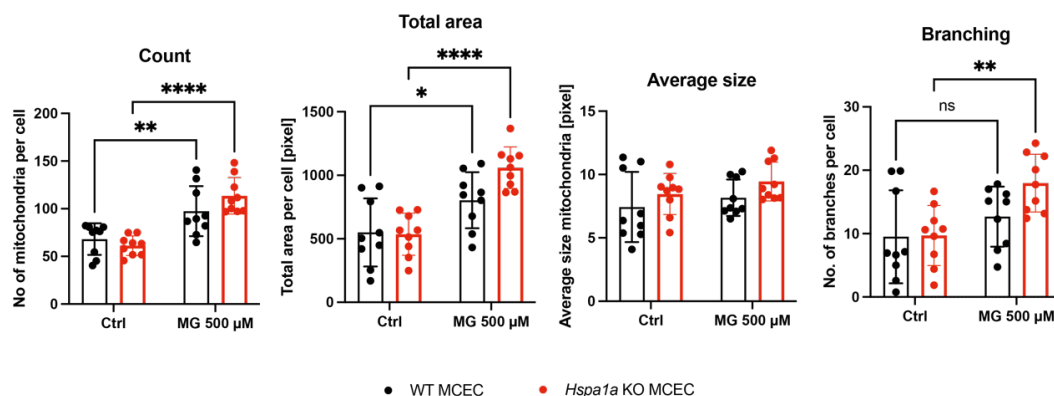
Figure 21 Mitochondria network analysis after acute methylglyoxal stress.
The number, total area, average size, and degree of branching for mitochondria was analyzed from COX1 immunofluorescence images. Data represents mean ± SD, analyzed by a two-way ANOVA statistical test followed by comparing all groups using Sidak`s multiple comparison test. *p ≤ 0.05, **p ≤ 0.01, ****p ≤ 0.0001.

2.2.7 Effect of acute methylglyoxal stress on bioenergetic health

The changes of the mitochondrial network were assumed to be an indicator of an increased energy demand by the cells, which is met by increasing the number of mitochondria through mitochondrial biogenesis. Therefore, in the next experiment it was analyzed whether methylglyoxal stress changes the metabolic capability of the mitochondria, e.g., ATP production. Thus, the cells were stressed with MG for 24 hours and a Seahorse XF cell mitochondrial stress test was performed. During this test, the cells are energetically challenged to assess the basic mitochondrial parameters. These include basal respiration, maximal respiration, spare respiratory capacity, proton leak, non-mitochondrial oxygen consumption and ATP production. During the test, oligomycin, FCCP (carbonyl cyanide-4-(trifluoromethoxy) phenylhydrazone) and rotenone/antimycin A are injected consecutively. Oligomycin, inhibits ATP synthase.[206] FCCP is a potent uncoupler of mitochondrial oxidative phosphorylation and reverses the effect of oligomycin.[207] The injection of rotenone/antimycin A then completely stops mitochondrial respiration.[208] (Figures 22A and 22B). None of the mitochondrial respiration parameters was changed upon treatment in WT and *Hspa1a* KO MCEC (Figure 22C). The baseline values for basal

respiration, maximal respiration, ATP production, proton leak, non-mitochondrial oxygen consumption and spare respiratory capacity were all increased in the untreated *Hspa1a* KO MCEC as compared to untreated WT MCEC, but not statistically significant. By using the measurements for spare respiratory capacity, ATP production, non-mitochondrial oxygen consumption and proton leak, Chacko and colleagues[209] have introduced the concept of a bioenergetic health index to quantify mitochondrial health under stress conditions. From the measurements of the MG stressed cells, the bioenergetic health index showed a worsening of mitochondrial health for the WT and interestingly an increase in mitochondrial health for the *Hspa1a* KO MCEC (Figure 22D). The changes, however, were not statistically significant.
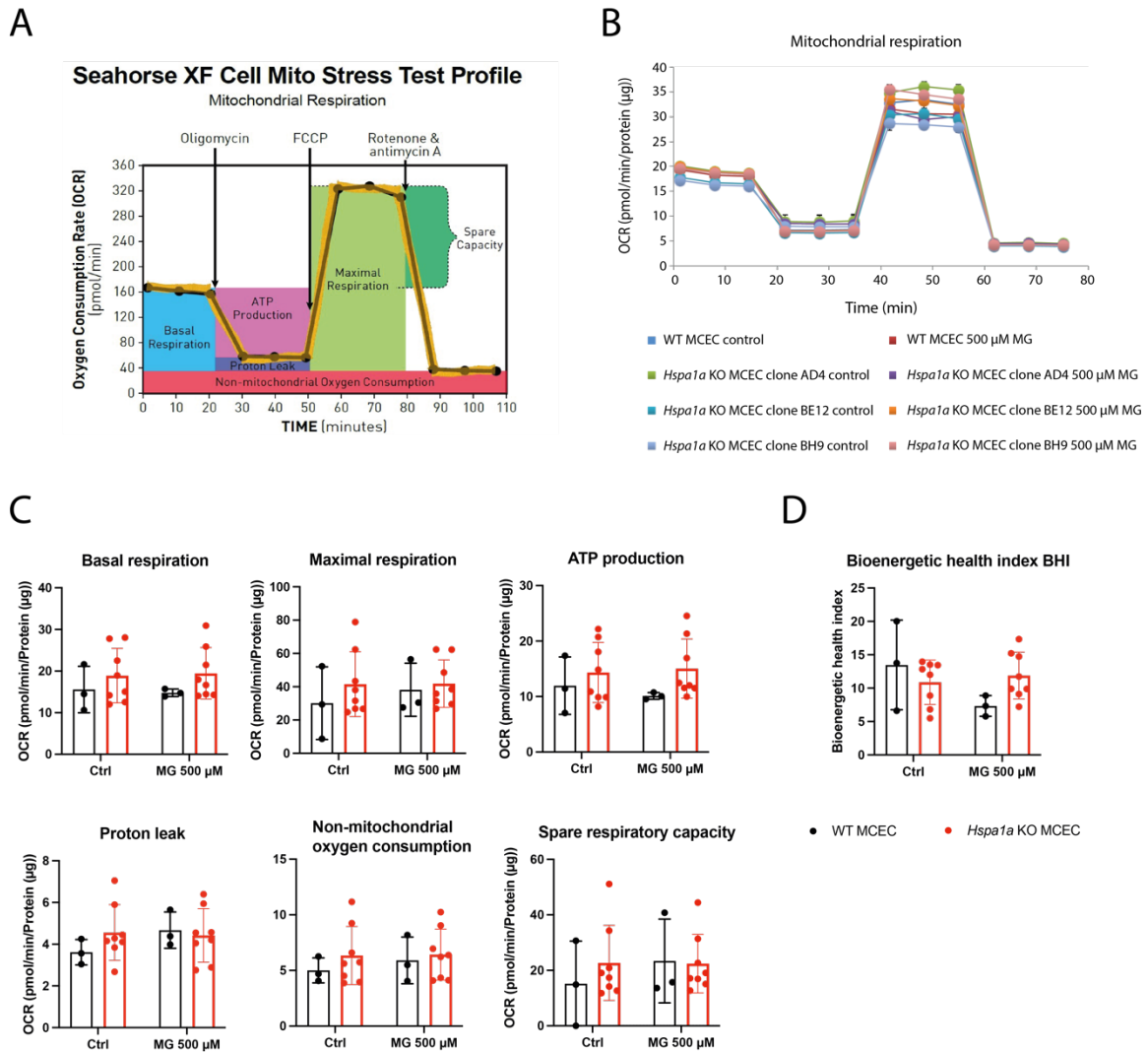
Figure 22 Mitochondrial respiration parameters after a mitochondrial stress test.
(A) The illustration shows the injection moments of oligomycin, FCCP and rotenone/antimycin A and how the different parameters can be obtained from area under curve (AUC) analysis. The figure was adapted from Agilent seahorse wave software. (B) Example result of one biological replicate for a mitochondrial stress test performed under MG stress in WT and *Hspa1a* KO MCEC. (C) The graphs show the changes of the respective parameters, that were measured during mitochondrial respiration after MG stress in WT and three independent *Hspa1a* KO MCEC. (D) The bioenergetic health index (BHI) was calculated based on data for spare respiratory capacity, ATP production, non-mitochondrial oxygen consumption and proton leak. The seahorse XF cell mitochondrial stress test was performed with the help of Dr. Thomas Fleming. Data represents mean ± SD, analyzed by a two-way ANOVA statistical test followed by comparing all groups using Sidak`s multiple comparison test.

2.2.8   mRNA expression changes after chronic methylglyoxal stress

To evaluate the effects of chronic MG stress, WT and *Hspa1a* KO MCEC were treated with 500 µM MG every 24 hours for 7 consecutive days. This should mimic real-live

conditions *in vivo*, where MG is produced continuously as a byproduct during glycolysis. In the WT MCEC the mRNA expression of all heat-shock proteins, that were investigated, were slightly increased after chronic MG stress (Figure 23). However, with exception for *Hspa1a* (1.53-fold, p=0.0046), the increase was not statistically significant. In the *Hspa1a* KO MCEC, the mRNA expression of these heat-shock proteins was also induced, but it was only statistically significant for the three genes, *Hspc1* (1.34-fold, p=0.0034), *Dnajb1* (1.35-fold, p=0.0046) and *Hspe1* (1.56-fold, p=0.011). Compared to the acute MG stress results, where the expression of *Hspb1* was reduced (Figure 16), it was slightly increased after chronic MG stress in WT and in *Hspa1a* KO MCEC (p=ns).
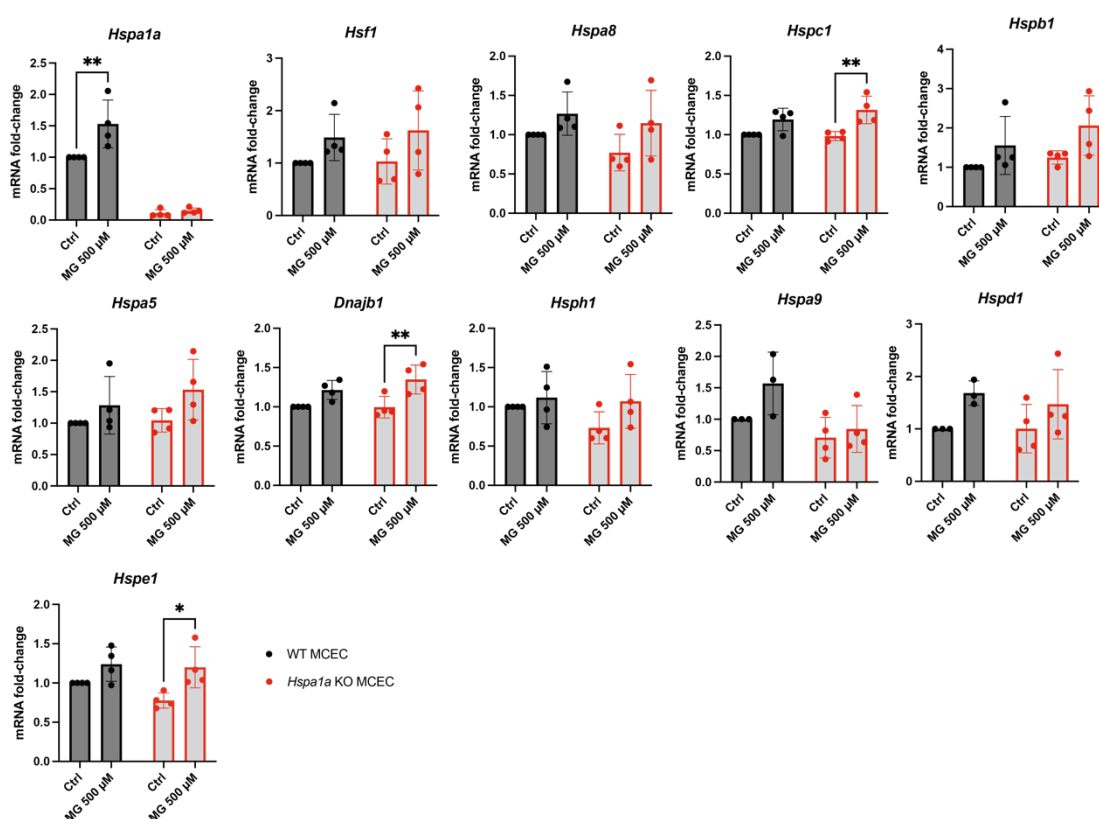
Figure 23 mRNA expression changes of heat-shock proteins after chronic MG stress.
WT and three different *Hspa1a* KO MCEC were treated with 500 µM of methylglyoxal for 7 consecutive days, every 24 hours. The graphs show the fold-change of mRNA expression of heat-shock proteins after chronic MG stress; *Hsp*= Heat-shock protein, *Hsf1*= Heat-shock factor 1, *Dnajb1*= DnaJ homolog subfamily B member 1. Data represents mean $\pm$ SD, analyzed by a two-way ANOVA statistical test followed by comparing all groups using Sidak`s multiple comparison test. *p ≤ 0.05, **p ≤ 0.01.

The mRNA expression of the oxidative stress genes *Nrf2*, *Nqo1* and *Ho1* showed a minor increase, except for WT MCEC *Nrf2* expression, but not statistically significant

(Figure 24A). *Gdf15* expression (Figure 24B) showed lower mRNA levels upon chronic MG stress in the WT MCEC (0.59-fold, p=ns) and in the *Hspa1a* KO MCEC (0.26-fold, p=0.034). While *Vcam1* expression was decreased in acute MG stress, it was induced 2.88-fold (p=0.0039) in the *Hspa1a* KO MCEC after chronic MG stress. *Icam1* expression was not altered in both WT and *Hspa1a* KO MCEC after chronic MG stress.
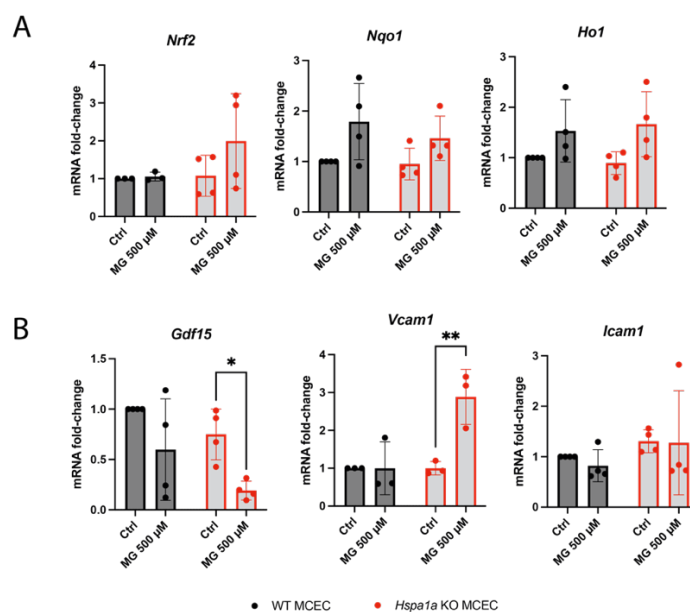
Figure 24 mRNA expression changes of anti-oxidative genes and inflammation markers after chronic MG stress.

WT and three different *Hspa1a* KO MCEC were treated with 500 µM of methylglyoxal for 7 consecutive days, every 24 hours. (A) The graphs show the fold-change of mRNA expression of anti-oxidative genes after chronic MG stress; *Nrf2*= Nuclear factor erythroid 2-related factor 2, *Nqo1*= NAD(P)H dehydrogenase [quinone] 1, *Ho1*= Heme oxygenase 1. (B) The graphs show the fold-change of mRNA expression of genes related to inflammation and atherosclerosis after chronic MG stress; *Gdf15*= Growth differentiation factor 15, *Vcam1*= Vascular cell adhesion molecule 1, *Icam1*= Intercellular adhesion molecule 1. Data represents mean ± SD, analyzed by a two-way ANOVA statistical test followed by comparing all groups using Sidak`s multiple comparison test. *p ≤ 0.05, **p ≤ 0.01.

The mitochondrial fission protein *Drp1* (Figure 25A) showed higher expression levels in the WT MCEC (2.59-fold, p=ns). While *Fis1* showed reduction after acute stress (Figure 18A), after chronic stress the mRNA expression was induced in WT (1.48-fold, p=0.045) and *Hspa1a* KO MCEC (1.73-fold, p=0.012). The mitochondrial fusion proteins *Mfn1* and *Opa1* revealed no statistically significant changes in expression. The baseline expression of *Pink1* in *Hspa1a* KO MCEC was reduced to 0.41-fold (p=0.0062) as compared to the untreated WT MCEC, which was comparable to the

result after acute MG stress (Figure 25B). *Parkin* and *Bnip3* expression showed no statistically significant changes in expression upon chronic MG stress. The key transcription factor, that regulates mitochondrial biogenesis *Pgc1a* was also differently regulated in chronic MG stress compared to acute MG stress. *Pgc1a* mRNA expression was induced 5.25-fold (p=0.001) in the *Hspa1a* KO MCEC (Figure 25C). The changes in expression of the transcription factors *Pgc1b*, *Nrf1* and *Tfam* were not statistically significant. *Tfb2m*, on the other hand, showed a 1.48-fold (p=0.0066) induction in the WT MCEC. *Tomm7* expression was increased by 1.51-fold (p=0.0187) in the *Hspa1a* KO MCEC. The two inner mitochondrial membrane translocases *Timm23* (WT: 1.27-fold, p=0.0004; *Hspa1a* KO: 1.52-fold, p<0.0001) and *Timm17a* (WT: 1.41-fold, p<0.0001; KO: 1.41-fold, p<0.0001) were induced in both WT and *Hspa1a* KO MCEC upon chronic MG stress.
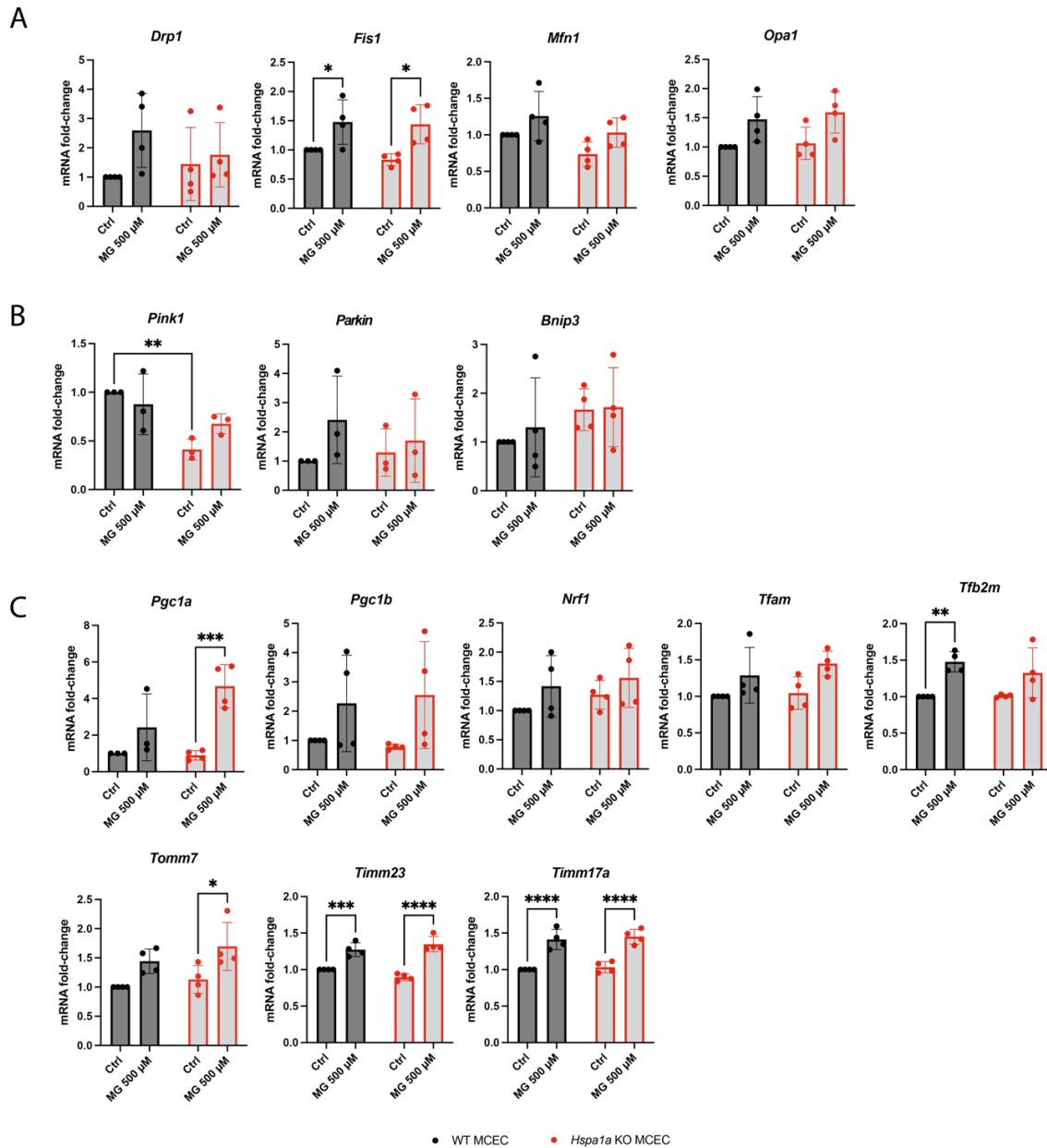
Figure 25 mRNA expression changes of genes related to mitochondrial fission and fusion, mitophagy and mitochondrial biogenesis after chronic MG stress.

WT and three different *Hspa1a* KO MCEC were treated with 500 µM of methylglyoxal for 7 consecutive days, every 24 hours. (A) The graphs show the fold-change of mRNA expression of the mitochondrial fusion and fission machinery after chronic MG stress; *Drp1*= dynamin-related protein 1, *Fis1*= mitochondrial fission protein 1, *Mfn*= mitofusin, *Opa1*= optic atrophy protein 1. (B) The graphs show the fold-change of mRNA expression of mitophagy-related genes after chronic MG stress; *Pink1*= PTEN-induced putative kinase protein 1, *Parkin*= Parkinson juvenile disease protein, *Bnip3*= BCL2/adenovirus E1B 19 kDa protein-interacting protein 3. (C) The graphs show the fold-change of mRNA expression of genes that regulate mitochondrial biogenesis after chronic MG stress; *Pgc*= peroxisome proliferator-activated receptor gamma coactivator 1, *Nrf1*= nuclear respiratory factor 1, *Tfam*= mitochondrial transcription factor 1, *Tfb2m*= transcription factor B2, mitochondrial,

42

Tomm7= translocase of the outer mitochondrial membrane 7, *Timm*= translocase of the inner mitochondrial membrane. Data represents mean ± SD, analyzed by a two-way ANOVA statistical test followed by comparing all groups using Sidak`s multiple comparison test. *$p \leq 0.05$, **$p \leq 0.01$, ***$p \leq 0.001$, ****$p \leq 0.0001$.

2.2.9 Mitochondrial network changes after chronic MG stress

As with the gene expression analysis, the mitochondrial network analysis was also performed in WT and *Hspa1a* KO MCEC after chronic methylglyoxal stress. The number of mitochondria did not change in WT MCEC upon chronic MG stress (Figure 26). However, the number did decrease to 0.66-fold (p=0.0019) in *Hspa1a* KO MCEC as compared to their controls and 0.72-fold (p=0.0265). The total area of mitochondria drastically dropped in WT MCEC (0.23-fold, p<0.0001) and to a lesser extent in *Hspa1a* KO MCEC (0.61-fold, p<0.0001). The average size of mitochondria in the *Hspa1a* KO MCEC remained constant, whereas in the WT MCEC it was reduced 0.22-fold (p<0.0001). The branching after chronic MG stress was also reduced in both cell lines. In WT MCEC it was reduced to 0.23-fold (p<0.0001) and in *Hspa1a* KO MCEC it was reduced to 0.55-fold (p<0.0001).
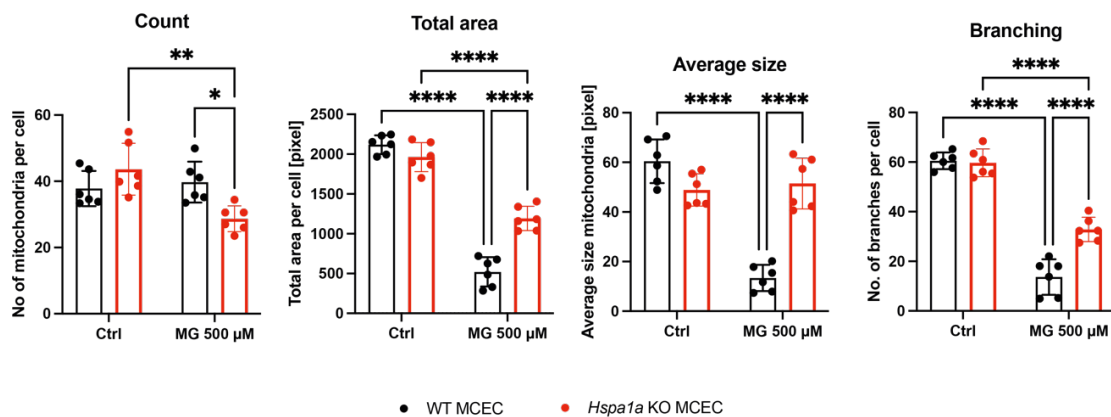
Figure 26 Mitochondria network analysis after chronic methylglyoxal stress.
The number, total area, average size, and degree of branching for mitochondria was analyzed from COX1 immunofluorescence images. Data represents mean ± SD, analyzed by a two-way ANOVA statistical test followed by comparing all groups using Sidak`s multiple comparison test. *$p \leq 0.05$, **$p \leq 0.01$, ***$p \leq 0.001$, ****$p \leq 0.0001$.

2.2.10 Effect of chronic methylglyoxal stress on bioenergetic health

The bioenergetic health index was also analyzed in the WT and *Hspa1a* KO MCEC after chronic MG stress. The single parameters that were obtained from the

mitochondrial stress test showed only minor differences in the treated, compared to the control cells (Figure 27A). However, the ATP production differed between the cell lines. While in the WT MCEC ATP production was unchanged, in the *Hspa1a* KO MCEC ATP production was increased 1.20-fold (p=0.01). Non-mitochondrial oxygen consumption was only increased in the *Hspa1a* KO MCEC after chronic stress (1.25-fold, p=0.0007). The bioenergetic health index was unchanged for both, WT MCEC and *Hspa1a* KO MCEC (Figure 27B).
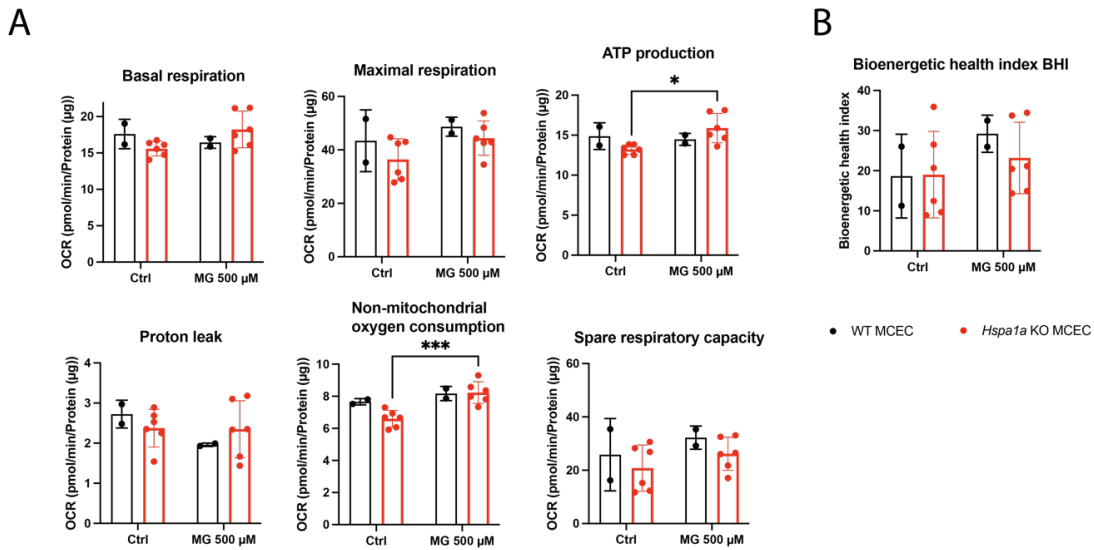
Figure 27 Mitochondrial respiration parameters after a mitochondrial stress test following chronic methylglyoxal stress.

(A) The graphs show the changes of the respective parameters, that were measured during mitochondrial respiration after chronic MG stress in WT and *Hspa1a* KO MCEC. (B) The bioenergetic health index (BHI) was calculated based on data for spare respiratory capacity, ATP production, non-mitochondrial oxygen consumption and proton leak. The Seahorse XF cell mitochondrial stress test was performed with the help of Dr. Thomas Fleming. Data represents mean $\pm$ SD, analyzed by a two-way ANOVA statistical test followed by comparing all groups using Sidak`s multiple comparison test. *p $\leq$ 0.05, ***p $\leq$ 0.001.

2.3 Diabetic nephropathy in a *Hspa1a/Hspa1b* knockout mouse model

In the first part of this study the focus was on the potential effects of acute and chronic methylglyoxal stress in endothelial cells. In the second part, the aim was to analyze control and STZ-induced diabetic wild-type and *Hspa1a*/*Hspa1b* knockout mice regarding the severity of a potential diabetic nephropathy phenotype.

2.3.1 Validation of *Hspa1a*/*Hspa1b* knockout mice

The mouse cardiac endothelial cell (MCEC) line only contained the *Hspa1a* gene, but not the *Hspa1b* gene. Therefore, it was analyzed, if the wild-type littermates that were used as controls contain both genes. Again, the genomic sequence of the two genes were amplified by PCR with an additional 500 base pair overhang on either site.

The PCR amplification however, revealed an 800 bp product for the *Hspa1b* gene, suggesting that the gene was not present (Figure 28A). On the other hand, the *Hspa1a* gene PCR resulted in the expected 3.8 kb product. The validation of a successful gene knockout in the *Hspa1a* KO mice was performed with mRNA and protein analyses (western blot and immunohistochemistry). Figure 28B shows the greatly reduced expression of *Hspa1a* (0.014-fold, $p<0.0001$), detected *via* qRT-PCR in WT and *Hspa1a* KO mice. Figure 28C shows the expression of HSPA1A, detected *via* western blot of WT and *Hspa1a* KO mice. The weak signal that was still detected for HSPA1A in the KO animals was assumed to be unspecific binding of the polyclonal anti-HSPA1A antibody to HSPA1L, as it was confirmed before in the endothelial *Hspa1a* KO cell line (Figure 13C). Furthermore, the protein expression from immunohistochemistry staining of kidney sections was negative for HSPA1A in the knockout animals (Figure 28D).
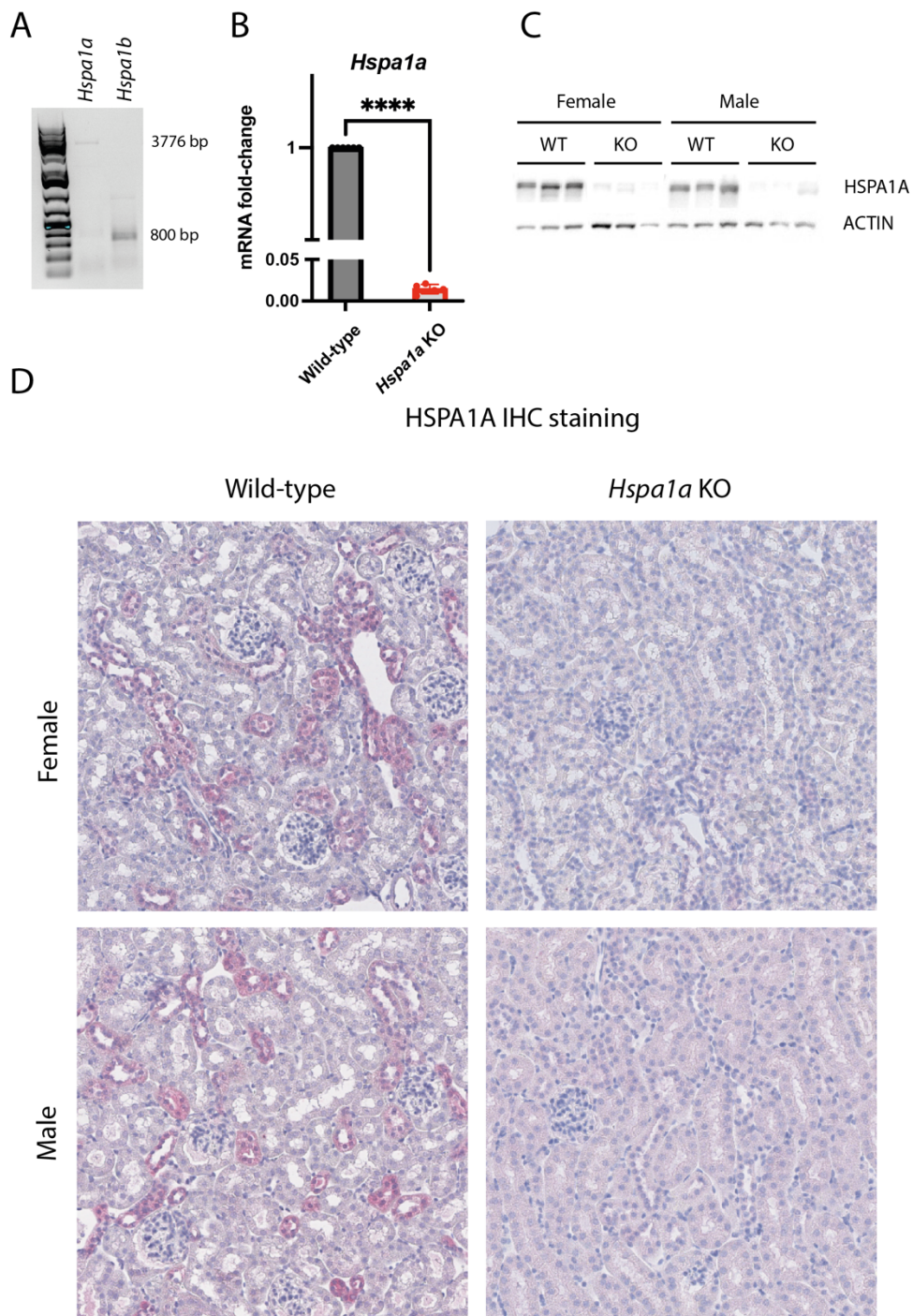
Figure 28 Validation of the *Hspa1a*/*Hspa1b* gene knockout in female and male mice.

(A) PCR amplification of the loci surrounding the *Hspa1a* and the *Hspa1b* gene in wild-type mice. (B) *Hspa1a* expression in WT and *Hspa1a* KO mice. (C) Western blot analysis of HSPA1A expression in mouse kidneys from WT and *Hspa1a* KO female and male mice. (D) Immunohistochemistry analysis of HSPA1A expression in mouse kidneys from WT and *Hspa1a* KO female and male mice. The IHC staining was performed in the Center for Model System and Comparative Pathology (CMCP) of Heidelberg University Hospital. Data represents mean $\pm$ SD, analyzed by an unpaired t test with Welch's correction. ****p < 0.0001

2.3.2 Streptozotocin-induced diabetes in WT and *Hspa1a* KO mice

At the age of 10 weeks, female and male mice were injected daily with streptozotocin for one week. The blood glucose levels were monitored regularly, and diabetic animals were injected with insulin. At the age of 28 weeks, mice were sacrificed, and urine, blood and organs were harvested for further analysis. The blood glucose levels of healthy animals were in the range of 120-150 mg/dL during the time course of the experiment. In the diabetic animals, the blood glucose levels started to rise from week 12 to a maximum of 540 mg/dL in week 24 (Figure 29).
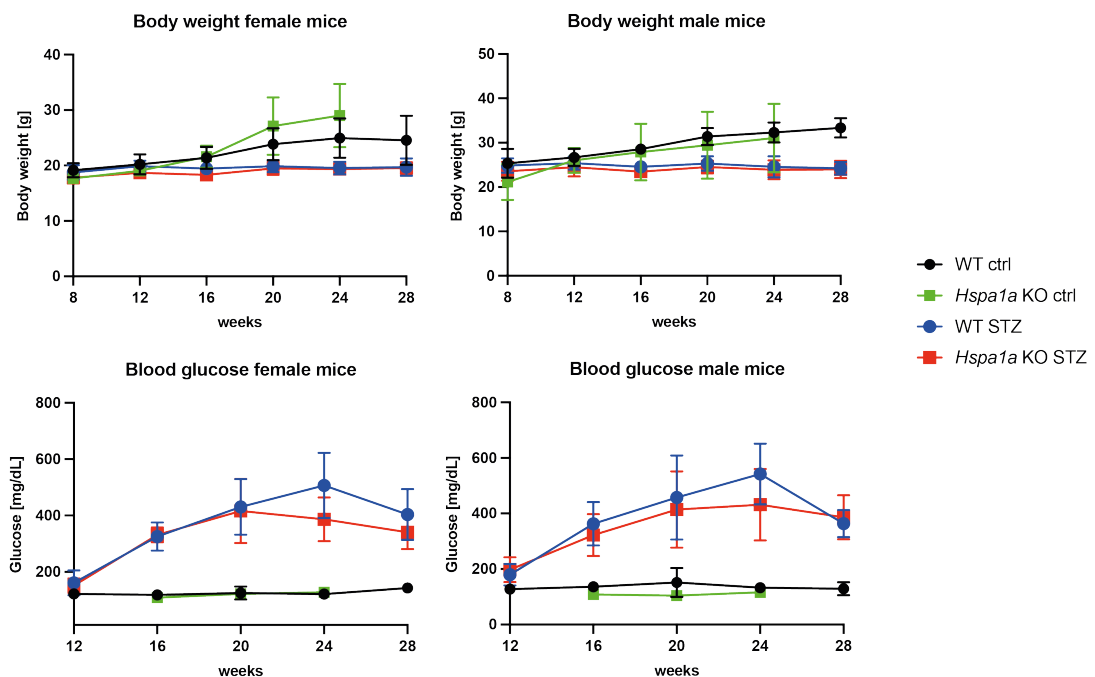
Figure 29 Bodyweight and blood glucose monitoring in control and STZ-treated WT and *Hspa1a* KO mice.
STZ injections, weight control and blood glucose measurements were done by Axel Erhardt. No data was available for 28-week-old *Hspa1a* KO ctrl mice.

2.3.3 Albuminuria

Albuminuria is one of the hallmarks of diabetic nephropathy. It is the most important detection parameter for the severity of glomerulus injury and thereby kidney health. To normalize the albumin levels from the different animals, creatinine levels were also measured. The UACR in WT and *Hspa1a* healthy control mice was 10.04 mg/g and 10.57 mg/g, respectively (Figure 30). Diabetic WT mice had a more than 4-fold increased UACR of 41.59 mg/g (p=0.0002) as compared to their controls. Diabetic

Hspa1a KO mice only showed a 3-fold increase in their UACR (33.40 mg/g, p=ns) as compared to their controls. There was no gender-specific difference detected (Figure 46 in appendix) between the groups.
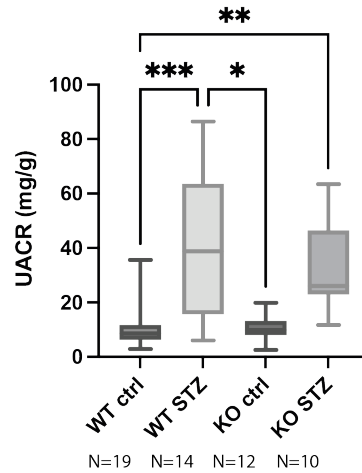
Figure 30 Urinary albumin-to-creatinine ratio (UCAR).
Excreted albumin and creatinine were measured from urine of WT and *Hspa1a* KO control and diabetic animals. Albumin measurements from mouse urine were done by Dr. Claus Rodemer. Creatinine measurements from mouse urine were done in the lab of Prof. Dr. Jürgen Okun in the metabolic center (division of inborn errors of metabolism) of Heidelberg University Hospital. Data represents mean ± SD, analyzed by a two-way ANOVA statistical test followed by comparing all groups using Sidak`s multiple comparison test. *p ≤ 0.05, **p ≤ 0.01, ***p ≤ 0.001.

2.3.4   Glomerulus pathology

2.3.4.1   Fractional mesangial area

Albuminuria is one consequence of glomerulosclerosis. Both diabetic groups (WT and *Hspa1a* KO) showed an increased albumin excretion. Thus, acid fuchsin orange G (AFOG) stained kidney tissue slides were analyzed regarding signs of glomerular damage. The fractional mesangial area (FMA) in diabetic WT animals was increased compared to their controls (23.02% vs. 30.19%, p=0.0009; Figure 31). The FMA in diabetic *Hspa1a* KO animals was also increased as compared to their controls (25.85% vs. 37.20%, p<0.0001). Furthermore, the increase of FMA was aggravated in diabetic *Hspa1a* KO animals as compared to diabetic WT animals (30.19% vs. 37.20%, p=0.0019). No differences were observed between male and female mice (Figure 47 in appendix).
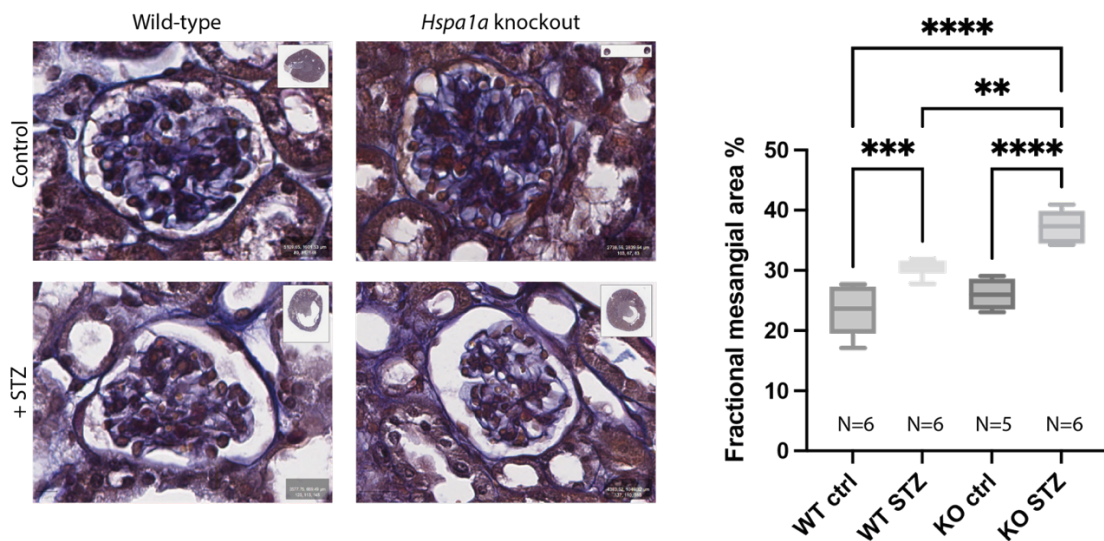
Figure 31 Analysis of the fractional mesangial area.

Tissue slices of kidneys from WT and *Hspa1a* KO control and diabetic mice were stained with acid fuchsin orange G (AFOG). The area of the glomerular tuft and the Bowman's capsule was measured, and the fractional mesangial area was calculated as shown in methods section 4.2.29. The AFOG staining of the kidney sections was performed in the CMCP. Data represents mean ± SD, analyzed by a two-way ANOVA statistical test followed by comparing all groups using Sidak`s multiple comparison test. **p ≤ 0.01, ***p ≤ 0.001, ****p ≤ 0.0001.

2.3.4.2 Glomerular basement membrane

The thickening of the glomerular basement membrane (GBM) is widely recognized as one pathological outcome in diabetic nephropathy. A thickening and scarring of this filtration barrier can increase protein leakage and lead to a worsening of albuminuria. Kidney sections of control and diabetic WT and *Hspa1a* KO mice were imaged with an electron microscope and the thickness of the glomerular basement membrane measured. It was observed that diabetic mice of both groups showed no statistically significant difference in GBM thickness compared to their controls (WT: 174.7 nm vs. 181.7 nm, p=ns; *Hspa1a* KO: 145.3 nm vs. 166.1 nm, p=ns; Figure 32). However, the GBM of diabetic control mice was thinner as compared to WT control mice (174.7 nm vs. 145.4 nm, p=0.004). There were no differences between female and male mice were observed (Figure 48 in appendix).
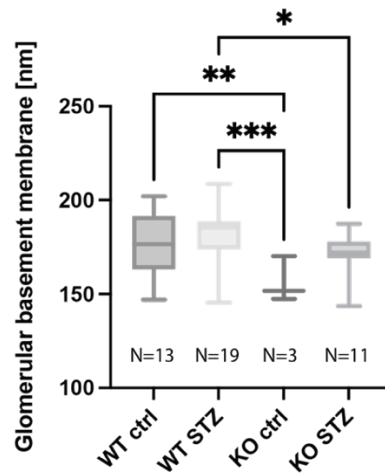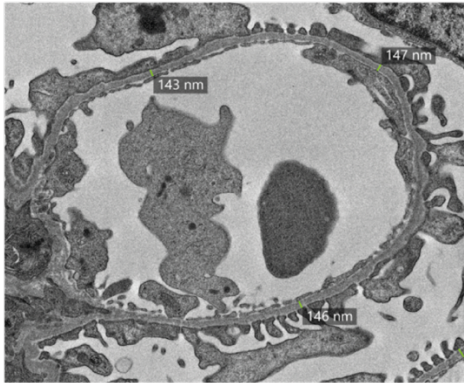
Figure 32 Analysis of the thickness of the glomerular basement membrane.
Tissue slices of kidneys from WT and *Hspa1a* KO control and diabetic mice were examined with an electron microscope. Preparation and electron microscopy was performed in the EM Lab (Dr. Ingrid Haußer-Siller, Institute of Pathology of Heidelberg University Hospital). Data represents mean ± SD, analyzed by a two-way ANOVA statistical test followed by comparing all groups using Sidak`s multiple comparison test. *p ≤ 0.05, **p ≤ 0.01, ***p ≤ 0.001.

2.3.4.3 Podocyte analysis

Podocytes were labeled with anti-WT1 antibody in kidney tissue and the number of podocytes was analyzed for all groups. No changes in the number of podocytes were detected between the groups (Figure 33). The analysis for female and male mice as well showed no differences (Figure 49 in appendix).
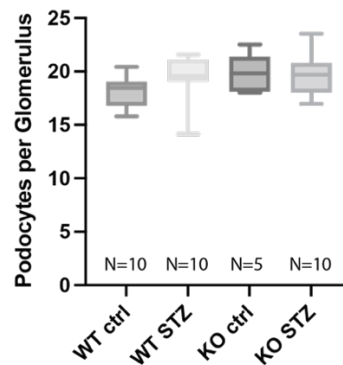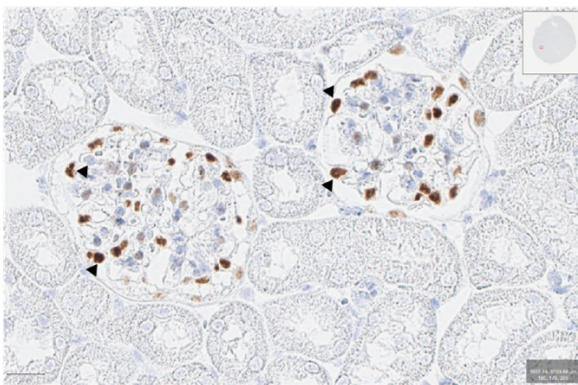
Figure 33 Podocyte analysis from kidney sections.
Podocytes (arrow heads in the left panel) from WT and *Hspa1a* KO control and diabetic mice were labeled *via* immunohistochemistry using an anti-WT1 antibody in kidney tissue. The number of podocytes was counted for all four groups. IHC was performed in the CMCP. Data represents mean ± SD, analyzed by a two-way ANOVA statistical test followed by comparing all groups using Sidak`s multiple comparison test.

2.3.5 Electrolyte excretion

In addition to albumin, the urine was analyzed for sodium, chloride, potassium, and phosphate excretion. These electrolytes are usually reabsorbed in the healthy proximal tubule. An increase in their excretion can be a sign for tubular damage. The excretion of the four electrolytes was, as before, normalized to urinary creatinine content. Sodium excretion in diabetic WT and *Hspa1a* KO mice was unchanged as compared to their controls (WT: 199 mmol/g vs. 247.7 mmol/g, p=ns; *Hspa1a* KO: 135.1 mmol/g vs. 281.9 mmol/g, p=ns; Figure 34). Chloride excretion also showed no differences in diabetic WT mice (324.5 mmol/g vs. 286.9 mmol/g, p=ns) and diabetic *Hspa1a* KO mice (272.0 mmol/g vs. 369 mmol/g, p=ns) as compared to their respective controls. Potassium excretion was increased in diabetic WT mice (305.5 mmol/g vs. 465.4 mmol/g, p=0.01) but unchanged in diabetic *Hspa1a* KO mice (406.7 mmol/g vs. 507.8 mmol/g, p=ns). Phosphate excretion was increased in both diabetic WT and diabetic *Hspa1a* KO mice as compared to their controls (WT: 108.7 mmol/g vs. 243.2 mmol/g, p=0.0005; *Hspa1a* KO: 134.4 mmol/g vs. 274.1 mmol/g, p=0.017). Gender-specific analysis was also performed but showed no differences (Figures 50-53 in appendix).
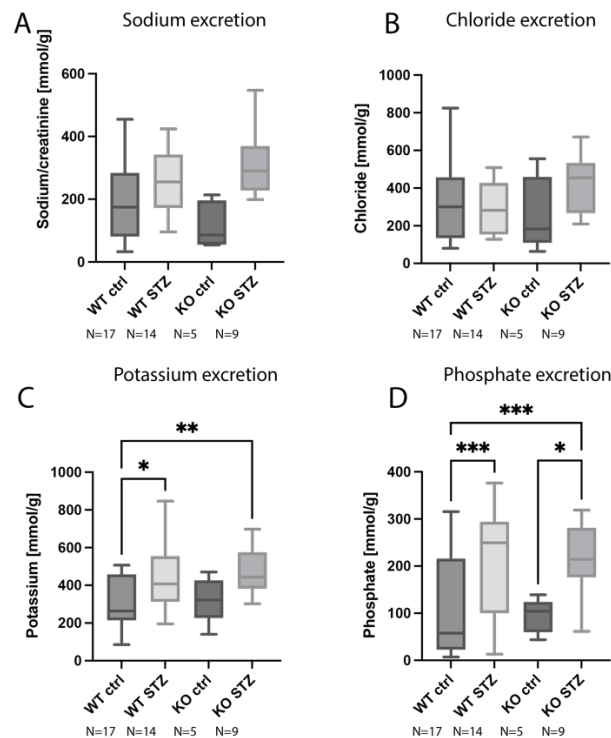
Figure 34 Urinary electrolyte excretion.

Excreted electrolytes (A) sodium, (B) chloride, (C) potassium and (D) phosphate and creatinine were measured from urine of WT and *Hspa1a* KO control and diabetic animals. Electrolyte measurements from mouse urine was performed with the help of Dr. Maik Brune from the central lab of Heidelberg University Hospital. Data represents mean $\pm$ SD, analyzed by a two-way ANOVA statistical test followed by comparing all groups using Sidak`s multiple comparison test. *$p \le 0.05$, **$p \le 0.01$, ***$p \le 0.001$.

2.3.6 mRNA expression analysis in the kidneys of wild-type and *Hspa1a* knockout control and diabetic mice

The mRNA expression levels in the kidneys of control and diabetic WT and *Hspa1a* KO mice were analyzed. *Hspa1a* expression was increased in the diabetic WT mice as compared to their controls (1.45-fold, p=0.0165, Figure 35). Interestingly, the expression was differently regulated in female and male mice (Figure 54 in appendix). While in female diabetic WT mice, *Hspa1a* expression remained unchanged, in male diabetic WT mice, it was increased 1.96-fold (p<0.0001). *Hspa8* expression was decreased in both, WT (0.36-fold, p<0.0001) and *Hspa1a* KO (0.52-fold, p=0.0001) diabetic mice. Additionally, the expression in *Hspa1a* control mice, was decreased to 0.65-fold (p=0.0001) as compared to WT control mice. *Hspb1* expression was unchanged in diabetic WT mice, but 3.98-fold (p=0.0012) increased in diabetic

Hspa1a KO mice. The expression of *Dnajb1* was only decreased in diabetic WT mice (0.66-fold, p=0.019), whereas for *Hsph1* the expression decreased in all diabetic mice (WT: 0.27-fold, p<0.0001; *Hspa1a* KO: 0.60-fold, p=0.026). In diabetic WT and *Hspa1a* KO mice, *Hspa9* expression was reduced to 0.70-fold (p=0.0039) and to 0.48-fold (p<0.0001), respectively. The expression of *Hspa9* was 1.37-fold (p=0.0037) higher in *Hspa1a* KO control mice, than in WT control mice. *Hspd1* mRNA expression in the kidneys decreased to 0.42-fold (p=0.0004) in diabetic WT animals. Furthermore, the expression of *Hspd1* was reduced to 0.23-fold (p<0.0001) in the control *Hspa1a* KO mice compared to WT control mice.
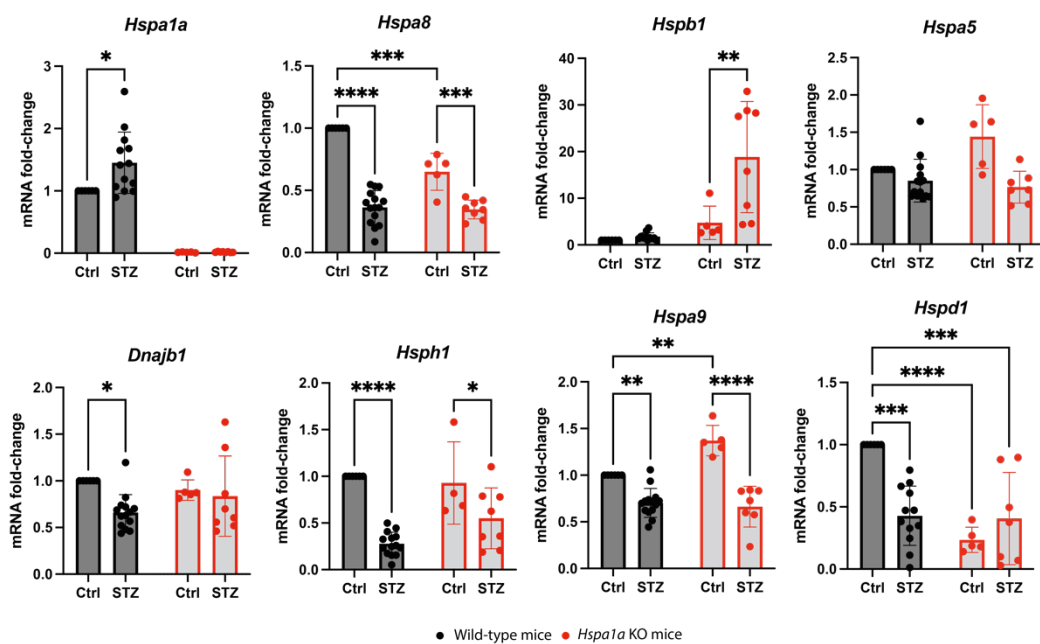
Figure 35 mRNA expression levels of heat-shock proteins in mouse kidneys from WT and *Hspa1a* KO control and diabetic mice.
Data represents mean ± SD, analyzed by a two-way ANOVA statistical test followed by comparing all groups using Sidak`s multiple comparison test. *p ≤ 0.05, **p ≤ 0.01, ***p ≤ 0.001, ****p ≤ 0.0001.

The expression of the antioxidant response genes *Nrf2* and *Ho1* (Figure 36A) were not differentially regulated in the diabetic mice, as compared to their respective controls. *Nqo1*, however, was 1.66-fold (p=0.012) increased in diabetic WT mice and 1.69-fold (p=ns) in diabetic *Hspa1a* KO mice. The mRNA expression of the inflammation and atherosclerosis markers *Gdf15*, *Vcam1* and *Icam1* (Figure 36B) were all increased in the diabetic WT mice (*Gdf15*: 6.72-fold, p=0.0009; *Vcam1*: 3.40-fold, p=0.0004; *Icam1*: 1.49-fold, p=0.035), but not in *Hspa1a* KO mice.
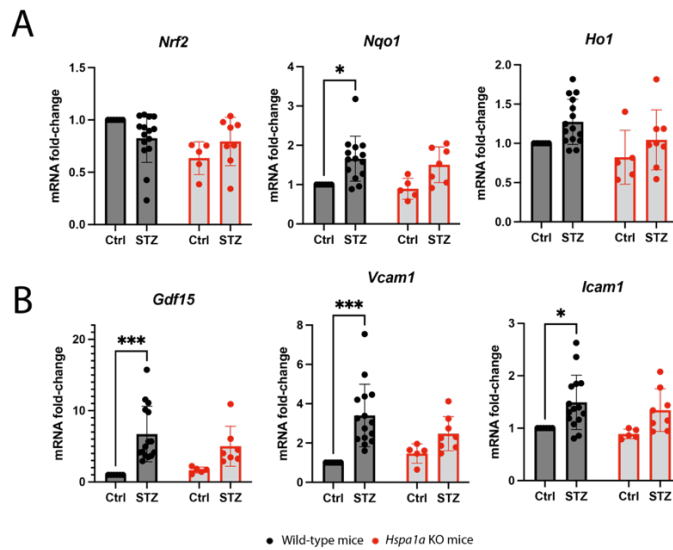
Figure 36 mRNA expression levels of (A) antioxidative genes and (B) inflammation markers in mouse kidneys from WT and *Hspa1a* KO control and diabetic mice.
Data represents mean ± SD, analyzed by a two-way ANOVA statistical test followed by comparing all groups using Sidak`s multiple comparison test. *$p \leq 0.05$, ***$p \leq 0.001$.

The mRNA expression of mitochondrial fission proteins *Drp1* and *Fis1* (Figure 37A) was decreased, but only in diabetic WT mice (*Drp1*: 0.46-fold, $p<0.0001$; *Fis1*: 0.47-fold, $p<0.0001$). Furthermore, the baseline expression of *Drp1* and *Fis1* was decreased in *Hspa1a* KO mice, as compared to WT control mice (*Drp1*: 0.29-fold, $p<0.0001$; *Fis1*: 0.61-fold, $p=0.0035$). Mitochondrial fusion proteins were downregulated in the diabetic animals. In diabetic WT and *Hspa1a* KO mice, *Mfn1* expression was reduced to 0.54-fold ($p=0.0013$) and to 0.50-fold ($p<0.0001$), respectively. The expression of *Mfn1* was 1.66-fold ($p<0.0001$) higher in *Hspa1a* control mice, than in WT control mice. *Opa1* mRNA expression was only reduced in diabetic WT animals (0.54-fold, $p=0.035$), as compared to their controls. The expression of the mitophagy-regulating protein *Pink1* (Figure 37B) was decreased in the diabetic animals compared to their respective controls (WT: 0.54-fold, $p=ns$; *Hspa1a* KO: 0.26-fold, $p<0.0001$). Additionally, the expression of *Pink1* was 2.97-fold ($p<0.0001$) increased in non-diabetic *Hspa1a* KO mice, as compared to non-diabetic WT mice. The mRNA expression of other mitophagy-related proteins *Parkin* and *Bnip3* was unchanged in diabetic mice. The transcription factors, regulating mitochondrial biogenesis *Pgc1a*, *Pgc1b* and *Tfam* all showed a reduced mRNA expression in diabetic mice, as compared to their controls (Figure 37C). In diabetic

54

WT mice, *Pgc1a* expression was reduced to 0.66-fold (p=0.0047), whilst *Pgc1b* expression was reduced to 0.56-fold (p=0.0022), and *Tfam* expression was reduced to 0.64-fold (p=0.0064). In diabetic *Hspa1a* KO mice, *Pgc1a* expression was reduced to 0.61-fold (p=0.0026) and *Pgc1b* expression was reduced to 0.34-fold (p=0.0009). The expression of the mitochondrial protein transporter *Timm23* was not changed in all diabetic mice.
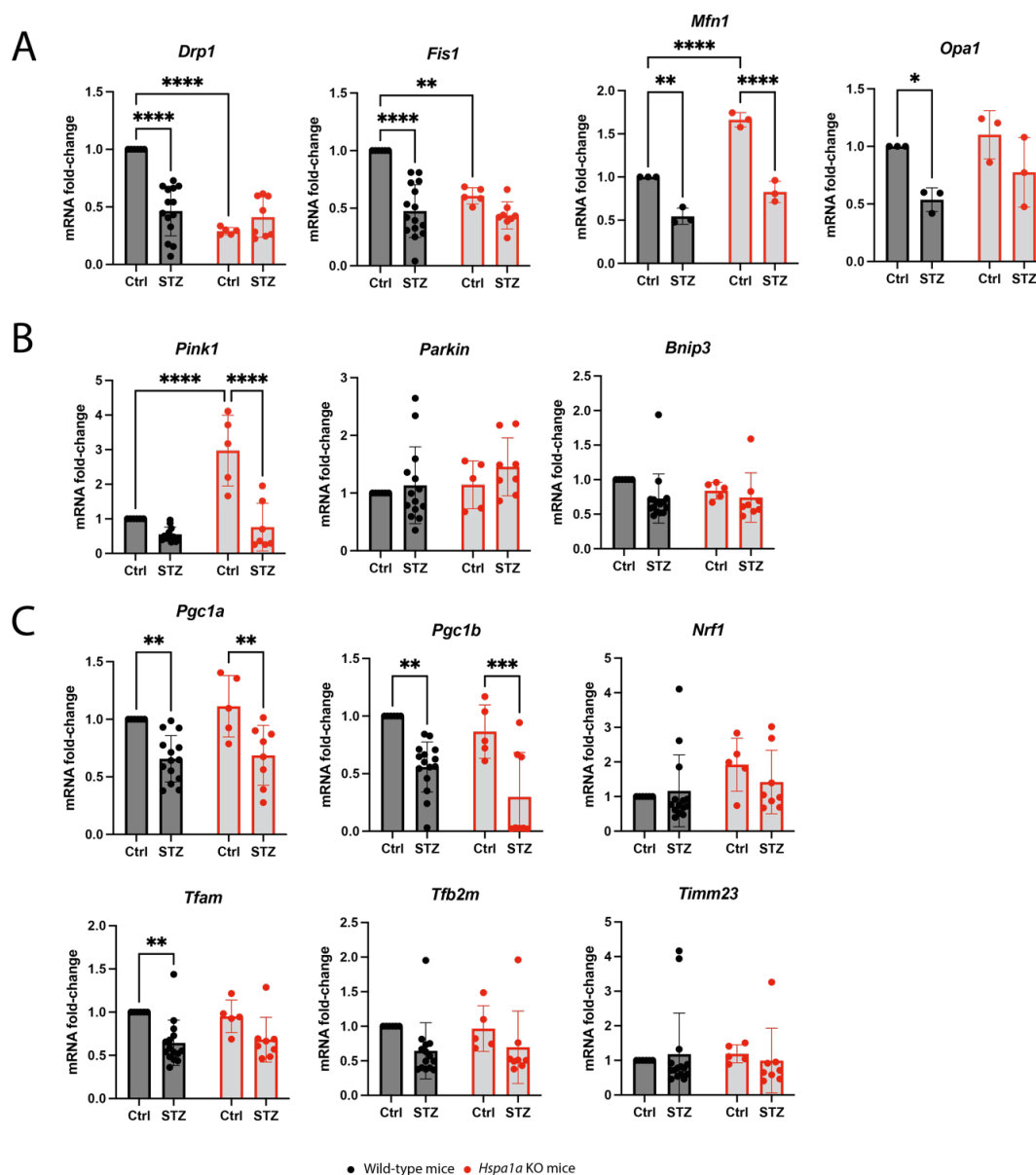
Figure 37 mRNA expression levels of genes related to (A) mitochondrial fission and fusion, (B) mitophagy and (C) mitochondrial biogenesis in mouse kidneys from WT and *Hspa1a* KO control and diabetic mice.

Data represents mean ± SD, analyzed by a two-way ANOVA statistical test followed by comparing all groups using Sidak`s multiple comparison test. *p ≤ 0.05, **p ≤ 0.01, ***p ≤ 0.001, ****p ≤ 0.0001.

2.3.7 Protein expression analysis in kidney tissue

Kidney sections of wild-type control and diabetic mice were stained with an anti-HSPA1A antibody for the detection of differences in HSPA1A protein expression of the two groups. The expression of HSPA1A did not differ in diabetic mice, as compared to their controls (Figure 38). Furthermore, the expression detected of HSPA1A in the IHC analysis was slightly higher in male diabetic mice, as compared to female mice (Figure 55 in appendix), which was also observed for the *Hspa1a* mRNA expression analysis (Figure 54 in appendix).
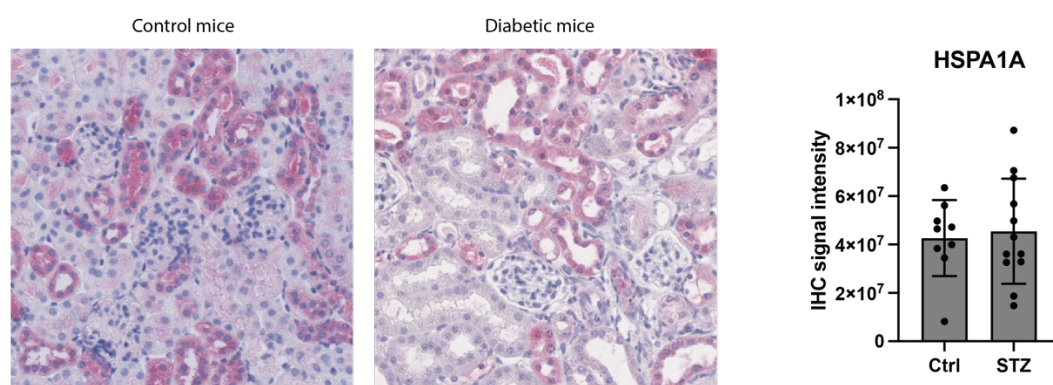
Figure 38 Immunohistochemistry analysis of HSPA1A protein expression from kidney sections. The images show the HSPA1A protein expression in wild-type control and STZ-induced diabetic mice. IHC staining was performed in the CMCP. Data represents mean ± SD.

Following the immunohistochemistry analysis, protein expression analysis was performed with whole kidney protein lysates of all four groups (Figures 39 and 57 in appendix). HSPA1A protein expression in all diabetic WT mice was no different, as compared to their controls. In male mice, the expression was unchanged, whereas in female mice, the expression was reduced to 0.71-fold (p=0.0005, Figure 56 in appendix). The expression of HSPB1 was only reduced in diabetic *Hspa1a* KO mice (0.63-fold, p=0.0177). Furthermore, the expression of HSPB1 was 2.69-fold (p=0.0001) increased in control *Hspa1a* KO mice, as compared to control WT mice. Protein expression of HSPA9 was 1.52-fold (p=ns) increased in diabetic WT animals, whereas it was decreased to 0.54-fold (p=0.0085) in diabetic *Hspa1a* KO animals, as compared to their respective controls. HSPA9 expression was also increased in control *Hspa1a* KO mice, as compared to WT control mice (2.93-fold, p<0.0001). Protein expression of HSPD1 was reduced to 0.61-fold (p=ns) in diabetic WT animals, whereas it was 5.15-fold (p=0.0038) increased in diabetic *Hspa1a* KO animals, as

compared to their respective controls. Furthermore, HSPD1 expression was largely decreased in control *Hspa1a* KO mice, as compared to WT control mice (0.19-fold, p=0.0053).
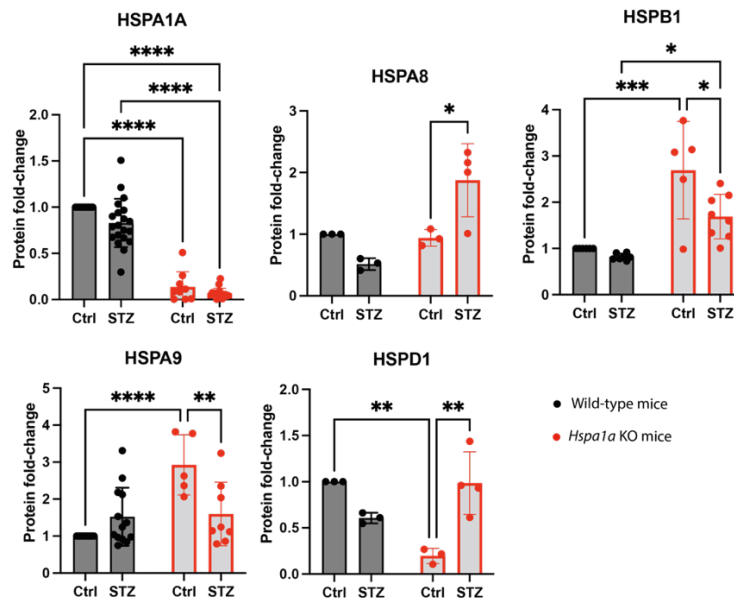
Figure 39 Protein expression of heat-shock proteins from western blot analysis of whole kidney protein lysates from WT and *Hspa1a* KO control and diabetic mice.

Data represents mean ± SD, analyzed by a two-way ANOVA statistical test followed by comparing all groups using Sidak`s multiple comparison test. *p ≤ 0.05, **p ≤ 0.01, ***p ≤ 0.001, ****p ≤ 0.0001.

The expression of the mitochondrial fission protein DRP1 was reduced to 0.71-fold (p=0.016) in diabetic WT mice, and unchanged in diabetic *Hspa1a* KO mice, as compared to their controls (Figure 40A). Also, the expression of DRP1 in *Hspa1a* KO control mice, was reduced as compared to WT control mice (0.71-fold, p=0.015). The expression of mitochondrial fusion protein MFN1 was reduced in both, diabetic WT and *Hspa1a* KO mice, as compared to their controls (WT: 0.74-fold, p=0.03; *Hspa1a* KO: 0.75-fold, p=0.03). The expression of the mitophagy protein PARKIN was also reduced in both, diabetic WT and *Hspa1a* KO mice, as compared to their controls (WT: 0.67-fold, p=0.0005; *Hspa1a* KO: 0.76-fold, p=0.0001). GDF15 protein expression (Figure 40B) was reduced in diabetic WT and *Hspa1a* KO mice, as compared to their controls (WT: 0.64-fold, p=0.0001; *Hspa1a* KO: 0.63-fold, p<0.0001). The expression of VCAM1 was 1.43-fold (p=ns) increased in diabetic WT animals, and to 0.66-fold (p=0.023) decreased in diabetic *Hspa1a* KO animals, as compared to their respective controls. Baseline VCAM1 expression in control mice

was increased in *Hspa1a* KO mice, as compared to their WT controls (2.08-fold, p=0.0007). The expression of the oxidative stress related protein HO1 showed no statistically significant expression changes on the protein level.
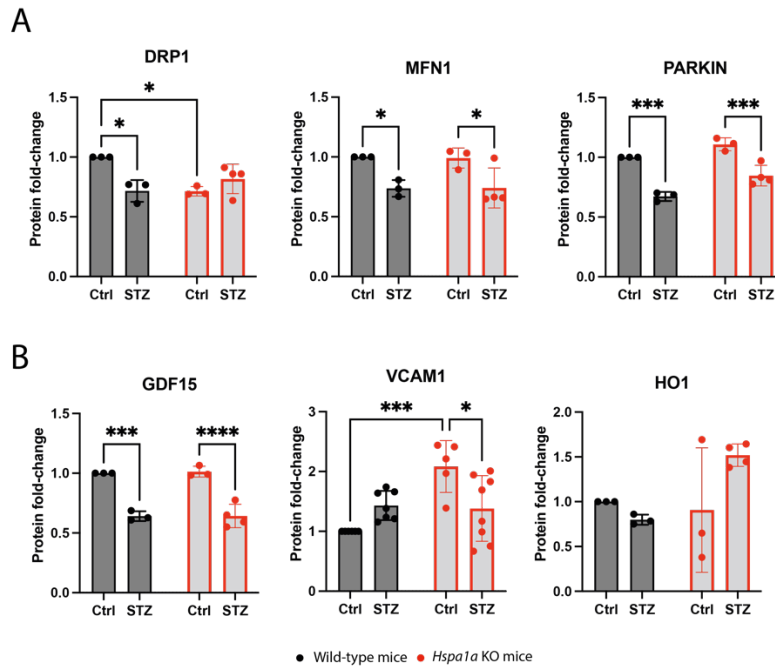
Figure 40 Protein expression of mitochondrial proteins and stress-related proteins from western blot analysis of whole kidney protein lysates from WT and *Hspa1a* KO control and diabetic mice. Data represents mean ± SD, analyzed by a two-way ANOVA statistical test followed by comparing all groups using Sidak`s multiple comparison test. *p ≤ 0.05, ***p ≤ 0.001, ****p ≤ 0.0001.

2.3.8 LC-MS/MS analysis of advanced glycation end products in mouse kidneys

The analysis of MG-H1 modified proteins showed an increased abundance in *Hspa1a* KO MCEC endothelial cells after acute MG stress (Figure 20). Therefore, the question was addressed whether protein-bound AGEs were also increased in diabetic *Hspa1a* KO mice, as compared to their controls, indicating that HSPA1A is involved in processing of AGE-modified proteins. For this, whole kidney protein lysates were processed and analyzed by liquid chromatography and mass spectrometry (LC-MS/MS). The content of MG-H1 was unchanged in all groups (Figure 41). The glyoxal-derived AGE G-H1 was decreased in diabetic WT mice, as compared to their controls (0.56 nmol/mg vs. 0.49 nmol/mg, p=0.009). CML showed a slight trend to be increased in *Hspa1a* KO mice (0.95 nmol/mg vs. 1.16 nmol/mg, p=ns). CEL was

unchanged in all groups. Fructose-lysine was increased in diabetic WT mice (1.56 nmol/mg vs. 2.93 nmol/mg, p=0.014) and showed the same trend in diabetic *Hspa1a* KO mice (1.99 nmol/mg vs. 2.44 nmol/mg, p=ns), as compared to their respective controls. Glucosepane was also unchanged in diabetic WT (0.0087 nmol/mg vs. 0.0093 nmol/mg, p=ns) and *Hspa1a* KO mice (0.010 nmol/mg vs. 0.0098 nmol/mg, p=ns), as compared to their respective controls.
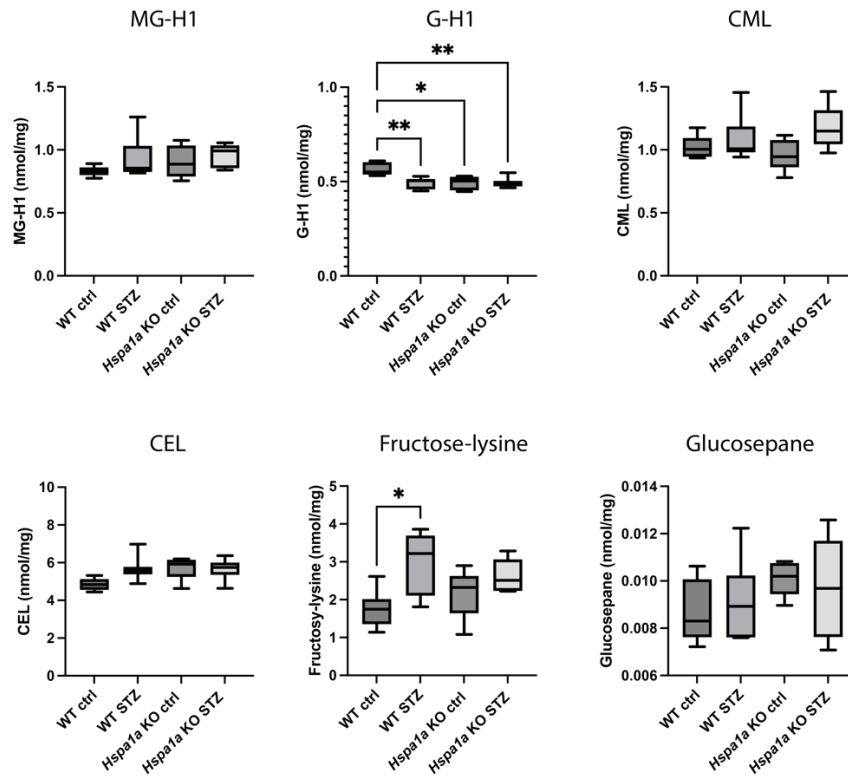
Figure 41 Liquid chromatography and mass spectrometry (LC-MS/MS) analysis of protein-bound advanced glycation end products in mouse kidneys from WT and *Hspa1a* KO control and diabetic mice.

AGEs from whole kidney protein lysates were measured by Dr. Thomas Fleming. WT ctrl: N= 6; WT STZ: N= 7; *Hspa1a* KO ctrl: N= 5, *Hspa1a* KO STZ: N= 6. Data represents mean ± SD, analyzed by a two-way ANOVA statistical test followed by comparing all groups using Sidak`s multiple comparison test. *p ≤ 0.05, **p ≤ 0.01.

3 DISCUSSION

3.1 *Hspa1a* knockout endothelial cell line

Hspa1b and *Hspa1a* are located on the same chromosome (chr17), with only 10.1 kb in between them (Figure 58 in appendix). The two genes consist each of one exon and are 2809 bp (*Hspa1b*) and 2798 bp (*Hspa1a*) long. They differ only in 12 base pairs in their genomic sequence. In their expressed version HSPA1B is one amino acid longer (one insertion of the amino acid proline at position 627), otherwise the sequence is similar. The genome PCR was designed, such that the whole gene, with an additional length of approximately 500 bp surrounding each of the two flanking sites was amplified. As seen in figure 13D, for *Hspa1a* the resulting DNA band was 3.8 kb, as expected. However, the gene amplification of *Hspa1b* only resulted in a PCR product of 800 bp. This suggests that the whole exon must have been missing in the genome of the endothelial cell line MCEC, as well as in the C57BL/6 mouse strain (Figure 28A) that served as the genetic background in the animal experiments. Due to the minor difference, it was concluded that HSPA1A and HSPA1B are essentially the same protein with the same protein function and the lack of one of the two should be compensated by the other. There was no information found in the literature regarding a missing *Hspa1b* gene in other studies of murine cell lines or mouse strains.

The validation of the three independent MCEC *Hspa1a* knockout cell line clones AD4, BE12 and BH9 was performed by qRT-PCR on the mRNA level and western blot on the protein level (Figure 13). The high sequence similarity of *Hspa1a* and *Hspa1b* explains why there was a signal obtained for the mRNA expression of *Hspa1b*, although it was not expressed. Only in the WT cells, the heat-shock induced an increase of HSPA1A expression and thereby a more prominent protein band in the western blot. Since the protein band for HSPA1A did not completely disappear in the KO cells, it was assumed, that the polyclonal anti-HSPA1A antibody is binding non-specifically to another target with the same size. All HSP70 proteins have sequence similarities across themselves, and even conserved sequences among different species. A nucleotide blast search revealed an 85% sequence similarity of *Hspa1l* to *Hspa1a.* Blotting of recombinant HSPA1L and detection with an

anti-HSPA1A antibody, confirmed the assumption of unspecific binding. In combination with the next generation sequencing results and the diminished mRNA expression of *Hspa1a* the three cell lines were confirmed as successful knockout clones of *Hspa1a*.

3.2 Using methylglyoxal to study hyperglycemia-derived carbonyl stress in endothelial cells

3.2.1 Choosing the right concentration of methylglyoxal

MG is a cytotoxic compound that is produced non-enzymatically during glycolysis. Therefore, its potential role in diabetes and diabetes-related complications has been investigated in many studies over the past few decades, *in vitro* and *in vivo*. The first question was, which concentrations of MG should be used in the cell-based experiments. Endogenous concentrations of MG in endothelial cells in normo-glucose medium of 5 mM were reported to be 1.28 pmol/10^6 cells and in high-glucose medium of 20 mM, 2.27 pmol/10^6 cells.[210] Fleming *et al.*[211] used the same mouse cardiac endothelial cell line in this study and determined baseline levels of MG to be 32 pmol/10^6 cells, which is equivalent to 42.6 µM MG.

In the CellTiter Glo® cell viability assay (Figure 14), cellular health started to deteriorate at concentrations of around 500 µM MG. The ED50 values for the WT and the *Hspa1a* KO MCEC, however, showed only a minor difference. Other research groups have used comparable concentrations in their experiments with MG treatment in mammalian cells. Jarisarapurin *et al.*[212] have used a human umbilical cord endothelial cell line, that they treated with different concentrations of MG. MG treatment resulted in a decline in the cell viability already starting at 300 µM MG (cell viability around 95%). They decided to use 800 µM MG for their experiments, where the cell viability only remained at 60%. Additionally, Fleming *et al.*[211] showed that MCEC have lost their proliferative capacity for concentrations above 600 µM MG and underwent cell death at concentrations above 900 µM MG. Thus, the concentration of 500 µM MG that was decided to use for all experiments, was in a range where the cells still showed unchanged viability and proliferative capacity.

62

3.2.2 Accumulation and degradation of MG-H1

The predominant subcellular location of MG-H1 modified proteins (Figure 15A) was found to be in the nucleus and in the cytoplasm, in line with previously reported results.[213] Upon acute MG stress, the amount of detected MG-H1 was higher in the *Hspa1a* KO MCEC (Figures 15A and 15B). This led to the assumption that HSPA1A is involved in the direct processing of MG-H1 modified proteins. However, when the MG-containing medium was removed from the cells, MG-H1 concentrations rapidly decreased in both, WT and *Hspa1a* KO MCEC (Figure 15B). Therefore, it was concluded, that HSPA1A may not be directly involved in removing MG-H1 modified proteins, although the lack thereof certainly led to a higher accumulation of MG-H1 intracellularly. Fleming *et al.*[211] showed that MG-H1 degradation is not performed by the proteasome degradation system. By using MG132, a potent inhibitor of the proteasome, the MG-H1 removal in the cells was not changed. Furthermore, it was shown that proteins glycated with methylglyoxal were a poorer substrate for the ubiquitin-proteasome system (UPS) and the UPS interacted with the lysosomal proteolytic system.[214,215] Eventually, it cannot completely be excluded that the cell's protein repair machinery might compensate for the HSPA1A depletion with the recruitment or induction of other heat-shock proteins, or other degradation pathways.

3.2.3 Methylglyoxal-induced mRNA and protein expression analysis

To investigate how the cells react to MG induced stress, mRNA expression analysis was performed in WT and *Hspa1a* KO MCEC upon acute and chronic MG stress. Multiple treatments with MG were used to mimic *in vivo* conditions, where MG formation occurs continuously through glycolysis. For this, MG was added to the cells daily for a period of one week, every 24 hours. The knockout of *Hspa1a* is especially interesting, as most of the MG-H1 related detrimental effects sooner or later involve an action of the stress-related protein quality control machinery. Furthermore, the chronic stress experiment addressed the question, whether HSPA1A plays an integral part in MG-H1 derived protein or cellular damage, and thus making it a potential target for pharmaceutical induction to prevent such damage. Aside from HSPs, the focus of the mRNA expression analysis was on expression changes of genes that are related to the antioxidant response and inflammatory genes and cytokines that are known to be induced by AGE-RAGE binding. In WT MCEC *Hspa1a* expression was induced after acute (Figure 16) and after chronic MG stress (Figure 23). So far, *Hspa1a*

expression in relation to MG stress was only reported by Zemva *et al.*[216] in a yeast study, where it was also induced. Furthermore, another study in yeast found HSPA1A to be a target of glycation of MG.[108] The expression of heat-shock proteins in stress conditions is mediated by HSF1. The protein expression of HSF1 was found to be increased after acute MG stress (Figure 19), whereas *Hsf1* mRNA expression after acute MG stress was slightly downregulated (Figure 16). For most of the analyzed heat-shock proteins, the expression changes after MG stress showed the same trend for both cell lines, WT and *Hspa1a* KO MCEC. The highest expression increase was seen for *Hspd1* after acute MG stress, a mitochondrial heat-shock protein, which could indicate MG-related mitochondrial stress. Both, HSPA9 and HSPD1 were also upregulated on the protein level (Figure 19). Whether MG-H1 modified proteins misfold or lead to aggregates, was investigated by *Dnajb1* and *Hsph1* expression. DNAJB1 binds to misfolded proteins and together with HSPH1 and HSPA builds a disaggregation complex. After acute and chronic MG stress, *Dnajb1* and *Hsph1* expression showed a trend to be increased, regardless of the genotype. This was also shown for DNAJB1 protein expression (Figure 19). Induction was even more pronounced for the two genes in the *Hspa1a* KO MCEC after chronic stress, which indirectly indicate the increased presence of MG-H1 derived misfolded or aggregated proteins after HSPA1A depletion.

The antioxidant response is mediated by the transcription factor NRF2 and leads to an increased expression of *Nqo1* and *Ho1*. In acute MG stress, only *Hspa1a* KO MCEC showed an increased expression for *Ho1* (Figure 17), whereas after chronic MG stress, both genes showed a trend to be upregulated (Figure 24). This indicates that HSPA1A reduces oxidative stress at least in acute MG stress conditions, whereas in chronic MG stress conditions cells are overwhelmed by oxidative stress even in the presence of HSPA1A in WT MCEC. A similar result was found for HSPB1, which also has antioxidative properties. While *Hspb1* expression was downregulated after acute MG stress, it showed a trend of being upregulated after chronic stress.

An increase in the formation of reactive oxygen species, with an induction of the NRF2-mediated antioxidant response was already reported after MG treatment in *in vitro* cell models.[217–219] In a paper from Bollong *et al.*[220], it was reported that KEAP1 (Kelch-like ECH-associated protein 1), the binding partner of NRF2 is a target for MG modification. After MG-H1-induced cross-linking it dissociates from NRF2, which results in the initiation of the antioxidant response via NRF2 binding to ARE. Thereby,

64

MG can induce the antioxidant response directly by increasing ROS content, but also indirectly through modulation of KEAP1-NRF2 binding. Since the antioxidant response was seemingly not induced in WT MCEC after acute stress (Figure 17), in contrast to *Hspa1a* KO MCEC, one explanation could be that under acute MG stress MG-H1 modification of KEAP1 is sensed and repaired by HSPA1A.

The expression of cytokines and inflammation markers showed a clear difference, when comparing acute and chronic MG stress (Figures 17 and 24). After acute stress, *Gdf15* expression was upregulated, especially in the *Hspa1a* KO MCEC, whereas it was downregulated in chronic MG stress conditions. *Vcam1* and *Icam1* expression was markedly downregulated in both cell lines upon acute MG stress. In WT MCEC *Vcam1* and *Icam1* expression was unchanged after chronic stress, whereas it was three-fold upregulated in *Hspa1a* KO MCEC (only *Vcam1*). This was in concordance with findings from other studies. Expression of the cytokine *TNF-alpha* was reported to be induced by MG in monocytes.[221] TNF-alpha can induce the expression of *Vcam1 via* NF-KB activation. Laga *et al.*[222] showed, that MG dampens the TNF-alpha-induced activation through modulation of the DNA binding of the transcription factor NF-KB.

As mentioned before, the two mitochondrial heat-shock proteins *Hspa9* and *Hspd1* were upregulated upon MG stress. This could hint to increased stress in the mitochondria or a reorganization of the mitochondrial network. Therefore, mitochondria from MG-stressed WT and *Hspa1a* KO MCEC were analyzed regarding differences in mRNA expression, mitochondrial network organization as well as on the metabolic level. Cells, which were only stressed once with MG, showed an increase in *Drp1* expression (Figure 18A), whereas mitochondrial fusion proteins *Mfn1*, *Mfn2* and *Opa1* were not upregulated. After chronic MG stress, *Fis1* showed increased expression (Figure 25A) in both cell types.

To analyze, whether an increase in *Drp1* expression translated into increased fission events, an automated and unbiased approach for the analysis of the mitochondrial network was developed together with Dr. Holger Lorenz from ZMBH Heidelberg. The total number of mitochondria per cell was increased for WT and *Hspa1a* KO MCEC after acute MG stress (Figure 21), which together with Drp1 upregulation could support an increase in mitochondrial fission. However, with a simultaneous increase in total area per cell but no reduction in the size of mitochondria, this was contradictive. This result shows that instead of an activation of mitochondrial fission, the cells produced new mitochondria *via* mitochondrial biogenesis. The effect was even more

pronounced in the *Hspa1a* KO MCEC. And indeed, qRT-PCR results of mitochondrial biogenesis inducing transcription factors *Nrf1*, *Tfam*, *Tfb2m* and mitochondrial protein import proteins *Timm23* and *Timm17a*, revealed an upregulation, however mainly for the *Hspa1a* KO MCEC (Figure 18C). In line with this observation, mitophagy-related genes *Pink1*, *Parkin* and *Bnip3* were all downregulated (Figure 18B). This was also observed in a recent publication with comparable MG stress conditions.[223] Interestingly, *Pgc1a* and *Pgc1b*, that are considered to be the master regulators of mitochondrial biogenesis, were both downregulated after acute MG stress. Mitochondrial network analysis after chronic MG stress showed a different outcome. In WT MCEC, the number of mitochondria did not change (Figure 26) but there was a strong decrease in total area as well as average size of mitochondria, which would indicate increased fission and mitophagy. The mRNA expression analysis of *Parkin* and *Bnip3* confirmed this finding (Figure 25B). Both proteins were seemingly upregulated, hinting to an increased mitophagy activity, especially compared to the downregulation after acute MG stress. For the *Hspa1a* KO MCEC there was a decrease in number of mitochondria, alongside a less pronounced decrease of total area (Figure 26). However, the average size of mitochondria remained unchanged. This would indicate a less active fission, and moderate mitophagy, which is consistent with the results from the mRNA analysis. Furthermore, data revealed that mitochondrial biogenesis was induced. In contrast to acute MG stress, in chronic MG stress the key mitochondrial biogenesis transcription regulator *Pgc1a* was upregulated in *Hspa1a* KO MCEC. Therefore, it must be assumed, that the cells not only degrade faulty mitochondria, but also have a high turnover rate by producing new mitochondria, that are integrated into the existing network to overcome mitochondrial dysfunction. This could be a reaction of the cell to secure the essential supply of sufficient ATP for the energy consuming processes initiated by MG-derived proteotoxic stress. During the progression of diabetes, this might end up in an exhaustion of the system and could lead to mitochondrial dysfunction contributing to the development of diabetic complications.

To evaluate the metabolic capacity and the health state of the mitochondria, a Seahorse mitochondrial stress test was performed in control conditions and under MG stress (Figure 22). MG had little to no effect in all measured parameters in WT as well as in *Hspa1a* KO MCEC after acute MG stress. The bioenergetic health index can be calculated from the parameters measured in the Seahorse assay (spare respiratory

capacity, ATP production, proton leak and non-mitochondrial oxygen consumption).[209] However, the BIH showed no statistically significant changes for both, the WT and *Hspa1a* KO MCEC after acute MG stress. Kim *et al.*[217] have also measured the effect of MG on mitochondrial respiration in brain endothelial cells. They have stressed their cells with 500 µM MG and saw also only minor differences compared to control conditions. Only when they stressed their cells with 1000 µM MG, they found dysfunction of mitochondrial respiration. However, with this high concentration they also reported an increase in PARKIN-mediated mitophagy and a 50% viability rate of their cells. After chronic MG stress, only ATP production and non-mitochondrial oxygen consumption showed an increase, but only in the *Hspa1a* KO MCEC (Figure 27). The bioenergetic health revealed no statistically significant changes in the two cell types.

3.2.4   The methylglyoxal-derived dicarbonyl proteome

The underlying question whether MG or its AGEs act directly through mitochondrial protein modification, or whether the above discussed results are indirect consequences related to fluctuations of the cell's energy demands, remains unclear. Thus, a more in-depth analysis of MG-H1 in mitochondria was performed. In a LC-MS/MS analysis of isolated mitochondria MG-H1 was found to be increased not only in whole cell lysates but also in mitochondrial lysates (Figure 20). However, the identification of mitochondrial MG-H1 modified proteins could not be clarified. Other research groups have found several proteins to be susceptible targets for MG-H1 modification.[224,225] They found proteins from glycolysis, transcription initiation and cell-cell adhesion to be MG-H1 modified just to name a few. Some of them were even modified in their active site. Interestingly, also various heat-shock proteins were found to be MG-H1 modified, including HSPC1, HSPA8, HSPH1, HSPA9, HSPE1 and HSPB1. Rosca *et al.*[226] also found mitochondrial proteins from oxidative phosphorylation and fatty acid beta-oxidation pathways to be MG-H1 modified and link this modification to an excess superoxide formation.

3.3 Consequences of a *Hspa1a* gene knockout in a STZ-induced diabetic mouse model

The aim of this animal study was to find out, whether an increase in hyperglycemia-derived advanced glycation end products is also observed in *Hspa1a* KO mice, and if this increase results in a worsening of the diabetic nephropathy phenotype. In addition to the conventional analysis regarding alterations in glomerulus morphology and albumin excretion, mRNA and protein expression profiles of the protein classes were analyzed, similar to the ones from the *in vitro* analysis.

3.3.1 STZ-induced diabetes and evaluation of the diabetic nephropathy phenotype

The most abundant method to induce diabetes in mouse models is *via* streptozotocin injection. STZ is highly toxic to the insulin producing beta cells in the pancreatic islets, which results in insulitis and type 1 diabetes.[227] Diabetes in mice was diagnosed from blood glucose measurements. As expected, the blood glucose levels were increased in diabetic female and male mice alike (Figure 29).

Albuminuria, the excretion of albumin in urine, is one of the hallmarks of diabetic nephropathy. The measurements of urinary albumin were normalized with urinary creatinine excretion and showed an increase for both WT and *Hspa1a* KO mice (Figures 30 and 46). The degree of albuminuria in diabetic *Hspa1a* KO mice, however, was less severe as compared to diabetic WT mice. In a study from Jheng *et al.*[228] the relationship of albuminuria occurrence and progression was analyzed in relation to HSP70 expression. They found out, that albumin is inducing the release of HSP70 (HSPA1A) in proximal tubule cells of male diabetic mice and that the interplay of HSP70 with toll-like receptor 4 (TLR4) is involved in the development of albuminuria and inflammation processes during diabetes. After blocking of HSP70 they could ameliorate albuminuria and tubular injury. That could explain, the finding in this study, that the UACR was lower in the *Hspa1a* KO mice.

Diabetic kidney disease is also characterized by changes in glomerular morphology, that result in a deficiency of blood filtering and increased excretion of molecules from a lower tubular reabsorption. Glomerular damage can result from a combination of changes. Podocyte lesions, or a loss of podocytes can result in an increase in protein leakage into the Bowman's space, which can be measured by assessing the fractional

mesangial area. Furthermore, the thickening of the GBM is also a common symptom in diabetic nephropathy, which results from glomerulosclerosis, the hardening and scarring of glomerular tissue. The fractional mesangial area was increased in all diabetic mice, with an aggravation for the *Hspa1a* KO mice (Figures 31 and 47). Based on this finding, either the number of podocytes should be reduced in diabetic mice, or there should be an increase in podocyte lesions. The analysis of all groups, however, did not show significant changes in podocyte numbers (Figures 33 and 49). Podocyte injury or lesions (changes in podocyte foot processes) could be an explanation, but they were not analyzed in this study. The third characteristic that was analyzed, was the thickness of the glomerular basement membrane, which can also affect filtration function. While in diabetic WT mice, the increase was only minimal, in diabetic *Hspa1a* KO mice it was higher, as compared to their respective controls (Figures 32 and 48). Although, it must be mentioned, that the number of animals in the KO control group was lower than in the other groups. In addition to albumin excretion, also several electrolytes were analyzed in the urine, that can be a sign for malfunctioning tubular reabsorption in the proximal tubules. Potassium and phosphate levels in urine were higher in diabetic mice (Figures 34 and 50-53), which could indicate increased tubular damage. If the renal loss is high enough, this decrease of electrolytes can also be diagnosed from blood samples, which was not done in these mice. Apart from tubular damage, hormonal changes can lead to a potassium and phosphate decrease in blood, for example hyperaldosteronism[229], hyperparathyroidism[230] or increased FGF23 levels[231], which were not determined in this study.

3.3.2 AGEs in kidneys of diabetic mice

Hyperglycemia-derived AGEs were measured in kidney protein lysates of all four groups (Figure 41). MG-H1 and CML levels were unchanged in diabetic WT mice, and minimally increased in *Hspa1a* KO mice (not statistically significant). While the glyoxal-derived AGE G-H1 showed a lower abundance in diabetic WT mice, it was not different in *Hspa1a* KO mice. The differences for CEL and glucosepane were also neglectable. Only for fructose-lysine a statistically significant increase was found in diabetic WT mice. Taken together, these results showed that a loss of *Hspa1a* is not leading to increased concentrations of AGEs, like it was shown for the concentration increase of MG-H1 in MG treated *Hspa1a* KO MCEC.

3.3.3 mRNA and protein expression in kidneys of diabetic mice

The analysis of heat-shock protein expression in kidney lysates showed an increase of *Hspa1a* in diabetic WT mice (Figure 35). This increase was solely detected in samples from male mice (Figure 54). Western blot analysis of HSPA1A showed a decreased expression (Figure 39), which was mainly due to female mice (Figure 56). IHC-derived protein expression analysis showed no differences in detected HSPA1A signal (Figures 38 and 55). HSPA1A expression was reported to be increased in dilated tubules of diabetic patients.[228] The expression of *Hspa8*, *Dnajb1*, *Hsph1*, and *Hspa9* was downregulated in diabetic animals as compared to their controls. *Hspd1* mRNA expression was downregulated in diabetic WT mice and unchanged in diabetic *Hspa1a* KO mice. On the protein level, however, HSPD1 showed an upregulation in diabetic *Hspa1a* KO mice, and no change in diabetic WT mice. Additionally, *Hspd1* mRNA and protein levels were already strongly reduced in *Hspa1a* KO control mice, as compared to the WT controls. A role of HSPD1 in tubular dysfunction was also discussed by Aluksanasuwan *et al.*[232] *Hspb1* expression was strongly induced in diabetic *Hspa1a* KO mice, which could indicate higher oxidative stress. However, this was not observed on the protein level, where HSPB1 protein expression was decreased in *Hspa1a* KO mice. This is contrary to other findings, where HSPB1 was overexpressed in the diabetic kidney.[233,234] Also, HSPA8 expression showed a contradictory outcome as compared to the mRNA expression results. The protein expression was almost two-fold increased in diabetic *Hspa1a* KO mice. In a study with diabetic rats, HSPB1, HSPD1 and HSPA1A expression levels were found to be increased in the outer renal medulla.[235] The NRF2-mediated antioxidant response was only slightly induced in diabetic mice (Figure 36A). *Nqo1* was also reported to be upregulated in the kidney of diabetic mice.[236] The mRNA expression of the cytokines *Gdf15* and *Vcam1* was increased but mainly in diabetic WT mice (Figure 36B), whereas on the protein levels they were found to be decreased in diabetic animals. In contrast, urinary GDF15 levels were reported to be higher in patients with diabetic nephropathy and correlated with GDF15 protein expression obtained from kidney IHC sections.[237] Two studies revealed a relation of *Vcam1* in diabetic nephropathy. One group reported an increased *Vcam1* expression in renal tubular cells, and the other group found increased plasma VCAM1 levels in patients with diabetic kidney disease.[238,239] The expression levels of *Drp1*, *Fis1*, *Mfn1* and *Opa1* revealed that neither mitochondrial fission, nor fusion was induced (Figure 37A). Other studies have

70

underlined the importance that *Drp1* has on the development of diabetic nephropathy through modulation of the mitochondrial network. In diabetic mice, a podocyte-specific deletion of *Drp1* was successful in attenuating albuminuria and improving the morphology of podocytes, compared to WT controls.[240] Another study has linked *Drp1* overexpression to the manifestation of tubulointerstitial injury.[241] Furthermore, *Parkin* and *Bnip3* levels were unchanged in diabetic mice (Figure 37B). Only *Pink1* was overexpressed in *Hspa1a* KO control mice compared to WT control mice. Audzeyenka *et al.*[242] performed IHC staining in kidney sections from control and diabetic male Wistar rats and observed a lower signal of the mitophagy markers PINK1 and LC3-II. Furthermore, they have isolated glomeruli and performed a Seahorse mitochondrial metabolism analysis. They found a decrease in mitochondrial respiration and ATP production in glomeruli from the diabetic rats. Mitochondrial biogenesis related genes were also mostly downregulated in both WT and *Hspa1a* KO mice (Figure 37C).

3.4 Conclusion and outlook

While in endothelial cells a *Hspa1a* knockout has resulted in increased levels of MG-H1, the clearance of the potential proteotoxic protein modification revealed to be not directly dependent on *Hspa1a*. The mRNA analysis indicated that oxidative stress and inflammation were increased when *Hspa1a* is not present, but the analysis of mitochondria did not reveal any detrimental effects in the knockout cells. In contrast, chronic MG stress even seemed to have a protective effect on mitochondrial homeostasis.

The results from the *in vivo* experiments, however, did show a phenotypical difference between diabetic WT and *Hspa1a* KO mice. Albuminuria was less severe in *Hspa1a* KO mice, which was shown to be in concordance with previous studies, which showed that albumin-induced HSPA1A release increases inflammatory processes *via* TLR4. This could also be observed in this study, with increased expression of *Nqo1*, *Gdf15*, *Vcam1* and *Icam1* in diabetic WT mice. Though this was not the case for all renal pathologies. The glomerular matrix expansion for example, was aggravated in *Hspa1a* KO mice.

Since not all diseases have the same symptomatic appearance or progression between male and female subjects an important aspect of this study was the analysis of mice with respect of their sex. Most of the morphological characteristics in diabetic

nephropathy showed no difference between male and female mice. The only difference found in expression levels was seen for *Hspa1a* in WT mice. mRNA and protein expression of *Hspa1a* was higher in male as compared to female diabetic mice. Whether these changes have any influence in terms of onset or progression of diabetic nephropathy will need further investigation. Most of the studies that were found during the literature research were conducting experiments only in male Wistar rats or did not mention sex-specific differences in their outcomes.

The results of this study show that endothelial cells can compensate the loss of *Hspa1a* to cope with MG-derived stress. Therefore, it could be assumed that a reduced *Hspa1a* expression or activity, which can be the result of genetic polymorphisms or mutations, is not directly associated with inducing endothelial dysfunction.

Other than initially expected, a HSPA1A reduction or inhibition *in vivo*, could be an interesting therapeutic approach to mitigate albuminuria and with that an albuminuria-induced progression of diabetic kidney disease.

4 MATERIALS AND METHODS

4.1 Materials

4.1.1 Antibodies

Table 3 Primary antibodies

Target protein	Manufacturer	Catalog nr.
HSPA1A/HSPA1B	Proteintech	10995-1-AP
MG-H1 (biotin labeled)	Self-made (see section 4.2.9)	
HSPA9	Invitrogen	MA3-028
HSPD1	Cell Signaling Technology	12165
HSPA8	Merck Millipore	MABE1120
HSF1	Cell Signaling Technology	12972
HSPB1	Cell Signaling Technology	2442
HSPC1	Cell Signaling Technology	4877
DNAJB1	Invitrogen	PA-17382
HO1	Invitrogen	MA1-112
GDF15	Proteintech	27455-1-AP
VCAM1	Cell signaling technology	32653
DRP1	Proteintech	12957-1-AP
MFN1	abcam	ab126575
PARKIN	Proteintech	14060-1-AP
HSPA9	Invitrogen	PA5-79410
WT1	Abnova	MAB20854
COX1	abcam	ab14705

Table 4 Secondary antibodies and dyes

Antibody/dye	Label	Manufacturer	Catalog nr.
Streptavidin	Alexa Fluor® 647	Biolegend	405237
Anti-mouse IgG	Alexa Fluor® 488	Cell signaling technology	4408
Anti-mouse IgG	Alexa Fluor® 594	Cell signaling technology	8890
Anti-rabbit IgG	Alexa Fluor® 488	Cell signaling technology	4412
Anti-rabbit IgG	Alexa Fluor® 594	Cell signaling technology	8889
IRdye®Streptavidin	800 CW	LI-COR	926-32230
POLYVIEW® Plus AP anti-rabbit	Alkaline Phosphatase (AP)	Enzo Life Sciences	ENZ-ACC110-0150
Permanent AP-red-kit	AP	Zytomed	ZUCC01-125

4.1.2 Bacterial strains, cell lines and mouse strains

Table 5 Bacterial strains, cell lines and mouse strains

	Manufacturer	Catalog nr.
DH5alpha competent cells	Invitrogen	18265017
Mouse cardiac endothelial cell line	Cellutions Biosystems	CLU510
B6;129S7-del(17*Hspa1b-Hspa1a*)1dix/mmucd	MMRC	000371-UCD

4.1.3 Buffers

Table 6 Buffers

Buffer	Manufacturer	Catalog nr.
Phosphate-buffered saline	Sigma Aldrich	D8537
Protein-free T20 blocking buffer	Thermo Scientific™	37573
RIPA lysis buffer	Thermo Scientific™	89901
Restore™ western blot stripping buffer	Thermo Scientific™	21059

4.1.4 Cell culture medium components

Table 7 Cell culture medium components

Component	Manufacturer	Catalog nr.	End concentration
DMEM (Dulbecco's modified eagle medium)	Gibco	31885-023	
Penicillin-streptomycin (10.000 U/mL)	Gibco	15140-122	100 U/mL
Amphotericin B 250 µg/mL	Gibco	15290-026	5 µg/mL
Fetal calf serum	Gibco	10082-147	10% (v/v)
HEPES 1 M	Gibco	15630-080	10 mM

4.1.5 Chemicals

Table 8 Chemicals

Chemical	Manufacturer	Catalog nr.
CellTag™ 700	LI-COR	926-41090
Agarose powder	Applichem	A2114
Luria-Bertani medium	Applichem	A6666
Nonfat dry milk powder	Applichem	A0830
GelRed™ 10000x in water	Biotium	41003

Q5® Hot start high-fidelity 2x master mix	New England Biolabs	M0494S
Kanamycin sulfate	Gibco	15160-054
Methylglyoxal	Sigma-Aldrich	M0252
Gelatin	Sigma-Aldrich	G9391
PowerUp™ SYBR™ Green master mix	Applied Biosystems	A25777
TrypLE™ express enzyme	Gibco	12605-010
Proteinase inhibitor cocktail	Cell Signaling Technology	5872
Benzonase	Novagen	70746-3
Protein Assay Dye	Bio-Rad	5000001
Tween20	Thermo Scientific™	003005
Goat serum	Sigma-Aldrich	G9023
Paraformaldehyde	Thermo Scientific™	047340.9M
Triton X-100	Sigma-Aldrich	X100
Bovine serum albumin	Sigma-Aldrich	A9647
Hoechst 33342	Thermo Scientific™	62249
Seahorse XF base medium	Agilent	102353-100
Oligomycin	Sigma-Aldrich	O4876
FCCP	Sigma-Aldrich	C2920
Rotenone	Sigma-Aldrich	R8875
Antymycin-a	Sigma-Aldrich	A8674
Sodium phosphate	Sigma-Aldrich	342483
Streptozotocin	Sigma-Aldrich	572201
Insulin	Sigma-Aldrich	I5523
Formalin	Sigma-Aldrich	HT501128
iBright™ prestained protein ladder	Invitrogen	LC5615
GeneRuler DNA ladder	Thermo Scientific™	SM0333
TRIS	Sigma-Aldrich	T1699
EDTA	Sigma-Aldrich	E9884
Target retrieval solution	Dako	S1699
UltraPure water	Cayman Chemical Company	Cay400000-1
Pepsin	Sigma-Aldrich	1071850100
Pronase E	Sigma-Aldrich	1074330001
Prolidase	Sigma-Aldrich	P6675-250UN
Aminopeptidase	Sigma-Aldrich	A8200-100UN
Trifluoroacetic acid	Sigma-Aldrich	302031
Tetrahydofuran	Sigma-Aldrich	401757

4.1.6 Consumables

Table 9 Consumables

Description	Manufacturer	Catalog nr.
T75 cell culture flask	Sarstedt	83.3911.002
Falcon 50 ml	Corning	14-959-49A
Falcon 15 ml	Corning	14-959-53A

Safe-lock tubes 1.5 ml	Eppendorf	0030120086
Safe-lock tubes 0.5 ml	Eppendorf	0030121023
Tubes 5 ml	Eppendorf	0030119401
4–20% Mini-PROTEAN® TGX™ Precast Protein Gels	Bio-Rad	4561096
Seahorse XF96 fluxpack	Agilent	101085-004
BZO seal film	Biozym	712350
PCR 96-well TW-MT-plate	Biozym	712260
Cellview microplate 96-well	Greiner bio-one	655891
Cell culture microplate 96-well	Greiner bio-one	655098
FP 30/0.2 CA-S filter unit	GE Healthcare Life Sciences	10462200
PCR tubes	Biozym	711080
Hypercarb™ chromatography column	Thermo Scientific™	35005-052130
Hypercarb™ chromatography column	Thermo Scientific™	35005-152130
Protein purification spin columns, 10 kDa cutoff	Amicon	UFC501096

4.1.7 Devices

Table 10 Devices

Description	Manufacturer
ThermoMixer® C	Eppendorf
ProFlex PCR system	Applied Biosystems
SPECTROstar Omega plate reader	BMG Labtech
Trans-blot® turbo™ transfer system	Bio-Rad
StepOnePlus™ Real-Time PCR system	Applied Biosystems
ChemiDoc™ MP imaging system	Bio-Rad
Odyssey® DLx imaging system	LI-COR
IX81 widefield fluorescence microscope	Olympus
Rocking shaker DRS-12	neoLabLine
Seahorse XF96 Analyzer	Agilent
AU400 chemistry analyzer	Olympus
ADVIA® chemistry XPT analyzer	Siemens
Bacterial shaker KS 4000 i control	IKA
Heracell CO_2 incubator	Heraeus
Light microscope AX10	Zeiss
Biological safety cabinet safe 2020	Thermo Scientific™
VWB 12 water bath	VWR
Centrifuge 5430 R	Eppendorf
pH meter pH 540 GLP	WTW
Hot plate stirrer MR Hei-Standard	Heidolph
Analytical balance ABJ-NM/ABS-N	KERN

Balance EG	KERN
ACQUITY ultra-high-performance liquid chromatography system	Waters™
XEVO-TQ-S LC-MS/MS spectrometer	Waters™

4.1.8 Kits

Table 11 Kits

Description	Manufacturer	Catalog nr.
RNeasy mini kit	Qiagen	74104
Plasmid mini kit	Qiagen	12123
Plasmid midi kit	Qiagen	12143
High-capacity cDNA reverse transcription kit	Applied Biosystems	4368813
Avidin/biotin blocking kit	Linaris	SP-2001
CellTiterGlo® luminescent cell viability assay	Promega	G7572
Mitochondria isolation kit	Miltenyi Biotec	130-096-946
Mouse albumin ELISA	Alpco	41-ALBMS-E01
Creatinine kit	Beckman Coulter	OSR6178
Trans-Blot Turbo midi 0.2 µm nitrocellulose transfer packs	Bio-Rad	1704159
Neon™ transfection system 100 µL-kit	Invitrogen™	MPK10096
ECL western blotting detection reagent	GE Healthcare	RPN2232
EZ-Link™ NHS-PEG4 biotinylation kit	Thermo Scientific™	21455

4.1.9 Plasmid DNA

Table 12 Plasmid DNA

Description	GRNA TARGET SEQUENCE	Manufacturer	Catalog nr.
Hspa1a-gRNA-Cas9-GFP	TGTGCTCAGACCTGTTCCG	Sigma-Aldrich	MM00018-0193740
Hspa1b-gRNA-Cas9-GFP	CGGTTCGAAGAGCTGTGCT	Sigma-Aldrich	MM00026-0015511
GFP-N1		Takara Bio	632515

4.1.10 qRT-PCR primers

Table 13 qRT-PCR primers

Gene	Forward primer	Reverse primer
Hprt	TCAGTCAACGGGGGACATAAA	GGGGCTGTACTGCTTAACCAG
Hspa1a	TGGTGCAGTCCGACATGAAG	GCTGAGAGTCGTTGAAGTAGGC
Hspa1b	GAGATCGACTCTCTGTTCGAGG	GCCCGTTGAAGAAGTCCTG
Hspa9	ATGGCTGGAATGGCCTTAGC	ACCCAAATCAATACCAACCACTG
Hspd1	ACAGTCCTTCGCCAGATGAGA	ACCTTGAAGCATTAAGGCTCG
Dnajb1	TTGGAGGAACCCCTCGTCA	CTCTTGCCGACAGTTGCATTT
Hspa8	TCTCGGCACCACCTACTCC	CTACGCCCGATCAGACGTTT
Hsph1	GGGCTAGACGTAGGCTCACA	CCACCATTTTTCATTGGGACCA
Hspb1	CTCTATCCCATGATGGCATCCT	CTCAACTCTGGCTATCTCTTCCT
Hsf1	GGGAAACAGGAGTGTATGGACT	CTTGTTGACAACTTTTTGCTGCT
Nrf2	CTGAACTCCTGGACGGGACTA	CGGTGGGTCTCCGTAAATGG
Nqo1	AGGATGGGAGGTACTCGAATC	AGGCGTCCTTCCTTATATGCTA
Ho1	AAGCCGAGAATGCTGAGTTCA	GCCGTGTAGATATGGTACAAGGA
Hspc1	AATTGCCCAGTTAATGTCCTTGA	CGTCCGATGAATTGGAGATGAG
Drp1	CAGGAATTGTTACGGTTCCCTAA	CCTGAATTAACTTGTCCCGTGA
Fis1	TGTCCAAGAGCACGCAATTTG	CCTCGCACATACTTTAGAGCCTT
Opa1	TGGAAAATGGTTCGAGAGTCAG	CATTCCGTCTCTAGGTTAAAGCG
Mfn1	ATGGCAGAAACGGTATCTCCA	CTCGGATGCTATTCGATCAAGTT
Mfn2	ACCCCGTTACCACAGAAGAAC	AAAGCCACTTTCATGTGCCTC
Parkin	GAGGTCCAGCAGTTAAACCCA	CACACTGAACTCGGAGCTTTC
Bnip3	TCCTGGGTAGAACTGCACTTC	GCTGGGCATCCAACAGTATTT
Pink1	TTCTTCCGCCAGTCGGTAG	CTGCTTCTCCTCGATCAGCC
Hspa5	ACTTGGGGACCACCTATTCCT	ATCGCCAATCAGACGCTCC
Hspe1	AGTTTCTTCCGCTCTTTGACAG	TGCCACCTTTGGTTACAGTTTC
Vcam1	TTGGGAGCCTCAACGGTACT	GCAATCGTTTTGTATTCAGGGGA
Icam1	GTGATGCTCAGGTATCCATCCA	CACAGTTCTCAAAGCACAGCG
Gdf15	CTGGCAATGCCTGAACAACG	GGTCGGGACTTGGTTCTGAG
Tomm7	ATCCGCTGGGGCTTTATTCC	CGACGGTTCAGGCATTCCA
Timm23	GAAGGTGGCGGAAGAAGTAGC	GGGGGGTTCATACCAGTCAGC
Timm17a	TGCCCCTGGCGAATTGTAG	CTGTCAAACTTCCTCGGAGTC
Pgc1a	TTCATCTGAGTATGGAGTCGCT	GGGGGTGAAACCACTTTTGTA

Gene	Forward	Reverse
Pgc1b	TGTGACCCTACCCACAAGGA	GCTCTGGTAAGGGCAGTGA
Nrf1	TATGGCGGAAGTAATGAAAGACG	CAACGTAAGCTCTGCCTTGTT
Tfam	ATTCCGAAGTGTTTTTCCAGCA	TCTGAAAGTTTTGCATCTGGGT
Tfb2m	GGCCCATCTTGCATTCTAGGG	CAGGCAACGGCTCTATATTGAAG

4.1.11 Sequencing primers

Table 14 Sequencing primers

Gene	Forward	Reverse
Hspa1a	ACCTCCAAACACAACAGGCA	CGTCCAGCCCCATTTCTTCT
Hspa1b	CTGGAGGGTAAGGGAGAGCT	GGGGAGACATGGACAAGCAA
Mycoplasma detection	GGGAGCAAACAGGATTAGATACCCT	TGCACCATCTGTCACTCTGTTAACCTC

4.1.12 Software

Table 15 Software

Software	Version	Source
Fiji	2.1.0/1.53c	https://imagej.net/software/fiji/
Graphpad prism	9.4.0 (453)	https://www.graphpad.com/
QuPath	0.3.2	https://qupath.github.io/
scanR acquisition		https://www.olympus-sis.com
Seahorse wave software		https://www.agilent.com
Image Studio™ Lite		https://www.licor.com
MassLynx	4.1	https://www.waters.com
TargetLynx	2.7	https://www.waters.com

4.2 Methods

4.2.1 Cell culture of MCEC

The immortalized murine cardiac endothelial cell line (MCEC) was purchased from Cellutions Biosystems. Cells were cultivated in DMEM supplemented with 5% (v/v) fetal calf serum (FCS), 1% penicillin-streptomycin (100 U/mL), 1% amphotericin B (5 µg/mL) and 10 mM HEPES ((4-(2-hydroxyethyl)-1-piperazineethanesulfonic acid)) in a humidified atmosphere at 37°C and 5% CO_2. The cell culture flasks were coated with 0.5% (w/v) gelatin solution for 15 minutes at 37°C to ensure a better attachment of the cells. For passaging, cells were grown to full confluency and detached from the flask bottom using 1x TrypLE™ dissociation reagent for 10 minutes. The cells were then resuspended in growth medium and a fraction of the cell solution (e.g., 1:15 for a 3-day incubation) was transferred to a new cell culture flask.

4.2.2 Mycoplasma screening

A screening for mycoplasma contamination was performed every four weeks on all cell lines. 100 µL of supernatant was removed from the cell culture and heat-inactivated at 98°C for 5 minutes. After 2 minutes centrifugation at 10,000 rpm, 2 µL were used for polymerase chain reaction and loaded on an 2% agarose gel. The resulting PCR product from a contaminated culture, or the positive control, was 280 bp.

4.2.3 Polymerase chain reaction

Polymerase chain reactions for the amplification of certain genomic DNA loci were performed with the Q5® Hot Start High-Fidelity 2x Master Mix with the following reaction setup:

Table 16 PCR reaction mix

Component	25 µL reaction
Q5 High-Fidelity 2x Master Mix	12.50 µL
10 µm forward primer	1.25 µL
10 µm reverse primer	1.25 µL
Template DNA	1.00-2.00 µL
Nuclease-free water	to 25.00 µL

The thermocycler conditions were as follows:

Table 17 Thermocycler reaction conditions

Step	Temperature	Time
Initial denaturation	98°C	30 seconds
	98°C	10 seconds
35 cycles	55°C	15 seconds
	72°C	20-30 seconds/kb
Final extension	72°C	2 minutes
Hold	4°C	

4.2.4 Agarose gel electrophoresis

PCR products and plasmid DNA were analyzed using DNA agarose gel electrophoresis. Agarose was dissolved in 1x tris/borate/ETDA buffer (TBE) at a concentration between 1-2% (w/v) by heating in a microwave for 2 minutes. Subsequently, GelRed™ solution was added to a final concentration of 1% (v/v). After a cooling time of 10 minutes the solution was poured in a plastic compartment with a comb for the loading pockets. The gel was then placed in the running chamber, filled with 1x TBE buffer. After loading of the samples and the DNA marker, the gel was run at 110 Volts for 60 minutes. The image was taken on a ChemiDoc™ MP imaging system.

4.2.5 Bacterial transformation and plasmid amplification

The DNA vector, containing the *Hspa1a* gene targeting gRNA (guide RNA) sequence, Cas9 enzyme, kanamycin resistance gene and green fluorescent protein reporter gene was purchased from Sigma-Aldrich. Plasmid amplification was performed with competent Escherichia coli (strain DH5 alpha) bacterial cells. 50 µL of competent cells were thawed on ice for 30 minutes. Then 10 ng of vector DNA was added, gently mixed and incubated on ice for 30 minutes. Then the cells were submerged in a 42°C tempered water bath for 20 seconds, and subsequently put on ice for 2 minutes. Then, 950 µL of pre-warmed (37°C) lysogeny-broth (LB) medium was added to the bacteria and incubated on a 37°C heat-block, shaking at 500 revolutions per minutes (rpm) for 45 minutes. Then, 200 µL of the bacterial solution was spread on kanamycin agar plate, and incubated overnight at 37°C. On the next day, single colonies were picked and incubated in 5 mL LB medium with 250 µg/mL kanamycin at 37°C and 250 rpm

overnight. The following day, 1-2 mL of bacterial solution was transferred to an Erlenmeyer flask in 100 mL LB medium with 250 µg/mL kanamycin at 37°C and 250 rpm overnight. The next day, a plasmid midi prep was performed to isolate the amplified vector DNA from the bacterial cells, according to the manufacturer's protocol.

4.2.6 CRISPR/Cas9 knockout cell line generation

The cells were transfected (Neon electroporation transfection system) with vectors targeting the *Hspa1a* and *Hspa1b* genes. The electroporation parameters were: Pulse voltage: 1200 V; pulse width: 30 ms; pulse no.: 1. The vector contained the gRNA target sequence, the Cas9 endonuclease gene and the fluorescent reporter gene green fluorescent protein. After 48 hours, fluorescence activated single cell sorting was performed to detect and isolate GFP expressing cells. Cells were grown to a sufficient amount for further genome, mRNA and protein analysis to confirm a successful gene knockout in the isolated clonal cell lines.

4.2.7 Heat-shock experiment

1×10^6 MCEC cells were incubated in 1 mL growth medium in a 1.5 mL Eppendorf tube in a heating block at 42°C for 30 minutes. The cells were then transferred to an incubator with a humidified atmosphere at 37°C and 5% CO_2 for three hours. Then, the cells were centrifuged for 5 minutes at 1,400 rpm and the cell pellets were subsequently frozen at - 80°C until RNA or protein isolation was performed.

4.2.8 Methylglyoxal treatment

75,000 cells/cm² were transferred to gelatin-coated (0.5% (w/v) in PBS for 15 minutes) tissue culture plate. On the next day, one hour before the MG treatment, the medium was replaced with assay medium (0.1% FCS). Then, a solution of 500 µM methylglyoxal in assay medium was prepared to replace the assay medium. The cells were incubated in a humidified atmosphere at 37°C and 5% CO_2. For 12 (mRNA analysis) or 24 hours (protein analysis). For the chronic MG stress experiments, the assay medium containing 500 µM MG was added to the cells every 24 hours for 7 consecutive days.

4.2.9 MG-H1 antibody generation

The rat monoclonal antibody targeting the advanced glycation end product MG-H1, was developed at the Helmholtz Centre in Munich.[243] To improve detection, affinity purified antibody was conjugated to [PEG]4-Biotin using the EZ-Link™ NHS-PEG4 biotinylation kit, following the manufacturer's instructions.

4.2.10 RNA isolation and cDNA transcription

After 12 hours of MG stress, the cells were harvested. mRNA was isolated from the cells using the RNeasy Mini Kit from Qiagen according to the manufacturer's instructions. For cDNA transcription of isolated total RNA 2 µg were used with the High-Capacity cDNA Reverse Transcription Kit without RNase inhibitor. The reaction setup was as follows:

Table 18 cDNA transcription mix

Component	20 µL reaction
10X RT buffer	2.00 µL
10X RT random primer	2.00 µL
25X dNTP mix (100 mM)	0.80 µL
Multiscribe reverse transcriptase (50 U/µL)	1.00 µL
Nuclease-free water	4.20 µL
RNA	2.00 µg in 10.00 µL

The thermocycler conditions were as follows:

Table 19 cDNA transcription thermocycler reaction conditions

Steps	Temperature	Time
1	25°C	10 minutes
2	37°C	120 minutes
3	85°C	5 minutes
4	4°C	Hold

After cDNA transcription, the cDNA was diluted 1:25 in nuclease-free water and stored at -20°C.

4.2.11 Quantitative Real-Time PCR (qRT-PCR)

qRT-PCR was conducted with the PowerUp™ SYBR™ Green Master Mix. The Real-Time PCR System that was used was the StepOnePlus™ machine from Applied Biosystems. mRNA levels were normalized to the expression of the housekeeping gene hypoxanthine-guanine phosphoribosyl transferase (*Hprt*). Calculation of the expression fold-changes was performed with the ΔΔCt method[244]. The reaction setup was as follows:

Table 20 qRT-PCR reaction mix

Component	12 µL reaction
PowerUp™ SYBR™ green master mix	6.00 µL
10 µm forward primer	0.36 µL
10 µm reverse primer	0.36 µL
cDNA	2.00 µL
Nuclease-free water	3.28 µL

The thermocycler conditions for the run and the dissociation melting curve are shown in tables 21 and 22.

Table 21 StepOnePlus standard qRT-PCR reaction conditions

Step	Temperature	Time
UDG activation	50°C	2 minutes
Dual-lock™ DNA polymerase	95°C	2 minutes
40 cycles	95°C	15 seconds
	60°C	1 minutes

Table 22 StepOnePlus qRT-PCR dissociation melt curve conditions

Step	Ramp rate	Temperature	Time
1	1.6°C/second	50°C	15 seconds
2	1.6°C/second	60°C	1 minute
3	0.15°C/second	95°C	15 seconds

4.2.12 Protein isolation, SDS PAGE and western blotting

After 24 hours of MG stress, the cells were harvested with TrypLE™ dissociation reagent. Cell lysis was performed in 200 µL radioimmunoprecipitation buffer

(RIPA: 50 mM Tris-HCl, 150 mM NaCl, 1% (v/v) Triton X-100, 0.5% (w/v) sodium deoxycholate, 0.1% (w/v) SDS (sodium dodecyl sulfate), 1 mM ethylenediaminetetraacetic acid (EDTA)) with 1x proteinase inhibitor cocktail and 0.5% (v/v) benzonase for 30 minutes on ice with occasional vortexing. Then, the lysates were centrifuged for 15 minutes at 14,000 rpm at 4°C and the supernatant was transferred to a new tube. The protein concentration was measured with a Bradford assay. 10 µg of the cell lysates were mixed with 4x Laemmli sample buffer (200 mM Tris-HCl pH 6.8, 8% (w/v) SDS, 40% (v/v) glycerol, 20% (v/v) beta-mercaptoethanol, 0.002% (w/v) bromophenol blue) and heated to 95°C for 5 minutes. Protein separation was performed *via* SDS-PAGE (polyacrylamide gel electrophoresis) using pre-casted Mini-PROTEAN® TGX gels (4–20% acrylamide) at 150 V for one hour. Proteins transfer was performed using a Trans-Blot® Turbo™ transfer system with the standard program. The membrane was incubated in blocking solution (1x tris-buffered saline (TBS) with 0.1% (v/v) Tween20 and 5% (w/v) milk powder). Endogenous biotin binding sites were blocked with and a biotin blocking kit according to the manufacturer's protocol. Membranes were covered with the primary antibody solution in blocking buffer in dilutions of 1:1,000 - 1:10,000 at 4°C overnight. Incubation with the secondary antibody was also done in blocking buffer in dilutions of 1:500 - 1:1,000 for one hour at room temperature. Washing of the membrane was done in three cycles of 10 minutes each at room temperature with TBS-T in between all steps. Imaging of the membranes was performed on a ChemiDoc™ MP imaging system with enhanced chemiluminescence detection reagent or via immunofluorescence with the Odyssey® DLx system (LI-COR).

4.2.13 Bradford protein assay

The protein concentration of protein lysates was measured by Bradford assay.[245] Protein lysates were diluted in water 1:20 and 10 µL pipetted in duplicates on a clear 96-well plate. For the standard curve, solutions of bovine serum albumin ranging from 1 µg/mL to 6 µg/mL in water were prepared and pipetted on the plate in duplicates. Then, a 1:5 dilution of protein assay dye in water was prepared and 190 µL added to the protein samples on the plate. After an incubation of 5 minutes at room temperature, the absorbance at 595 nm was measured on a SPECTROstar Omega plate reader.

4.2.14 Immunocytochemistry

24 hours after treatment, the cells were fixed using paraformaldehyde solution 4% (w/v) in 1x PBS for 20 minutes at room temperature. Permeabilization was done using 0.1% (v/v) Triton X-100 in 1x PBS for 8 minutes. Then, blocking was performed with 3% (w/v) BSA (bovine serum albumin) in 1x PBS for 60 minutes on a rocking shaker. The incubation of cells with the primary antibody was done in blocking buffer in dilutions of 1:50 - 1:1,000 and incubated overnight at 4°C. The incubation of cells with the secondary antibody was done in blocking buffer in dilutions of 1:500 - 1:1,000 and incubated at room temperature for 60 minutes on a rocking shaker. Staining of the nuclei was done with Hoechst 33342 (1 µg/mL in 1x PBS) for two minutes at room temperature on a rocking shaker. Washing of the cells was done in three cycles of 5 minutes each at room temperature with 1x PBS in between all steps.

4.2.15 Widefield microscopy

Images acquisition was performed on an automated screening widefield microscope using scanR acquisition. The 60X objective and the following filters were used: DAPI filter (4′,6-diamidino-2-phenylindole; excitation at 358 nm; emission maximum: 461 nm), GFP filter (excitation at 395 nm; emission at 475 nm) and mCherry filter (excitation at 597 nm; emission maximum: 610 nm).

4.2.16 MG clearance assay and in-cell western blot

MCECs were treated with 500 µM MG for 24 hours. Then, MG-containing medium was replaced with assay medium. 24, 48 and 72 hours after medium change, the cells were fixed using paraformaldehyde solution 4% (w/v) in 1x PBS for 20 minutes at room temperature. Permeabilization was done using 0.1% (v/v) Triton X-100 in 1x PBS for 8 minutes. Then, blocking was performed with 3% (w/v) BSA (bovine serum albumin) in 1x PBS for 60 minutes on a rocking shaker. The incubation of cells with the primary antibody was done in blocking buffer in dilutions of 1:100 and incubated overnight at 4°C. The incubation of cells with the secondary antibody was done in blocking buffer in a dilution of 1:500 and incubated at room temperature for 60 minutes on a rocking shaker. CellTag™ 700 dye was added to the secondary antibody solution in a dilution of 1:500 to normalize for total protein content. Washing of the cells was done in three cycles of 5 minutes each at room temperature with 1x PBS in between all steps.

4.2.17 Image analysis

Fluorescence microscopy image analysis was performed using Fiji, a Java-based image processing program which is based on ImageJ.[246] In-cell western blots were analyzed in Image Studio Lite. Kidney sections were analyzed with QuPath and Fiji.

4.2.18 Mitochondrial network analysis

The mitochondrial network analysis was performed with an imageJ plugin provided by Holger Lorenz (ZMBH, Heidelberg). The macro requires multicolor images, in this case a merge of the mitochondrial antibody staining (COX1) and a Hoechst 33342 nuclear counterstain. Figure 42 shows is a depiction of the user interface that allows the modification of the analysis settings.
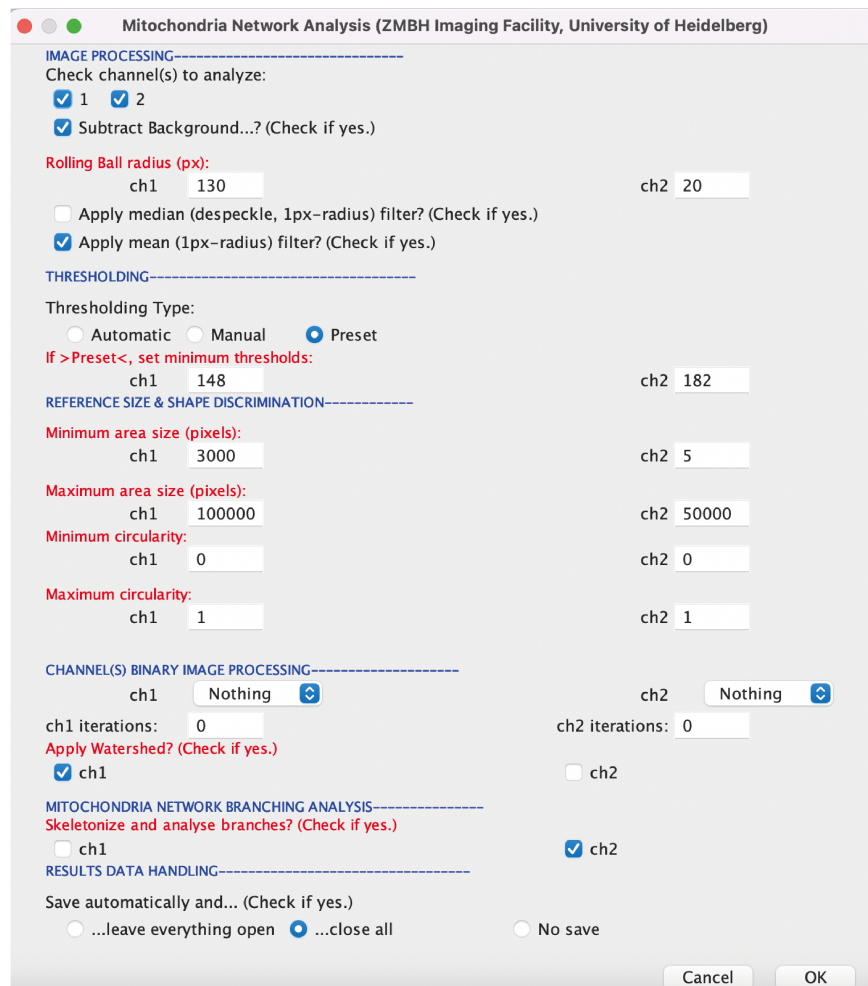
Figure 42 User interface for the mitochondria network analysis plugin.
The plugin was programmed by Dr. Holger Lorenz.

The software then converts the images in a binary mask. Then the signal is processed *via* thresholding and skeletonized. From the resulting images the software then isolates the information for number and size of the detected particles, as well as the total fluorescence signal that was measured. In figure 43, an example of the workflow is shown.

Figure 43 Workflow with example images for the mitochondrial network analysis plugin.

4.2.19 CellTiter-Glo® luminescence cell viability assay

After 24 hours of MG stress, the cells were removed from the incubator for 30 minutes to equilibrate to room temperature. Then, a volume of CellTiter-Glo® reagent, equal to the volume of the cell culture medium was added to each well. Then the plates

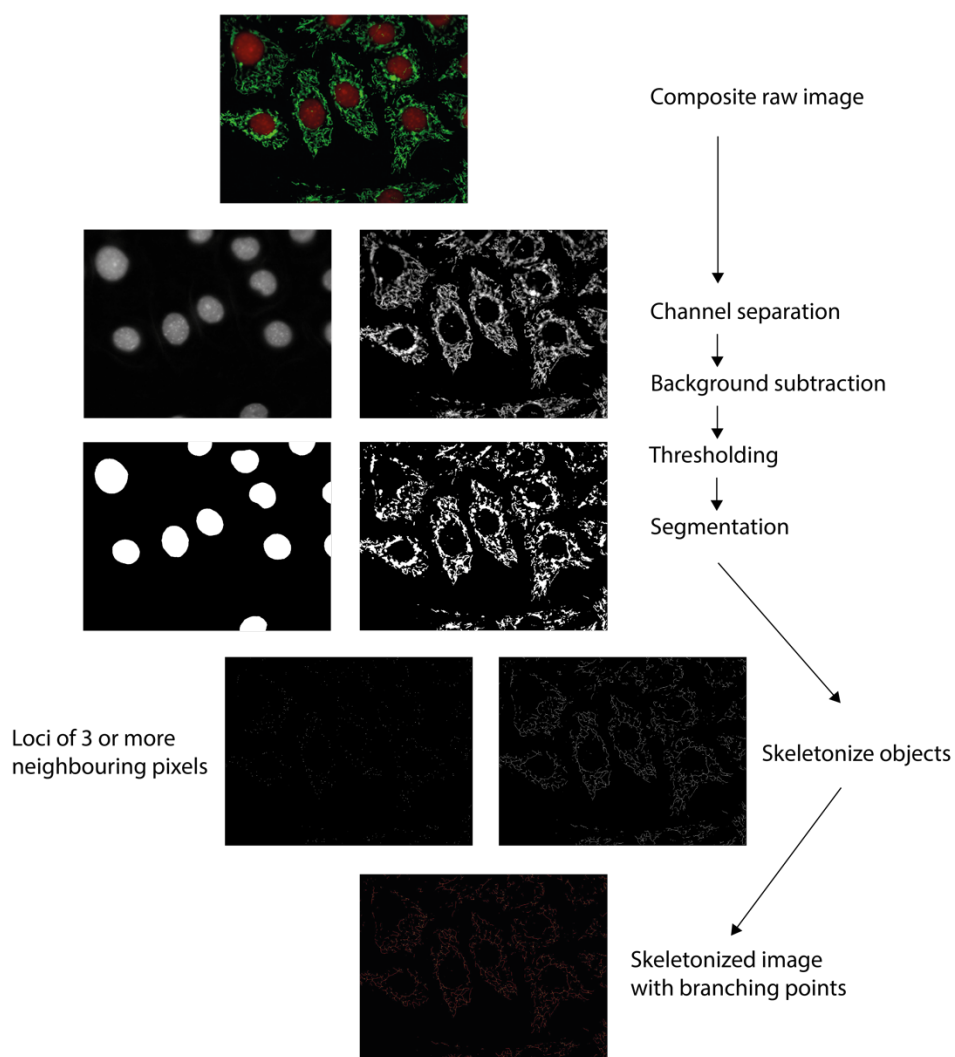were incubated on a rocking shaker for two minutes, following by an incubation at room temperature for 10 minutes. Then the luminescence was measured on a SPECTROstar Omega plate reader.

4.2.20 Seahorse XF Cell mitochondrial stress test

The Seahorse XF96 Bioanalyzer was used to analyze mitochondrial respiration parameters.[247] 75,000 cells/cm² were seeded in 100 µL growth medium in a XF96-well fluxpack. The next day, the medium was replaced with assay medium containing 500 µM MG and incubated at 37°C for 24 hours. Then, medium was changed to the Seahorse XF base medium and incubated for one hour prior to the assay in a non-CO_2 incubator at 37°C. Oligomycin (2 µM in base medium), FCCP (1 µM in base medium), and rotenone/antimycin-A (0.5 µM each in base medium) were loaded in the injection ports of the machine. After an internal calibration, the plate was placed in the device and the program started. Analysis of the data was done by the proprietary Seahorse wave software. Total protein content, measured by a Bradford assay, was used to normalize the data.

4.2.21 Mitochondrial isolation

1×10^7 MCEC were harvested 24 hours after MG treatment and mitochondria were isolated with a mitochondria isolation kit according to the manufacturer's protocol. First, cells were resuspended in lysis buffer and lysed by passing through a syringe needle 20 times. Then the lysate is mixed with 9 mL 1x separation buffer and 50 µL of anti-TOMM20 magnetic MicroBeads and put on a rocking shaker for one hour at 4°C. Then the lysate was loaded onto a MACS column, that was placed on a MACS magnetic separator. The magnetically labeled mitochondria are thereby retained in the column. After three washing cycles with 1x separation buffer, the column is removed from the magnetic separator and the mitochondria are eluted with 1x separation buffer into an empty 1.5 mL tube. Isolated mitochondria were then centrifuged at 13,000 g for two minutes at 4°C. Then, the supernatant was removed, and mitochondria were resuspended in storage buffer and stored at 4°C until further analysis.

4.2.22 AGE measurement via LC-MS/MS

Protein-bound AGEs in the kidneys and endothelial mitochondrial isolations were determined by isotope dilution, tandem mass spectroscopy by Dr. Thomas Fleming, as previously described.[248] Briefly, 10 mg of total protein extracts from the kidney were prepared by homogenization in 10 mM sodium phosphate buffer (pH 7.4). The soluble protein fraction was retained and then concentrated by micro spin ultrafiltration at 14,000 rpm for 30 minutes at 4°C, and then washed by adding ultrapure water and another centrifugation step at 14,000 rpm for 20 minutes at 4°C for five cycles. 100 µg of protein was then hydrolyzed by an enzyme digest using pepsin, pronase E, aminopeptidase and prolidase.[248] 30 µL of the sample were spiked with 30 µL 0.2% (v/v) trifluoroacetic acid (TFA) in water containing the isotopic standards (5-25 pmol). Normal and isotopic standards were produced as described previously.[63,249] Samples were then analyzed by LC-MS/MS using an ACQUITY ultra-high-performance liquid chromatography system with a Xevo TQ-S LC-MS/MS spectrometer. Two 5 µm HypercarbTM columns in series were used: 2.1 x 50 mm, fitted with a 5 x 2.1 mm pre-column, and 2.1 x 250 mm. The mobile phases were 0.1% (v/v) TFA in water and 0.1% (v/v) TFA in 50% water. The column temperature was set to 30°C and the flow rate was set to 0.2 mL/minute. Elution was done by a two-step gradient and washing of the columns was performed with 0.1% (v/v) TFA in 50% tetrahydrofuran (THF).[248] Detection of advanced glycation end products, including oxidation and nitration markers, was done by electrospray positive ionization in combination with multiple reaction monitoring. Ionization temperature was set to 150°C and desolvation temperature was set to 500°C. The gas flows rates of the cone and the desolvation were 150 and 1000 L/hour, respectively. The capillary voltage was 0.5 kV. Molecular ion and fragment ion masses, cone voltage and collision energizes were optimized to ±0.1 Da and ±1 eV for multiple reaction monitoring detection. For the acquisition, proprietary MassLynx software was used and for the quantification proprietary TargetLynx software was used.

4.2.23 Streptozotocin-induced diabetic mouse model

The animal studies were approved by the authorities. Mice were handled in accordance with the regulations found in animal proposal (file number: 35-9185.81/G-103/18). Mice were housed in cages of up to 3 animals in a

temperature- and humidity-controlled environment with a 12-hour light-dark cycle with water and food ad libitum.

Wild-type (C57BL/6) and *Hspa1a* knockout mice were injected intraperitoneally with 60 µg/g streptozotocin (dissolved in 12.5 mM sodium citrate buffer with 0.7% sodium chloride, pH 7.4) daily for 1 week at the age of 10 weeks. Blood glucose was measured regularly to identify diabetic animals. At the age of 28 weeks the mice were sacrificed with CO_2 and organs were harvested. The organs were snap-frozen in liquid nitrogen or submerged in formalin for subsequent paraffin embedding or Cryo-EM until further analysis.

4.2.24 Urinary albumin measurement

Urine samples were obtained in a metabolic cage one day before sacrifice. Albumin concentration was measured using a mouse albumin ELISA (enzyme-linked immunosorbent assay) kit. Briefly, mouse urine was diluted 1:500 in dilution solution. 100 µL of albumin standard solution and samples were pipetted into the wells of the ELISA plate, followed by an incubation at room temperature for 30 minutes. Then, all wells are aspirated completely, and washed with wash solution for four times. Then, 100 µL of enzyme-antibody conjugate were added to each well, followed by an incubation at room temperature, in the dark, for 30 minutes. Then, the plate was again washed four times with wash solution. Then, 100 µL of TMB (3,3',5,5'-tetramethylbenzidine) substrate solution was added to each well, followed by an incubation at room temperature, in the dark, for 10 minutes. Then, 100 µL of stop solution were added to each well, and the absorbance was determined at 450 nm using a SPECTROstar Omega plate reader.

4.2.25 Urinary creatinine measurement

Creatinine concentration was measured with a creatinine kit on an Olympus AU400 chemistry analyzer in the lab of Prof. Dr. Jürgen Okun in the metabolic center (division of inborn errors of metabolism) of Heidelberg University Hospital.

4.2.26 Urinary electrolyte measurement

Phosphate, sodium, potassium, and chloride from mouse urine samples were measured in the central lab of Heidelberg University hospital using an ADVIA® Chemistry XPT (Siemens) analyzer, with the help of Dr. Maik Brune.

4.2.27 Murine kidney samples processed and evaluated by the CMCP

4.2.27.1 Histopathology

Organs were removed from the animals and directly placed in 10% formalin for preservation. Paraffin embedding and preparation for histological staining and imaging was performed by the Center for Model System and Comparative Pathology (CMCP) of Heidelberg University Hospital.

4.2.27.2 Antibody staining

Antigen retrieval was done in a steamer with antigen retrieval solution at 95°C for 30 minutes. Blocking was performed with peroxidase blocking solution (Dako REAL, Agilent). The primary antibody anti-HSPA1A was incubated for one hour in a 1:100 dilution at room temperature. The secondary reagent ENZO Polyview Plus AP anti-rabbit was used for detection with the Zytomed permanent AP-red kit. The primary antibody anti-WT1 was incubated for one hour in a 1:800 dilution at room temperature. The secondary reagent Enzo Polyview Plus HRP anti-rabbit was used for detection with the Zytomed permanent AP-red kit. Counterstain was done with hemalum solution (Hemalum solution acid acc. to Mayer, Carl Roth GmbH).

4.2.27.3 Acid fuchsin orange G (AFOG) staining

First, sections were deparaffinized. Then, the sections were covered with Bouin fixative for three hours at 56°C and washed with distilled water. Nuclei were stained with Weigert reagent for 10 minutes. Then, sections were submerged in Jenkins reagent for 10 seconds and subsequently washed with distilled water. Then, sections were covered with 1% phosphomolybdic acid for 5 minutes and washed with distilled water. Finally, the sections were covered in AFOG solution for 10 minutes, washed in distilled water for one minute, dehydrated and mounted.

4.2.28 Light and Electron microscopy

Mouse kidney biopsies were fixed for at least two hours at room temperature in 3% glutaraldehyde solution in 0.1 M cacodylate buffer at pH 7.4. The samples were brought to the electron microscopy lab (Institute of Pathology of Heidelberg University Hospital) for further processing. The kidneys were cut into pieces of ca. 1 mm^3. After a washing step in buffer, post-fixation was performed for one hour at 4°C in 1% aqueous osmium tetroxide. The fixed samples were then rinsed in water, followed by a dehydration in ethanol. Then they were transferred to propylene oxide solution, and

subsequently embedded in an epoxy resin (glycidether 100). Sections were of the samples were cut using an ultramicrotome (Reichert Ultracut E, Leica UC7). Then the sections were stained with toluidine blue solution. 60-80 nm ultrathin sections were overlaid with uranyl acetate and lead citrate. Afterwards, image acquisition was performed on an electron microscope (JEM 1400).

4.2.29 Fractional mesangial area measurement

The fractional mesangial area (FMA) was obtained by measuring the Bowman's capsule area (yellow outline in figure 44) and the glomerular tuft area (red outline in figure 44). The area in between was then calculated and plotted as % fractional mesangial area.
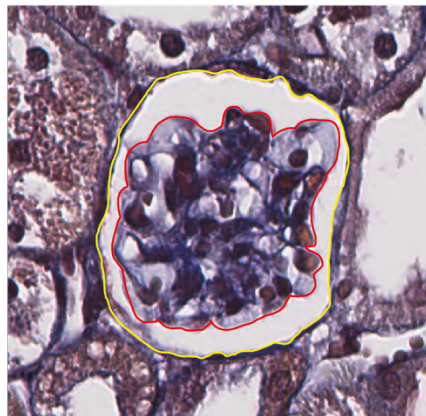

Figure 44 Measurement of the fractional mesangial area in kidney sections.

4.2.30 Statistical analyses

Experimental results from the endothelial cell lines are expressed as mean ± standard deviation from three independent biological replicates, unless otherwise stated. Experimental results from the mouse experiments are expressed as mean ± standard deviation. Statistical significance was analyzed using Welch's corrected t-test or two-way ANOVA, followed by comparing all groups using Tukey's or Sidak`s multiple comparison test. Statistical analysis of the data was performed using GraphPad Prism software and p-values < 0.05 were considered statistically significant.
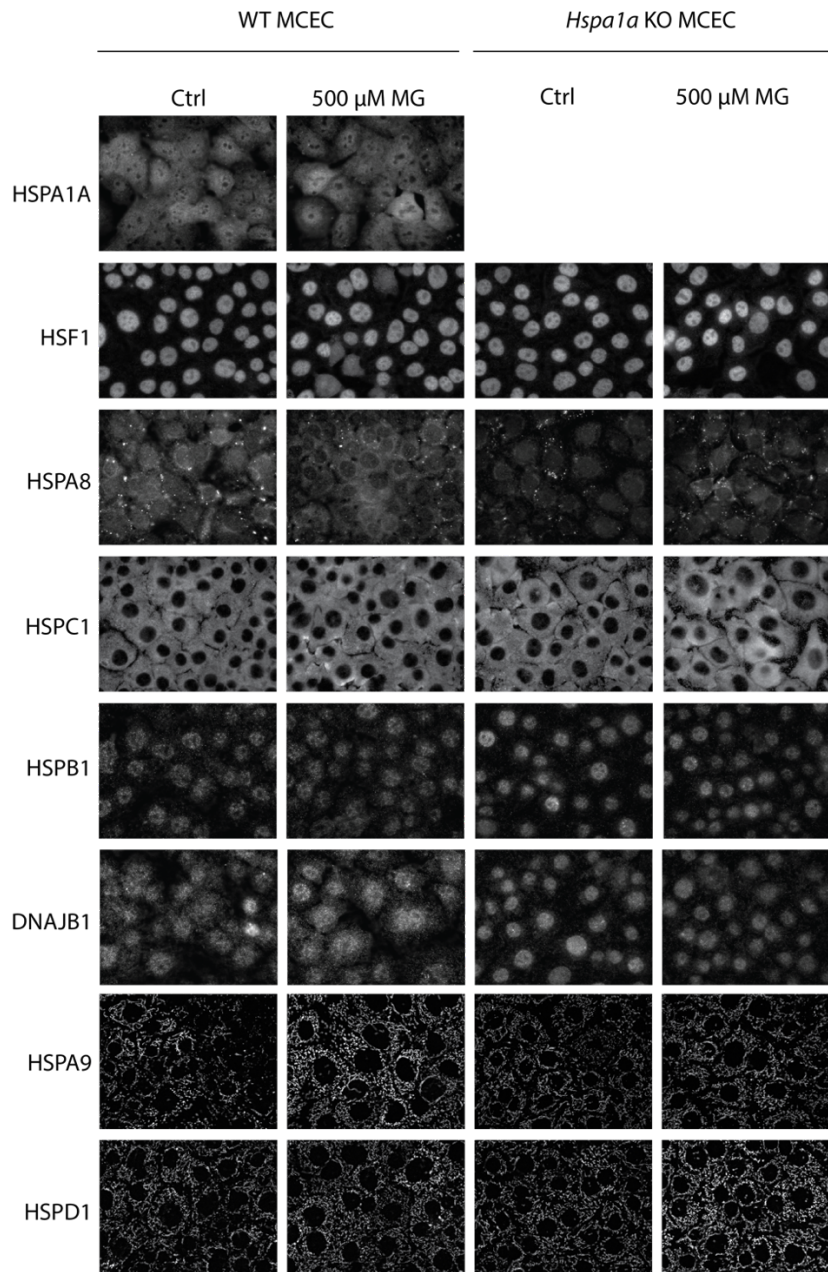
5 APPENDIX

5.1 Supplemental figures

Figure 45 Immunofluorescence analysis of the protein expression after acute methylglyoxal stress.
WT and *Hspa1a* KO MCEC were stressed with 500 μM MG for 24 hours and then stained with the respective antibodies detecting heat-shock proteins, co-chaperones, and heat-shock factor 1.
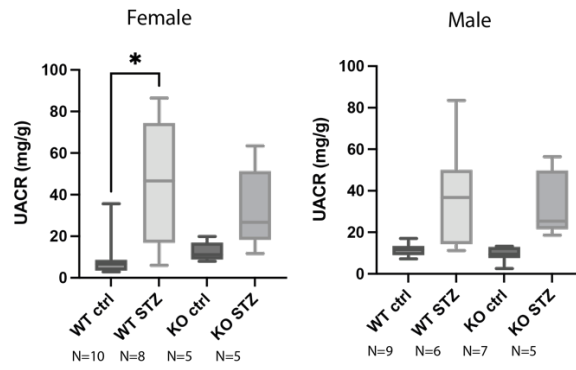
Figure 46 Urinary albumin-to-creatinine ratio in female and male mice.
Albumin measurements from mouse urine were done by Dr. Claus Rodemer. Creatinine measurements from mouse urine were done in the lab of Prof. Dr. Jürgen Okun in the metabolic center (division of inborn errors of metabolism) of Heidelberg University Hospital. Data represents mean ± SD, analyzed by a two-way ANOVA statistical test followed by comparing all groups using Sidak`s multiple comparison test. *p ≤ 0.05.

Figure 47 Fractional mesangial area of kidney glomeruli from female and male mice.
Data represents mean ± SD, analyzed by a two-way ANOVA statistical test followed by comparing all groups using Sidak`s multiple comparison test. *p ≤ 0.05, **p ≤ 0.01, ***p ≤ 0.001.

Figure 48 Glomerular basement membrane thickness of female and male mice.
Data represents mean ± SD, analyzed by a two-way ANOVA statistical test followed by comparing all groups using Sidak`s multiple comparison test. *p ≤ 0.05.

Figure 49 Podocyte number per kidney glomerulus from female and male mice.

Data represents mean ± SD, analyzed by a two-way ANOVA statistical test followed by comparing all groups using Sidak`s multiple comparison test.
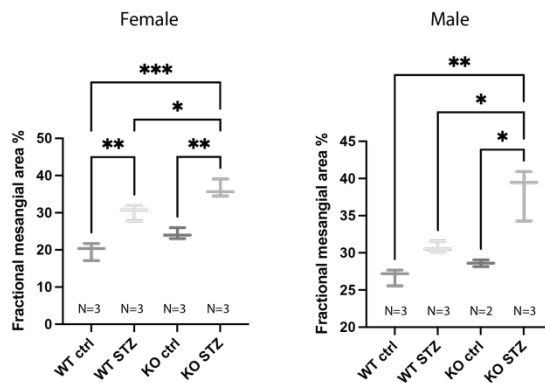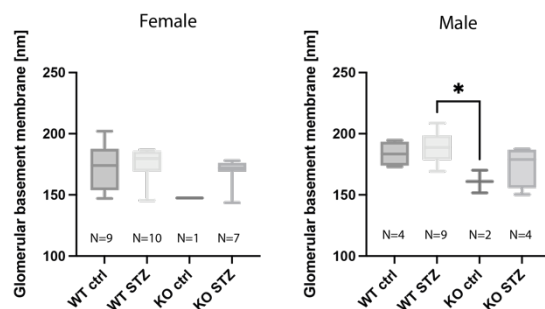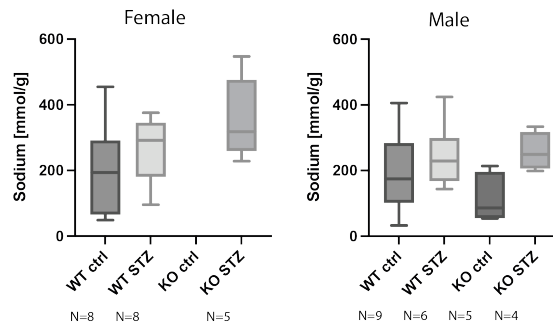

Figure 50 Urinary sodium-to-creatinine ratio in female and male mice.

Data represents mean ± SD, analyzed by a two-way ANOVA statistical test followed by comparing all groups using Sidak`s multiple comparison test.
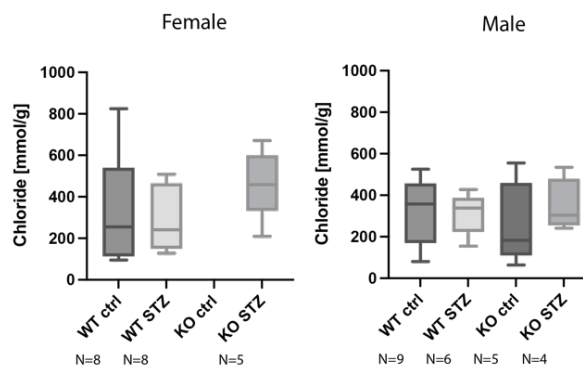
Figure 51 Urinary chloride-to-creatinine ratio in female and male mice.

Data represents mean ± SD, analyzed by a two-way ANOVA statistical test followed by comparing all groups using Sidak`s multiple comparison test.
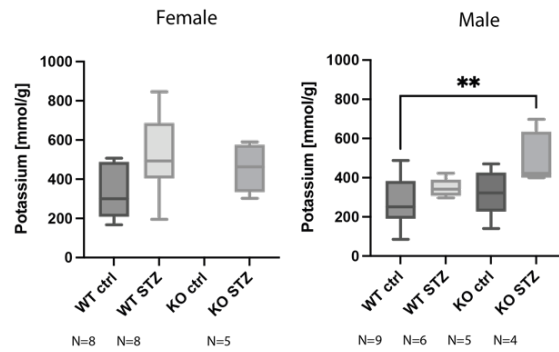
Figure 52 Urinary potassium-to-creatinine ratio in female and male mice.
Data represents mean ± SD, analyzed by a two-way ANOVA statistical test followed by comparing all groups using Sidak`s multiple comparison test. **$p \leq 0.01$.
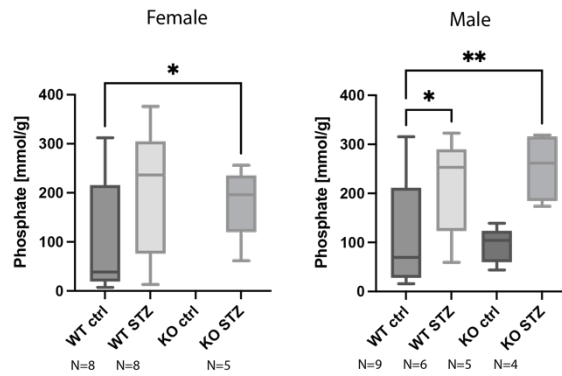
Figure 53 Urinary phosphate-to-creatinine ratio in female and male mice.
Data represents mean ± SD, analyzed by a two-way ANOVA statistical test followed by comparing all groups using Sidak`s multiple comparison test. *$p \leq 0.05$, **$p \leq 0.01$.
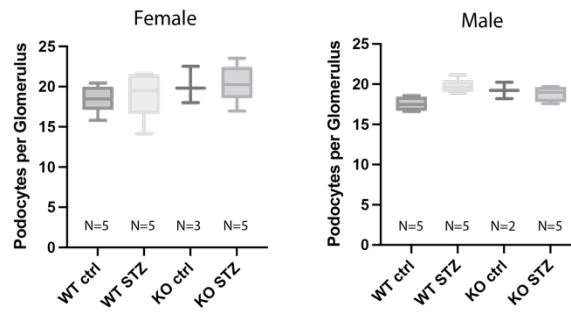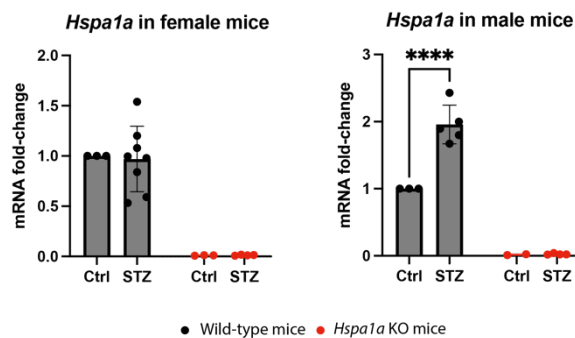

Figure 54 Analysis of *Hspa1a* mRNA expression from kidneys in female and male mice.
Data represents mean ± SD, analyzed by a two-way ANOVA statistical test followed by comparing all groups using Sidak`s multiple comparison test. ****$p \leq 0.0001$.

98
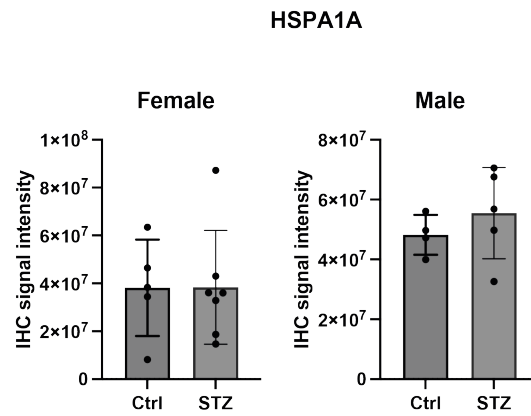
Figure 55 Immunohistochemical analysis of HSPA1A protein expression from kidney sections of female and male wild-type mice.

Data represents mean ± SD.
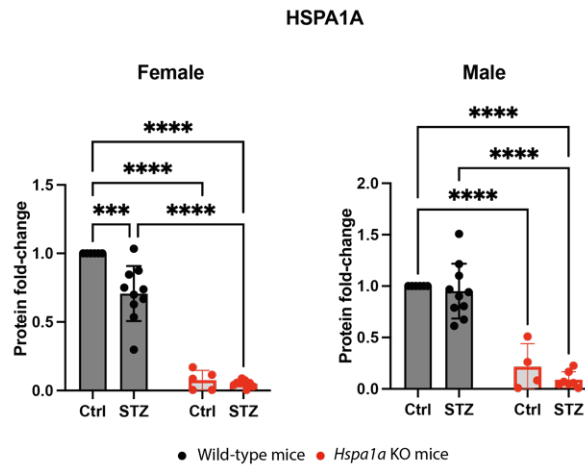
Figure 56 Analysis of HSPA1A protein expression from kidneys in female and male mice.

Data represents mean ± SD, analyzed by a two-way ANOVA statistical test followed by comparing all groups using Sidak`s multiple comparison test. ***p ≤ 0.001, ****p ≤ 0.0001.
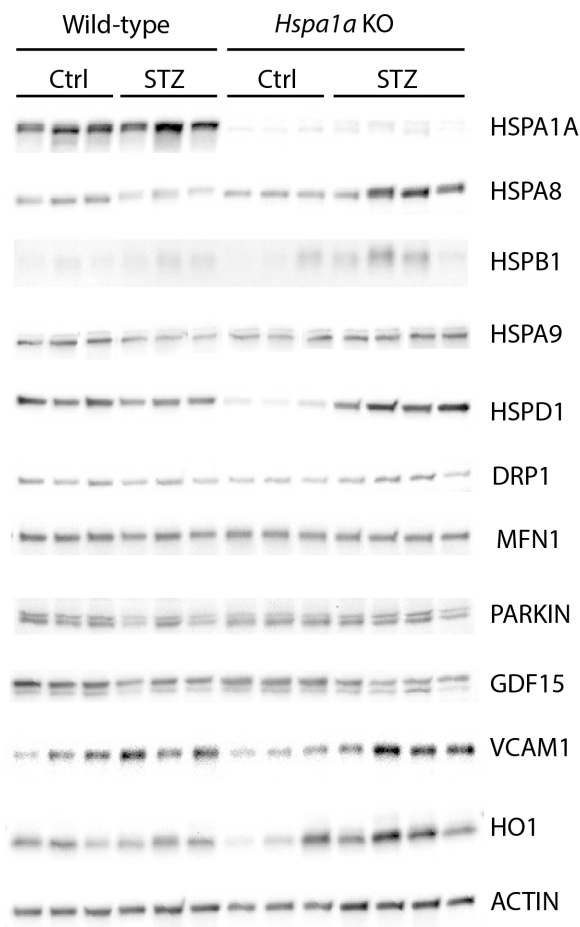
Figure 57 Western blot protein analyses from kidney protein lysates of WT and *Hspa1a* KO control and diabetic animals.

HSPA9 and VCAM1 blot were prepared by Dr. Claus Rodemer. ACTIN was used as a loading control.
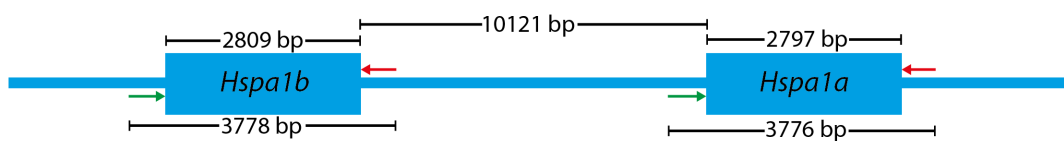
Figure 58 Schematic overview of the PCR amplified regions to determine the genotype of MCEC and C57BL/6 mice.

The green arrows represent the forward primer binding site approximately 500 base pairs ahead of the gene. The red arrows represent the reverse primer binding site approximately 500 base pairs after the gene.

6 REFERENCES

1.   IDF Diabetes Atlas 2021. https://diabetesatlas.org/atlas/tenth-edition/.

2.   American Diabetes Association. Diagnosis and Classification of Diabetes Mellitus. *Diabetes Care* **32**, S62–S67 (2009).

3.   American Diabetes Association. https://www.diabetes.org/diabetes/a1c/diagnosis (2022).

4.   Atkinson, M. A. *et al.* How does type 1 diabetes develop?: the notion of homicide or β-cell suicide revisited. *Diabetes* **60**, 1370–1379 (2011).

5.   Winter, W. E. & Pittman, D. The clinical application of islet autoantibody testing for the diagnosis of autoimmune diabetes. *MLO Med Lab Obs* **45**, 16, 20, 22 passim (2013).

6.   Baekkeskov, S. *et al.* Identification of the 64K autoantigen in insulin-dependent diabetes as the GABA-synthesizing enzyme glutamic acid decarboxylase. *Nature* **347**, 151–156 (1990).

7.   American Diabetes Association. Standards of Medical Care in Diabetes—2013. *Diabetes Care* **36**, S11–S66 (2013).

8.   Ross, G. Gestational diabetes. *Aust Fam Physician* **35**, 392–396 (2006).

9.   Ahlqvist, E. *et al.* Novel subgroups of adult-onset diabetes and their association with outcomes: a data-driven cluster analysis of six variables. *The Lancet Diabetes & Endocrinology* **6**, 361–369 (2018).

10.   Stern, S. E. *et al.* Identification of individuals with insulin resistance using routine clinical measurements. *Diabetes* **54**, 333–339 (2005).

11.   Matthews, D. R. *et al.* Homeostasis model assessment: insulin resistance and beta-cell function from fasting plasma glucose and insulin concentrations in man. *Diabetologia* **28**, 412–419 (1985).

12.   Turner, R. C., Holman, R. R., Matthews, D., Hockaday, T. D. & Peto, J. Insulin deficiency and insulin resistance interaction in diabetes: estimation of their relative contribution by feedback analysis from basal plasma insulin and glucose concentrations. *Metabolism* **28**, 1086–1096 (1979).

13.   Zaharia, O. P. *et al.* Risk of diabetes-associated diseases in subgroups of patients with recent-onset diabetes: a 5-year follow-up study. *Lancet Diabetes Endocrinol* **7**, 684–694 (2019).

14. Wagner, R. *et al.* Pathophysiology-based subphenotyping of individuals at elevated risk for type 2 diabetes. *Nat Med* **27**, 49–57 (2021).

15. Viigimaa, M. *et al.* Macrovascular Complications of Type 2 Diabetes Mellitus. *Curr Vasc Pharmacol* **18**, 110–116 (2020).

16. Fong, D. S., Aiello, L. P., Ferris, F. L. & Klein, R. Diabetic retinopathy. *Diabetes Care* **27**, 2540–2553 (2004).

17. Vinik, A. I., Nevoret, M.-L., Casellini, C. & Parson, H. Diabetic neuropathy. *Endocrinol Metab Clin North Am* **42**, 747–787 (2013).

18. Selby, N. M. & Taal, M. W. An updated overview of diabetic nephropathy: Diagnosis, prognosis, treatment goals and latest guidelines. *Diabetes Obes Metab* **22 Suppl 1**, 3–15 (2020).

19. Younossi, Z. M. *et al.* The global epidemiology of NAFLD and NASH in patients with type 2 diabetes: A systematic review and meta-analysis. *J Hepatol* **71**, 793–801 (2019).

20. Kopf, S. *et al.* Diabetic Pneumopathy-A New Diabetes-Associated Complication: Mechanisms, Consequences and Treatment Considerations. *Front Endocrinol (Lausanne)* **12**, 765201 (2021).

21. Nikkilä, E. A. Plasma triglycerides in human diabetes. *Proc R Soc Med* **67**, 662–665 (1974).

22. Virmani, R. *et al.* Atherosclerotic Plaque Progression and Vulnerability to Rupture: Angiogenesis as a Source of Intraplaque Hemorrhage. *ATVB* **25**, 2054–2061 (2005).

23. Madonna, R., Balistreri, C. R., Geng, Y.-J. & De Caterina, R. Diabetic microangiopathy: Pathogenetic insights and novel therapeutic approaches. *Vascul Pharmacol* **90**, 1–7 (2017).

24. Girach, A., Manner, D. & Porta, M. Diabetic microvascular complications: can patients at risk be identified? A review: DIABETIC MICROVASCULAR COMPLICATIONS. *International Journal of Clinical Practice* **60**, 1471–1483 (2006).

25. Brownlee, M. Biochemistry and molecular cell biology of diabetic complications. *Nature* **414**, 813–820 (2001).

26. Umanath, K. & Lewis, J. B. Update on Diabetic Nephropathy: Core Curriculum 2018. *Am J Kidney Dis* **71**, 884–895 (2018).

27. *Pathophysiology: the biologic basis for disease in adults and children.* (Elsevier, 2019).

28.   Eshbach, M. L. & Weisz, O. A. Receptor-Mediated Endocytosis in the Proximal Tubule. *Annu Rev Physiol* **79**, 425–448 (2017).

29.   *Pathophysiology: clinical concepts of disease processes.* (Mosby-Year Book, 1992).

30.   https://commons.wikimedia.org/wiki/File:Renal_corpuscle-en.svg#metadata.

31.   Tervaert, T. W. C. *et al.* Pathologic classification of diabetic nephropathy. *J Am Soc Nephrol* **21**, 556–563 (2010).

32.   *Klinisches Wörterbuch.* (Walter de Gruyter GmbH, 2014).

33.   Klahr, S., Schreiner, G. & Ichikawa, I. The progression of renal disease. *N Engl J Med* **318**, 1657–1666 (1988).

34.   Mauer, S. M., Sutherland, D. E. & Steffes, M. W. Relationship of systemic blood pressure to nephropathology in insulin-dependent diabetes mellitus. *Kidney Int* **41**, 736–740 (1992).

35.   Stevens, P. E., Levin, A., & Kidney Disease: Improving Global Outcomes Chronic Kidney Disease Guideline Development Work Group Members. Evaluation and management of chronic kidney disease: synopsis of the kidney disease: improving global outcomes 2012 clinical practice guideline. *Ann Intern Med* **158**, 825–830 (2013).

36.   Nguyen, T. Q. *et al.* Urinary Connective Tissue Growth Factor Excretion Correlates With Clinical Markers of Renal Disease in a Large Population of Type 1 Diabetic Patients With Diabetic Nephropathy. *Diabetes Care* **29**, 83–88 (2006).

37.   Yonemoto, S. *et al.* Correlations of tissue macrophages and cytoskeletal protein expression with renal fibrosis in patients with diabetes mellitus. *Clin Exp Nephrol* **10**, 186–192 (2006).

38.   Najafian, B., Kim, Y., Crosson, J. T. & Mauer, M. Atubular glomeruli and glomerulotubular junction abnormalities in diabetic nephropathy. *J Am Soc Nephrol* **14**, 908–917 (2003).

39.   Tracy, R. E. *et al.* Renovasculopathies of nephrosclerosis in relation to atherosclerosis at ages 25 to 54 years. *Kidney Int* **49**, 564–570 (1996).

40.   Basta, G., Schmidt, A. M. & De Caterina, R. Advanced glycation end products and vascular inflammation: implications for accelerated atherosclerosis in diabetes. *Cardiovasc Res* **63**, 582–592 (2004).

41.   Madiraju, A. K. *et al.* Metformin suppresses gluconeogenesis by inhibiting mitochondrial glycerophosphate dehydrogenase. *Nature* **510**, 542–546 (2014).

42.   Natali, A. & Ferrannini, E. Effects of metformin and thiazolidinediones on suppression of hepatic glucose production and stimulation of glucose uptake in type 2 diabetes: a systematic review. *Diabetologia* **49**, 434–441 (2006).

43.   Hummel, C. S. *et al.* Glucose transport by human renal Na+/D-glucose cotransporters SGLT1 and SGLT2. *Am J Physiol Cell Physiol* **300**, C14-21 (2011).

44.   Haas, B., Eckstein, N., Pfeifer, V., Mayer, P. & Hass, M. D. S. Efficacy, safety and regulatory status of SGLT2 inhibitors: focus on canagliflozin. *Nutr Diabetes* **4**, e143 (2014).

45.   Vasilakou, D. *et al.* Sodium-glucose cotransporter 2 inhibitors for type 2 diabetes: a systematic review and meta-analysis. *Ann Intern Med* **159**, 262–274 (2013).

46.   DeFronzo, R. A., Reeves, W. B. & Awad, A. S. Pathophysiology of diabetic kidney disease: impact of SGLT2 inhibitors. *Nat Rev Nephrol* **17**, 319–334 (2021).

47.   Palmer, S. C. *et al.* Sodium-glucose cotransporter protein-2 (SGLT-2) inhibitors and glucagon-like peptide-1 (GLP-1) receptor agonists for type 2 diabetes: systematic review and network meta-analysis of randomised controlled trials. *BMJ* **372**, m4573 (2021).

48.   Cherney, D. Z. I. *et al.* Pooled analysis of Phase III trials indicate contrasting influences of renal function on blood pressure, body weight, and HbA1c reductions with empagliflozin. *Kidney International* **93**, 231–244 (2018).

49.   Schirra, J. *et al.* Exendin(9-39)amide is an antagonist of glucagon-like peptide-1(7-36)amide in humans. *J Clin Invest* **101**, 1421–1430 (1998).

50.   Gerstein, H. C. *et al.* Dulaglutide and renal outcomes in type 2 diabetes: an exploratory analysis of the REWIND randomised, placebo-controlled trial. *Lancet* **394**, 131–138 (2019).

51.   Marso, S. P. *et al.* Liraglutide and Cardiovascular Outcomes in Type 2 Diabetes. *N Engl J Med* **375**, 311–322 (2016).

52.   Hendarto, H. *et al.* GLP-1 analog liraglutide protects against oxidative stress and albuminuria in streptozotocin-induced diabetic rats via protein kinase A-mediated inhibition of renal NAD(P)H oxidases. *Metabolism* **61**, 1422–1434 (2012).

53.   Ninčević, V. *et al.* Renal Benefits of SGLT 2 Inhibitors and GLP-1 Receptor Agonists: Evidence Supporting a Paradigm Shift in the Medical Management of Type 2 Diabetes. *Int J Mol Sci* **20**, E5831 (2019).

54.   Yin, W. *et al.* Recombinant human GLP-1(rhGLP-1) alleviating renal

tubulointestitial injury in diabetic STZ-induced rats. *Biochem Biophys Res Commun* **495**, 793–800 (2018).

55. Goldin, A., Beckman, J. A., Schmidt, A. M. & Creager, M. A. Advanced Glycation End Products: Sparking the Development of Diabetic Vascular Injury. *Circulation* **114**, 597–605 (2006).

56. Schneider, M. *et al.* Determination of glycated nucleobases in human urine by a new monoclonal antibody specific for N2-carboxyethyl-2'-deoxyguanosine. *Chem Res Toxicol* **17**, 1385–1390 (2004).

57. Genuth, S. *et al.* Glycation and carboxymethyllysine levels in skin collagen predict the risk of future 10-year progression of diabetic retinopathy and nephropathy in the diabetes control and complications trial and epidemiology of diabetes interventions and complications participants with type 1 diabetes. *Diabetes* **54**, 3103–3111 (2005).

58. Henning, C. & Glomb, M. A. Pathways of the Maillard reaction under physiological conditions. *Glycoconj J* **33**, 499–512 (2016).

59. Vistoli, G. *et al.* Advanced glycoxidation and lipoxidation end products (AGEs and ALEs): an overview of their mechanisms of formation. *Free Radic Res* **47 Suppl 1**, 3–27 (2013).

60. Dunn, J. A. *et al.* Reaction of ascorbate with lysine and protein under autoxidizing conditions: formation of N epsilon-(carboxymethyl)lysine by reaction between lysine and products of autoxidation of ascorbate. *Biochemistry* **29**, 10964–10970 (1990).

61. Fu, M. X. *et al.* The advanced glycation end product, Nepsilon-(carboxymethyl)lysine, is a product of both lipid peroxidation and glycoxidation reactions. *J Biol Chem* **271**, 9982–9986 (1996).

62. Lo, T. W., Westwood, M. E., McLellan, A. C., Selwood, T. & Thornalley, P. J. Binding and modification of proteins by methylglyoxal under physiological conditions. A kinetic and mechanistic study with N alpha-acetylarginine, N alpha-acetylcysteine, and N alpha-acetyllysine, and bovine serum albumin. *J Biol Chem* **269**, 32299–32305 (1994).

63. Thornalley, P. J. *et al.* Quantitative screening of advanced glycation endproducts in cellular and extracellular proteins by tandem mass spectrometry. *Biochem J* **375**, 581–592 (2003).

64. Schmidt, R., Böhme, D., Singer, D. & Frolov, A. Specific tandem mass

spectrometric detection of AGE-modified arginine residues in peptides. *J Mass Spectrom* **50**, 613–624 (2015).

65.   Brings, S. *et al.* Dicarbonyls and Advanced Glycation End-Products in the Development of Diabetic Complications and Targets for Intervention. *IJMS* **18**, 984 (2017).

66.   Thornalley, P. J., Yurek-George, A. & Argirov, O. K. Kinetics and mechanism of the reaction of aminoguanidine with the alpha-oxoaldehydes glyoxal, methylglyoxal, and 3-deoxyglucosone under physiological conditions. *Biochem Pharmacol* **60**, 55–65 (2000).

67.   Phillips, S. A. & Thornalley, P. J. The formation of methylglyoxal from triose phosphates. Investigation using a specific assay for methylglyoxal. *Eur J Biochem* **212**, 101–105 (1993).

68.   Maillard, L. C. Action Des Acides Aminés Sur Les Sucres; Formation Des Mélanoïdines Par Voie Méthodique. *C. R. Acad. Sci.* 66–68 (1912).

69.   Ahmed, N., Dobler, D., Dean, M. & Thornalley, P. J. Peptide mapping identifies hotspot site of modification in human serum albumin by methylglyoxal involved in ligand binding and esterase activity. *J Biol Chem* **280**, 5724–5732 (2005).

70.   Shipanova, I. N., Glomb, M. A. & Nagaraj, R. H. Protein modification by methylglyoxal: chemical nature and synthetic mechanism of a major fluorescent adduct. *Arch Biochem Biophys* **344**, 29–36 (1997).

71.   van Eupen, M. G. A. *et al.* The methylglyoxal-derived AGE tetrahydropyrimidine is increased in plasma of individuals with type 1 diabetes mellitus and in atherosclerotic lesions and is associated with sVCAM-1. *Diabetologia* **56**, 1845–1855 (2013).

72.   Thornalley, P. J. The glyoxalase system in health and disease. *Mol Aspects Med* **14**, 287–371 (1993).

73.   Abordo, E. A., Minhas, H. S. & Thornalley, P. J. Accumulation of α-oxoaldehydes during oxidative stress: a role in cytotoxicity. *Biochemical Pharmacology* **58**, 641–648 (1999).

74.   Alfarouk, K. O. *et al.* The possible role of methylglyoxal metabolism in cancer. *Journal of Enzyme Inhibition and Medicinal Chemistry* **36**, 2010–2015 (2021).

75.   Ishibashi, Y. *et al.* Methylglyoxal-derived hydroimidazolone-1 evokes inflammatory reactions in endothelial cells via an interaction with receptor for advanced glycation end products. *Diab Vasc Dis Res* **14**, 450–453 (2017).

76.   Schmidt, A. M. *et al.* Receptor for advanced glycation end products (AGEs) has a central role in vessel wall interactions and gene activation in response to circulating AGE proteins. *Proc Natl Acad Sci U S A* **91**, 8807–8811 (1994).

77.   Bierhaus, A. *et al.* Advanced glycation end product (AGE)-mediated induction of tissue factor in cultured endothelial cells is dependent on RAGE. *Circulation* **96**, 2262–2271 (1997).

78.   Neumann, A., Schinzel, R., Palm, D., Riederer, P. & Münch, G. High molecular weight hyaluronic acid inhibits advanced glycation endproduct-induced NF-kappaB activation and cytokine expression. *FEBS Lett* **453**, 283–287 (1999).

79.   Li, J. & Schmidt, A. M. Characterization and functional analysis of the promoter of RAGE, the receptor for advanced glycation end products. *J Biol Chem* **272**, 16498–16506 (1997).

80.   de Hemptinne, V., Rondas, D., Toepoel, M. & Vancompernolle, K. Phosphorylation on Thr-106 and NO-modification of glyoxalase I suppress the TNF-induced transcriptional activity of NF-kappaB. *Mol Cell Biochem* **325**, 169–178 (2009).

81.   Tanaka, S., Avigad, G., Brodsky, B. & Eikenberry, E. F. Glycation induces expansion of the molecular packing of collagen. *J Mol Biol* **203**, 495–505 (1988).

82.   Hammes, H. P. *et al.* Modification of vitronectin by advanced glycation alters functional properties in vitro and in the diabetic retina. *Lab Invest* **75**, 325–338 (1996).

83.   Howard, E. W., Benton, R., Ahern-Moore, J. & Tomasek, J. J. Cellular contraction of collagen lattices is inhibited by nonenzymatic glycation. *Exp Cell Res* **228**, 132–137 (1996).

84.   Haitoglou, C. S., Tsilibary, E. C., Brownlee, M. & Charonis, A. S. Altered cellular interactions between endothelial cells and nonenzymatically glucosylated laminin/type IV collagen. *J Biol Chem* **267**, 12404–12407 (1992).

85.   Klöpfer, A., Spanneberg, R. & Glomb, M. A. Formation of arginine modifications in a model system of Nα-tert-butoxycarbonyl (Boc)-arginine with methylglyoxal. *J Agric Food Chem* **59**, 394–401 (2011).

86.   Ahmed, N., Argirov, O. K., Minhas, H. S., Cordeiro, C. A. A. & Thornalley, P. J. Assay of advanced glycation endproducts (AGEs): surveying AGEs by chromatographic assay with derivatization by 6-aminoquinolyl-N-hydroxysuccinimidyl-carbamate and application to Nepsilon-carboxymethyl-lysine- and Nepsilon-(1-carboxyethyl)lysine-modified albumin. *Biochem J* **364**, 1–14 (2002).

87.   Biemel, K. M., Friedl, D. A. & Lederer, M. O. Identification and quantification

of major maillard cross-links in human serum albumin and lens protein. Evidence for glucosepane as the dominant compound. *J Biol Chem* **277**, 24907–24915 (2002).

88.   Angeloni, C., Zambonin, L. & Hrelia, S. Role of methylglyoxal in Alzheimer's disease. *Biomed Res Int* **2014**, 238485 (2014).

89.   Hipkiss, A. R. On the Relationship between Energy Metabolism, Proteostasis, Aging and Parkinson's Disease: Possible Causative Role of Methylglyoxal and Alleviative Potential of Carnosine. *Aging Dis* **8**, 334–345 (2017).

90.   Knani, I. *et al.* Methylglyoxal: A Relevant Marker of Disease Activity in Patients with Rheumatoid Arthritis. *Dis Markers* **2018**, 8735926 (2018).

91.   Rabbani, N. & Thornalley, P. J. Hexokinase-2 Glycolytic Overload in Diabetes and Ischemia-Reperfusion Injury. *Trends Endocrinol Metab* **30**, 419–431 (2019).

92.   Han, Y. *et al.* Plasma methylglyoxal and glyoxal are elevated and related to early membrane alteration in young, complication-free patients with Type 1 diabetes. *Mol Cell Biochem* **305**, 123–131 (2007).

93.   Lapolla, A. *et al.* Glyoxal and methylglyoxal levels in diabetic patients: quantitative determination by a new GC/MS method. *Clin Chem Lab Med* **41**, 1166–1173 (2003).

94.   Scheijen, J. L. J. M. & Schalkwijk, C. G. Quantification of glyoxal, methylglyoxal and 3-deoxyglucosone in blood and plasma by ultra performance liquid chromatography tandem mass spectrometry: evaluation of blood specimen. *Clin Chem Lab Med* **52**, 85–91 (2014).

95.   Ahmed, N. *et al.* Methylglyoxal-derived hydroimidazolone advanced glycation end-products of human lens proteins. *Invest Ophthalmol Vis Sci* **44**, 5287–5292 (2003).

96.   Fosmark, D. S. *et al.* Increased serum levels of the specific advanced glycation end product methylglyoxal-derived hydroimidazolone are associated with retinopathy in patients with type 2 diabetes mellitus. *Metabolism* **55**, 232–236 (2006).

97.   Odani, H. *et al.* Imidazolium crosslinks derived from reaction of lysine with glyoxal and methylglyoxal are increased in serum proteins of uremic patients: evidence for increased oxidative stress in uremia. *FEBS Lett* **427**, 381–385 (1998).

98.   Wendt, T. M. *et al.* RAGE drives the development of glomerulosclerosis and implicates podocyte activation in the pathogenesis of diabetic nephropathy. *Am J Pathol* **162**, 1123–1137 (2003).

99.   Huang, K.-P. *et al.* AGEs-RAGE system down-regulates Sirt1 through the

ubiquitin-proteasome pathway to promote FN and TGF-β1 expression in male rat glomerular mesangial cells. *Endocrinology* **156**, 268–279 (2015).

100.   Kumar Pasupulati, A., Chitra, P. S. & Reddy, G. B. Advanced glycation end products mediated cellular and molecular events in the pathology of diabetic nephropathy. *Biomol Concepts* **7**, 293–309 (2016).

101.   Serban, A. I. *et al.* Extracellular matrix is modulated in advanced glycation end products milieu via a RAGE receptor dependent pathway boosted by transforming growth factor-β1 RAGE. *J Diabetes* **7**, 114–124 (2015).

102.   Beisswenger, P. J. *et al.* Early progression of diabetic nephropathy correlates with methylglyoxal-derived advanced glycation end products. *Diabetes Care* **36**, 3234–3239 (2013).

103.   Ha, T.-S. High-glucose and advanced glycosylation end products increased podocyte permeability via PI3-K/Akt signaling. *J Mol Med (Berl)* **88**, 391–400 (2010).

104.   Fredrickson, E. K., Rosenbaum, J. C., Locke, M. N., Milac, T. I. & Gardner, R. G. Exposed hydrophobicity is a key determinant of nuclear quality control degradation. *Mol Biol Cell* **22**, 2384–2395 (2011).

105.   Meuzelaar, H., Vreede, J. & Woutersen, S. Influence of Glu/Arg, Asp/Arg, and Glu/Lys Salt Bridges on α-Helical Stability and Folding Kinetics. *Biophys J* **110**, 2328–2341 (2016).

106.   Polykretis, P., Luchinat, E., Boscaro, F. & Banci, L. Methylglyoxal interaction with superoxide dismutase 1. *Redox Biol* **30**, 101421 (2020).

107.   Banerjee, S. Methylglyoxal modification reduces the sensitivity of hen egg white lysozyme to stress-induced aggregation: Insight into the anti-amyloidogenic property of α-dicarbonyl compound. *J Biomol Struct Dyn* **38**, 5474–5487 (2020).

108.   Gomes, R. A. *et al.* Yeast protein glycation *in vivo* by methylglyoxal: Molecular modification of glycolytic enzymes and heat shock proteins. *FEBS Journal* **273**, 5273–5287 (2006).

109.   Willis, M. S. & Patterson, C. Protein quality control, the ubiquitin proteasome system, and autophagy: when worlds collide. [Corrected]. *J Mol Cell Cardiol* **71**, 1–2 (2014).

110.   Frydman, J. Folding of newly translated proteins in vivo: the role of molecular chaperones. *Annu Rev Biochem* **70**, 603–647 (2001).

111.   Li, K. *et al.* Tetrameric Assembly of K+ Channels Requires ER-Located Chaperone Proteins. *Mol Cell* **65**, 52–65 (2017).

112.   Kang, P. J. *et al.* Requirement for hsp70 in the mitochondrial matrix for translocation and folding of precursor proteins. *Nature* **348**, 137–143 (1990).

113.   Hageman, J. *et al.* A DNAJB chaperone subfamily with HDAC-dependent activities suppresses toxic protein aggregation. *Mol Cell* **37**, 355–369 (2010).

114.   Glover, J. R. & Lindquist, S. Hsp104, Hsp70, and Hsp40: a novel chaperone system that rescues previously aggregated proteins. *Cell* **94**, 73–82 (1998).

115.   Minoia, M. *et al.* BAG3 induces the sequestration of proteasomal clients into cytoplasmic puncta: implications for a proteasome-to-autophagy switch. *Autophagy* **10**, 1603–1621 (2014).

116.   Meacham, G. C., Patterson, C., Zhang, W., Younger, J. M. & Cyr, D. M. The Hsc70 co-chaperone CHIP targets immature CFTR for proteasomal degradation. *Nat Cell Biol* **3**, 100–105 (2001).

117.   Ritossa, F. A new puffing pattern induced by temperature shock and DNP in drosophila. *Experientia* **18**, 571–573 (1962).

118.   Matz, J. M., Blake, M. J., Tatelman, H. M., Lavoi, K. P. & Holbrook, N. J. Characterization and regulation of cold-induced heat shock protein expression in mouse brown adipose tissue. *Am J Physiol* **269**, R38-47 (1995).

119.   Maytin, E. V. Differential effects of heat shock and UVB light upon stress protein expression in epidermal keratinocytes. *Journal of Biological Chemistry* **267**, 23189–23196 (1992).

120.   Morimoto, R. I. The heat shock response: systems biology of proteotoxic stress in aging and disease. *Cold Spring Harb Symp Quant Biol* **76**, 91–99 (2011).

121.   Garbe, T. R. Heat shock proteins and infection: Interactions of pathogen and host. *Experientia* **48**, 635–639 (1992).

122.   Morimoto, R. I., Kroeger, P. E. & Cotto, J. J. The Transcriptional regulation of heat shock genes: A plethora of heat shock factors and regulatory conditions. in *Stress-Inducible Cellular Responses* (eds. Feige, U., Yahara, I., Morimoto, R. I. & Polla, B. S.) 139–163 (Birkhäuser Basel, 1996). doi:10.1007/978-3-0348-9088-5_10.

123.   Wu, C. Heat Shock Transcription Factors: Structure and Regulation. *Annu. Rev. Cell Dev. Biol.* **11**, 441–469 (1995).

124.   Perisic, O., Xiao, H. & Lis, J. T. Stable binding of Drosophila heat shock factor to head-to-head and tail-to-tail repeats of a conserved 5 bp recognition unit. *Cell* **59**, 797–806 (1989).

125.   Xiao, H., Perisic, O. & Lis, J. T. Cooperative binding of drosophila heat shock

factor to arrays of a conserved 5 bp unit. *Cell* **64**, 585–593 (1991).

126. Tavaria, M., Gabriele, T., Kola, I. & Anderson, R. L. A hitchhiker's guide to the human Hsp70 family. *Cell Stress Chaperones* **1**, 23–28 (1996).

127. Milner, C. M. & Campbell, R. D. Structure and expression of the three MHC-linked HSP70 genes. *Immunogenetics* **32**, 242–251 (1990).

128. Ting, J. & Lee, A. S. Human gene encoding the 78,000-dalton glucose-regulated protein and its pseudogene: structure, conservation, and regulation. *DNA* **7**, 275–286 (1988).

129. Tavaria, M. *et al.* Localization of the gene encoding the human heat shock cognate protein, HSP73, to chromosome 11. *Genomics* **29**, 266–268 (1995).

130. Domanico, S. Z., DeNagel, D. C., Dahlseid, J. N., Green, J. M. & Pierce, S. K. Cloning of the gene encoding peptide-binding protein 74 shows that it is a new member of the heat shock protein 70 family. *Mol Cell Biol* **13**, 3598–3610 (1993).

131. Flaherty, K. M., DeLuca-Flaherty, C. & McKay, D. B. Three-dimensional structure of the ATPase fragment of a 70K heat-shock cognate protein. *Nature* **346**, 623–628 (1990).

132. Morshauser, R. C., Wang, H., Flynn, G. C. & Zuiderweg, E. R. The peptide-binding domain of the chaperone protein Hsc70 has an unusual secondary structure topology. *Biochemistry* **34**, 6261–6266 (1995).

133. Kityk, R., Vogel, M., Schlecht, R., Bukau, B. & Mayer, M. P. Pathways of allosteric regulation in Hsp70 chaperones. *Nat Commun* **6**, 8308 (2015).

134. Abrams, J. L., Verghese, J., Gibney, P. A. & Morano, K. A. Hierarchical functional specificity of cytosolic heat shock protein 70 (Hsp70) nucleotide exchange factors in yeast. *J Biol Chem* **289**, 13155–13167 (2014).

135. Bracher, A. & Verghese, J. The nucleotide exchange factors of Hsp70 molecular chaperones. *Front Mol Biosci* **2**, 10 (2015).

136. Levy-Rimler, G. *et al.* The effect of nucleotides and mitochondrial chaperonin 10 on the structure and chaperone activity of mitochondrial chaperonin 60. *Eur J Biochem* **268**, 3465–3472 (2001).

137. Ehrnsperger, M., Gräber, S., Gaestel, M. & Buchner, J. Binding of non-native protein to Hsp25 during heat shock creates a reservoir of folding intermediates for reactivation. *EMBO J* **16**, 221–229 (1997).

138. Rogalla, T. *et al.* Regulation of Hsp27 oligomerization, chaperone function, and protective activity against oxidative stress/tumor necrosis factor alpha by

phosphorylation. *J Biol Chem* **274**, 18947–18956 (1999).

139.   Rauch, J. N. & Gestwicki, J. E. Binding of human nucleotide exchange factors to heat shock protein 70 (Hsp70) generates functionally distinct complexes in vitro. *J Biol Chem* **289**, 1402–1414 (2014).

140.   Cheng, M. Y. *et al.* Mitochondrial heat-shock protein hsp60 is essential for assembly of proteins imported into yeast mitochondria. *Nature* **337**, 620–625 (1989).

141.   Mayer, M. P. & Bukau, B. Hsp70 chaperones: cellular functions and molecular mechanism. *Cell Mol Life Sci* **62**, 670–684 (2005).

142.   Ng, D. T., Watowich, S. S. & Lamb, R. A. Analysis in vivo of GRP78-BiP/substrate interactions and their role in induction of the GRP78-BiP gene. *Mol Biol Cell* **3**, 143–155 (1992).

143.   Slutsky-Leiderman, O. *et al.* The Interplay between Components of the Mitochondrial Protein Translocation Motor Studied Using Purified Components. *Journal of Biological Chemistry* **282**, 33935–33942 (2007).

144.   Wiech, H., Buchner, J., Zimmermann, R. & Jakob, U. Hsp90 chaperones protein folding in vitro. *Nature* **358**, 169–170 (1992).

145.   Walls, K. C. *et al.* Swedish Alzheimer mutation induces mitochondrial dysfunction mediated by HSP60 mislocalization of amyloid precursor protein (APP) and beta-amyloid. *J Biol Chem* **287**, 30317–30327 (2012).

146.   Lianos, G. D. *et al.* The role of heat shock proteins in cancer. *Cancer Letters* **360**, 114–118 (2015).

147.   Qi, Z. *et al.* Phosphorylation of heat shock protein 27 antagonizes TNF-α induced HeLa cell apoptosis via regulating TAK1 ubiquitination and activation of p38 and ERK signaling. *Cell Signal* **26**, 1616–1625 (2014).

148.   Dunlop, M. E. & Muggli, E. E. Small heat shock protein alteration provides a mechanism to reduce mesangial cell contractility in diabetes and oxidative stress. *Kidney Int* **57**, 464–475 (2000).

149.   Joussen, A. M. *et al.* In vivo retinal gene expression in early diabetes. *Invest Ophthalmol Vis Sci* **42**, 3047–3057 (2001).

150.   Barutta, F. *et al.* Heat shock protein expression in diabetic nephropathy. *Am J Physiol Renal Physiol* **295**, F1817-1824 (2008).

151.   Gong, D. *et al.* Quantitative proteomic profiling identifies new renal targets of copper(II)-selective chelation in the reversal of diabetic nephropathy in rats. *Proteomics* **9**, 4309–4320 (2009).

152.   Chen, S.-C. *et al.* Advanced glycation end-product-induced mitogenesis is dependent on Janus kinase 2-induced heat shock protein 70 in normal rat kidney interstitial fibroblast cells. *Transl Res* **149**, 274–281 (2007).

153.   Gellai, R. *et al.* Role of O-linked N-acetylglucosamine modification in diabetic nephropathy. *Am J Physiol Renal Physiol* **311**, F1172–F1181 (2016).

154.   Qi, W. *et al.* High glucose-induced thioredoxin-interacting protein in renal proximal tubule cells is independent of transforming growth factor-beta1. *Am J Pathol* **171**, 744–754 (2007).

155.   Buraczynska, M., Swatowski, A., Buraczynska, K., Dragan, M. & Ksiazek, A. Heat-shock protein gene polymorphisms and the risk of nephropathy in patients with Type 2 diabetes. *Clin Sci (Lond)* **116**, 81–86 (2009).

156.   Zubair, M. & Ahmad, J. Heat Shock Protein 70 Gene Single Nucleotide Polymorphism and Diabetic Foot Ulcer. Is There Any Relationship? *J Clin Med* **7**, E187 (2018).

157.   Chuang, L. M., Jou, T. S., Wu, H. P., Tai, T. Y. & Lin, B. J. A rapid method to study heat shock protein 70-2 gene polymorphism in insulin-dependent diabetes mellitus. *Pancreas* **13**, 268–272 (1996).

158.   Moniruzzaman, M. *et al.* Association of polymorphism in heat shock protein 70 genes with type 2 diabetes in Bangladeshi population. *Mol Genet Genomic Med* **8**, e1073 (2020).

159.   Wiemerslage, L. & Lee, D. Quantification of mitochondrial morphology in neurites of dopaminergic neurons using multiple parameters. *J Neurosci Methods* **262**, 56–65 (2016).

160.   Pel, H. J. & Grivell, L. A. Protein synthesis in mitochondria. *Mol Biol Rep* **19**, 183–194 (1994).

161.   Barchiesi, A. & Vascotto, C. Transcription, Processing, and Decay of Mitochondrial RNA in Health and Disease. *Int J Mol Sci* **20**, E2221 (2019).

162.   Lowenstein, J. M. *Citric acid cycle*. (Academic Press, 1969).

163.   Voet, D. & Voet, J. G. *Biochemistry*. (Wiley, 2004).

164.   Longo, V. D., Gralla, E. B. & Valentine, J. S. Superoxide dismutase activity is essential for stationary phase survival in Saccharomyces cerevisiae. Mitochondrial production of toxic oxygen species in vivo. *J Biol Chem* **271**, 12275–12280 (1996).

165.   Nishikawa, T. *et al.* Normalizing mitochondrial superoxide production blocks three pathways of hyperglycaemic damage. *Nature* **404**, 787–790 (2000).

166.   DeHart, D. N. *et al.* Opening of voltage dependent anion channels promotes reactive oxygen species generation, mitochondrial dysfunction and cell death in cancer cells. *Biochem Pharmacol* **148**, 155–162 (2018).

167.   Twig, G. *et al.* Fission and selective fusion govern mitochondrial segregation and elimination by autophagy. *EMBO J* **27**, 433–446 (2008).

168.   Toyama, E. Q. *et al.* Metabolism. AMP-activated protein kinase mediates mitochondrial fission in response to energy stress. *Science* **351**, 275–281 (2016).

169.   Yoneda, M., Miyatake, T. & Attardi, G. Complementation of mutant and wild-type human mitochondrial DNAs coexisting since the mutation event and lack of complementation of DNAs introduced separately into a cell within distinct organelles. *Mol Cell Biol* **14**, 2699–2712 (1994).

170.   Ishihara, N., Eura, Y. & Mihara, K. Mitofusin 1 and 2 play distinct roles in mitochondrial fusion reactions via GTPase activity. *J Cell Sci* **117**, 6535–6546 (2004).

171.   Song, Z., Chen, H., Fiket, M., Alexander, C. & Chan, D. C. OPA1 processing controls mitochondrial fusion and is regulated by mRNA splicing, membrane potential, and Yme1L. *J Cell Biol* **178**, 749–755 (2007).

172.   Koirala, S. *et al.* Interchangeable adaptors regulate mitochondrial dynamin assembly for membrane scission. *Proc. Natl. Acad. Sci. U.S.A.* **110**, (2013).

173.   Ingerman, E. *et al.* Dnm1 forms spirals that are structurally tailored to fit mitochondria. *J Cell Biol* **170**, 1021–1027 (2005).

174.   Mears, J. A. *et al.* Conformational changes in Dnm1 support a contractile mechanism for mitochondrial fission. *Nat Struct Mol Biol* **18**, 20–26 (2011).

175.   Puigserver, P. *et al.* A cold-inducible coactivator of nuclear receptors linked to adaptive thermogenesis. *Cell* **92**, 829–839 (1998).

176.   Wu, Z. *et al.* Mechanisms controlling mitochondrial biogenesis and respiration through the thermogenic coactivator PGC-1. *Cell* **98**, 115–124 (1999).

177.   Gaspari, M., Falkenberg, M., Larsson, N.-G. & Gustafsson, C. M. The mitochondrial RNA polymerase contributes critically to promoter specificity in mammalian cells. *EMBO J* **23**, 4606–4614 (2004).

178.   Ryan, M. T., Müller, H. & Pfanner, N. Functional staging of ADP/ATP carrier translocation across the outer mitochondrial membrane. *J Biol Chem* **274**, 20619–20627 (1999).

179.   Bauer, M. F. *et al.* Genetic and structural characterization of the human mitochondrial inner membrane translocase 1 1Edited by J. Karn. *Journal of Molecular*

Biology **289**, 69–82 (1999).

180.   Jin, S. M. *et al.* Mitochondrial membrane potential regulates PINK1 import and proteolytic destabilization by PARL. *Journal of Cell Biology* **191**, 933–942 (2010).

181.   Greene, A. W. *et al.* Mitochondrial processing peptidase regulates PINK1 processing, import and Parkin recruitment. *EMBO Rep* **13**, 378–385 (2012).

182.   Yamano, K. & Youle, R. J. PINK1 is degraded through the N-end rule pathway. *Autophagy* **9**, 1758–1769 (2013).

183.   Okatsu, K. *et al.* PINK1 autophosphorylation upon membrane potential dissipation is essential for Parkin recruitment to damaged mitochondria. *Nat Commun* **3**, 1016 (2012).

184.   Okatsu, K. *et al.* A Dimeric PINK1-containing Complex on Depolarized Mitochondria Stimulates Parkin Recruitment. *Journal of Biological Chemistry* **288**, 36372–36384 (2013).

185.   Kane, L. A. *et al.* PINK1 phosphorylates ubiquitin to activate Parkin E3 ubiquitin ligase activity. *Journal of Cell Biology* **205**, 143–153 (2014).

186.   Wei, Y., Chiang, W.-C., Sumpter, R., Mishra, P. & Levine, B. Prohibitin 2 Is an Inner Mitochondrial Membrane Mitophagy Receptor. *Cell* **168**, 224-238.e10 (2017).

187.   Chu, C. T. *et al.* Cardiolipin externalization to the outer mitochondrial membrane acts as an elimination signal for mitophagy in neuronal cells. *Nat Cell Biol* **15**, 1197–1205 (2013).

188.   Hanna, R. A. *et al.* Microtubule-associated Protein 1 Light Chain 3 (LC3) Interacts with Bnip3 Protein to Selectively Remove Endoplasmic Reticulum and Mitochondria via Autophagy. *Journal of Biological Chemistry* **287**, 19094–19104 (2012).

189.   Rikka, S. *et al.* Bnip3 impairs mitochondrial bioenergetics and stimulates mitochondrial turnover. *Cell Death Differ* **18**, 721–731 (2011).

190.   Paltauf-Doburzynska, J., Malli, R. & Graier, W. F. Hyperglycemic conditions affect shape and Ca2+ homeostasis of mitochondria in endothelial cells. *J Cardiovasc Pharmacol* **44**, 423–436 (2004).

191.   Yu, T., Robotham, J. L. & Yoon, Y. Increased production of reactive oxygen species in hyperglycemic conditions requires dynamic change of mitochondrial morphology. *Proc Natl Acad Sci U S A* **103**, 2653–2658 (2006).

192.   Kytövuori, L. *et al.* A novel mutation m.8561C>G in MT-ATP6/8 causing a mitochondrial syndrome with ataxia, peripheral neuropathy, diabetes mellitus, and

hypergonadotropic hypogonadism. *J Neurol* **263**, 2188–2195 (2016).

193. Lowell, B. B. & Shulman, G. I. Mitochondrial dysfunction and type 2 diabetes. *Science* **307**, 384–387 (2005).

194. Heinonen, S. *et al.* Impaired Mitochondrial Biogenesis in Adipose Tissue in Acquired Obesity. *Diabetes* **64**, 3135–3145 (2015).

195. Patti, M. E. *et al.* Coordinated reduction of genes of oxidative metabolism in humans with insulin resistance and diabetes: Potential role of PGC1 and NRF1. *Proc Natl Acad Sci U S A* **100**, 8466–8471 (2003).

196. Mootha, V. K. *et al.* PGC-1alpha-responsive genes involved in oxidative phosphorylation are coordinately downregulated in human diabetes. *Nat Genet* **34**, 267–273 (2003).

197. van der Kloet, F. M. *et al.* Discovery of early-stage biomarkers for diabetic kidney disease using ms-based metabolomics (FinnDiane study). *Metabolomics* **8**, 109–119 (2012).

198. Pena, M. J. *et al.* Urine and plasma metabolites predict the development of diabetic nephropathy in individuals with Type 2 diabetes mellitus. *Diabet Med* **31**, 1138–1147 (2014).

199. Sharma, K. *et al.* Metabolomics reveals signature of mitochondrial dysfunction in diabetic kidney disease. *J Am Soc Nephrol* **24**, 1901–1912 (2013).

200. Qi, W. *et al.* Pyruvate kinase M2 activation may protect against the progression of diabetic glomerular pathology and mitochondrial dysfunction. *Nat Med* **23**, 753–762 (2017).

201. Crouch, S. P., Kozlowski, R., Slater, K. J. & Fletcher, J. The use of ATP bioluminescence as a measure of cell proliferation and cytotoxicity. *J Immunol Methods* **160**, 81–88 (1993).

202. Huang, H. C., Nguyen, T. & Pickett, C. B. Regulation of the antioxidant response element by protein kinase C-mediated phosphorylation of NF-E2-related factor 2. *Proc Natl Acad Sci U S A* **97**, 12475–12480 (2000).

203. Ross, D. *et al.* NAD(P)H:quinone oxidoreductase 1 (NQO1): chemoprotection, bioactivation, gene regulation and genetic polymorphisms. *Chemico-Biological Interactions* **129**, 77–97 (2000).

204. Alam, J. *et al.* Nrf2, a Cap'n'Collar transcription factor, regulates induction of the heme oxygenase-1 gene. *J Biol Chem* **274**, 26071–26078 (1999).

205. Sena, C. M. *et al.* Methylglyoxal promotes oxidative stress and endothelial

dysfunction. *Pharmacol Res* **65**, 497–506 (2012).

206.   Kagawa, Y. & Racker, E. Partial resolution of the enzymes catalyzing oxidative phosphorylation. 8. Properties of a factor conferring oligomycin sensitivity on mitochondrial adenosine triphosphatase. *J Biol Chem* **241**, 2461–2466 (1966).

207.   Park, K.-S. *et al.* FCCP depolarizes plasma membrane potential by activating proton and Na+ currents in bovine aortic endothelial cells. *Pflugers Arch* **443**, 344–352 (2002).

208.   Wolvetang, E. J., Johnson, K. L., Krauer, K., Ralph, S. J. & Linnane, A. W. Mitochondrial respiratory chain inhibitors induce apoptosis. *FEBS Lett* **339**, 40–44 (1994).

209.   Chacko, B. K. *et al.* The Bioenergetic Health Index: a new concept in mitochondrial translational research. *Clin Sci (Lond)* **127**, 367–373 (2014).

210.   Irshad, Z. *et al.* Activation of the unfolded protein response in high glucose treated endothelial cells is mediated by methylglyoxal. *Sci Rep* **9**, 7889 (2019).

211.   Fleming, T. *et al. Methylglyoxal Induces Endothelial Dysfunction via Stunning-like Phenotype.* http://biorxiv.org/lookup/doi/10.1101/2021.11.18.469085 (2021) doi:10.1101/2021.11.18.469085.

212.   Jarisarapurin, W., Kunchana, K., Chularojmontri, L. & Wattanapitayakul, S. K. Unripe Carica papaya Protects Methylglyoxal-Invoked Endothelial Cell Inflammation and Apoptosis via the Suppression of Oxidative Stress and Akt/MAPK/NF-κB Signals. *Antioxidants (Basel)* **10**, 1158 (2021).

213.   Wang, T., Streeter, M. D. & Spiegel, D. A. Generation and characterization of antibodies against arginine-derived advanced glycation endproducts. *Bioorg Med Chem Lett* **25**, 4881–4886 (2015).

214.   Raupbach, J., Ott, C., Koenig, J. & Grune, T. Proteasomal degradation of glycated proteins depends on substrate unfolding: Preferred degradation of moderately modified myoglobin. *Free Radic Biol Med* **152**, 516–524 (2020).

215.   Uchiki, T. *et al.* Glycation-altered proteolysis as a pathobiologic mechanism that links dietary glycemic index, aging, and age-related disease (in nondiabetics): Glycation altered proteolysis and aging. *Aging Cell* **11**, 1–13 (2012).

216.   Zemva, J. *et al.* Hormesis enables cells to handle accumulating toxic metabolites during increased energy flux. *Redox Biology* **13**, 674–686 (2017).

217.   Kim, D., Kim, K.-A., Kim, J.-H., Kim, E.-H. & Bae, O.-N. Methylglyoxal-Induced Dysfunction in Brain Endothelial Cells via the Suppression of Akt/HIF-1α Pathway and

Activation of Mitophagy Associated with Increased Reactive Oxygen Species. *Antioxidants (Basel)* **9**, E820 (2020).

218. Braun, J. D. *et al.* Methylglyoxal down-regulates the expression of cell cycle associated genes and activates the p53 pathway in human umbilical vein endothelial cells. *Sci Rep* **9**, 1152 (2019).

219. Paramita, D. & Wisnubroto, J. D. P. Effect of methylglyoxal on reactive oxygen species, KI-67, and caspase-3 expression in MCF-7 cells. *Exp Mol Pathol* **105**, 76–80 (2018).

220. Bollong, M. J. *et al.* A metabolite-derived protein modification integrates glycolysis with KEAP1-NRF2 signalling. *Nature* **562**, 600–604 (2018).

221. Webster, L., Abordo, E. A., Thornalley, P. J. & Limb, G. A. Induction of TNF alpha and IL-1 beta mRNA in monocytes by methylglyoxal- and advanced glycated endproduct-modified human serum albumin. *Biochem Soc Trans* **25**, 250S (1997).

222. Laga, M. *et al.* Methylglyoxal suppresses TNF-alpha-induced NF-kappaB activation by inhibiting NF-kappaB DNA-binding. *Biochem Pharmacol* **74**, 579–589 (2007).

223. Chen, Y.-F. *et al.* The Antioxidant, Anti-Inflammatory, and Neuroprotective Properties of the Synthetic Chalcone Derivative AN07. *Molecules* **25**, E2907 (2020).

224. Donnellan, L. *et al.* Proteomic Analysis of Methylglyoxal Modifications Reveals Susceptibility of Glycolytic Enzymes to Dicarbonyl Stress. *Int J Mol Sci* **23**, 3689 (2022).

225. Padival, A. K., Crabb, J. W. & Nagaraj, R. H. Methylglyoxal modifies heat shock protein 27 in glomerular mesangial cells. *FEBS Lett* **551**, 113–118 (2003).

226. Rosca, M. G. *et al.* Glycation of mitochondrial proteins from diabetic rat kidney is associated with excess superoxide formation. *Am J Physiol Renal Physiol* **289**, F420-430 (2005).

227. Rossini, A. A., Like, A. A., Chick, W. L., Appel, M. C. & Cahill, G. F. Studies of streptozotocin-induced insulitis and diabetes. *Proc Natl Acad Sci U S A* **74**, 2485–2489 (1977).

228. Jheng, H.-F. *et al.* Albumin stimulates renal tubular inflammation through an HSP70-TLR4 axis in mice with early diabetic nephropathy. *Dis Model Mech* **8**, 1311–1321 (2015).

229. Rossi, G. P. *et al.* A prospective study of the prevalence of primary aldosteronism in 1,125 hypertensive patients. *J Am Coll Cardiol* **48**, 2293–2300

118

(2006).

230.   Allerheiligen, D. A., Schoeber, J., Houston, R. E., Mohl, V. K. & Wildman, K. M. Hyperparathyroidism. *Am Fam Physician* **57**, 1795–1802, 1807–1808 (1998).

231.   Gohil, A. & Imel, E. A. FGF23 and Associated Disorders of Phosphate Wasting. *Pediatr Endocrinol Rev* **17**, 17–34 (2019).

232.   Aluksanasuwan, S., Sueksakit, K., Fong-Ngern, K. & Thongboonkerd, V. Role of HSP60 (HSPD1) in diabetes-induced renal tubular dysfunction: regulation of intracellular protein aggregation, ATP production, and oxidative stress. *FASEB J* **31**, 2157–2167 (2017).

233.   Sanchez-Niño, M. D. *et al.* HSP27/HSPB1 as an adaptive podocyte antiapoptotic protein activated by high glucose and angiotensin II. *Lab Invest* **92**, 32–45 (2012).

234.   Tikoo, K., Meena, R. L., Kabra, D. G. & Gaikwad, A. B. Change in post-translational modifications of histone H3, heat-shock protein-27 and MAP kinase p38 expression by curcumin in streptozotocin-induced type I diabetic nephropathy. *Br J Pharmacol* **153**, 1225–1231 (2008).

235.   Barutta, F. *et al.* Heat shock protein expression in diabetic nephropathy. *American Journal of Physiology-Renal Physiology* **295**, F1817–F1824 (2008).

236.   Moon, S.-J. *et al.* The potential roles of NAD(P)H:quinone oxidoreductase 1 in the development of diabetic nephropathy and actin polymerization. *Sci Rep* **10**, 17735 (2020).

237.   Perez-Gomez, M. V. *et al.* Urinary Growth Differentiation Factor-15 (GDF15) levels as a biomarker of adverse outcomes and biopsy findings in chronic kidney disease. *J Nephrol* **34**, 1819–1832 (2021).

238.   Liu, J.-J. *et al.* Vascular cell adhesion molecule-1, but not intercellular adhesion molecule-1, is associated with diabetic kidney disease in Asians with type 2 diabetes. *J Diabetes Complications* **29**, 707–712 (2015).

239.   Jia, Y., Xu, H., Yu, Q., Tan, L. & Xiong, Z. Identification and verification of vascular cell adhesion protein 1 as an immune-related hub gene associated with the tubulointerstitial injury in diabetic kidney disease. *Bioengineered* **12**, 6655–6673 (2021).

240.   Ayanga, B. A. *et al.* Dynamin-Related Protein 1 Deficiency Improves Mitochondrial Fitness and Protects against Progression of Diabetic Nephropathy. *J Am Soc Nephrol* **27**, 2733–2747 (2016).

241. Yang, S.-K. *et al.* Mitochondria-Targeted Peptide SS31 Attenuates Renal Tubulointerstitial Injury via Inhibiting Mitochondrial Fission in Diabetic Mice. *Oxid Med Cell Longev* **2019**, 2346580 (2019).

242. Audzeyenka, I. *et al.* Hyperglycemia alters mitochondrial respiration efficiency and mitophagy in human podocytes. *Exp Cell Res* **407**, 112758 (2021).

243. Morgenstern, J. *et al.* Loss of Glyoxalase 1 Induces Compensatory Mechanism to Achieve Dicarbonyl Detoxification in Mammalian Schwann Cells. *J Biol Chem* **292**, 3224–3238 (2017).

244. Livak, K. J. & Schmittgen, T. D. Analysis of relative gene expression data using real-time quantitative PCR and the 2(-Delta Delta C(T)) Method. *Methods* **25**, 402–408 (2001).

245. Bradford, M. M. A rapid and sensitive method for the quantitation of microgram quantities of protein utilizing the principle of protein-dye binding. *Anal Biochem* **72**, 248–254 (1976).

246. Schindelin, J. *et al.* Fiji: an open-source platform for biological-image analysis. *Nat Methods* **9**, 676–682 (2012).

247. Pike Winer, L. S. & Wu, M. Rapid analysis of glycolytic and oxidative substrate flux of cancer cells in a microplate. *PLoS One* **9**, e109916 (2014).

248. Rabbani, N., Shaheen, F., Anwar, A., Masania, J. & Thornalley, P. J. Assay of methylglyoxal-derived protein and nucleotide AGEs. *Biochem Soc Trans* **42**, 511–517 (2014).

249. Ahmed, N. & Thornalley, P. J. Chromatographic assay of glycation adducts in human serum albumin glycated in vitro by derivatization with 6-aminoquinolyl-N-hydroxysuccinimidyl-carbamate and intrinsic fluorescence. *Biochem J* **364**, 15–24 (2002).

7 ACKNOWLEDGEMENTS